A Broadband Mid-infrared Metasurface for Polarisation Manipulation and Utilisation

Huanling Zou

Natural Sciences

University of Exeter

A thesis submitted for the degree of

Doctor of Philosophy

August 2023

A Broadband Mid-infrared Metasurface for Polarisation Manipulation and Utilisation

Submitted by Huanling Zou to the University of Exeter as a thesis for the degree of

Doctor of Philosophy in Natural Sciences

In August 2023

I certify that all material in this thesis which is not my own work has been identified and that no material has previously been submitted and approved for the award of a degree by this or any other university.

(Signature)…….

Huanling Zou

August 2023

Acknowledgements

Looking back to my four-year doctoral study, the pandemic seems to evaporate the time, but fortunately a trail of memory fragments still fill me with a profound sense of gratitude.

First and foremost, I would like to thank my supervisor, Professor *Geoff Nash.* Pursuing a PhD research can indeed be a solitary experience as it often means to develop a specialised area that few people around might fully understand. It is a unique adventure like hiking through an unknown forest. It is embarked by curiosity, powered by satisfaction of new findings but also challenged by obstacles leading to strong self-doubt and sense of hopeless. However, I have been fortunate enough to have such remarkable supervisor who is so knowledgeable, purely enthusiastic to education and genuinely concerns about students. I appreciate the continuous inspiration, encouragement, solid trust as well as some freedom he gave me and let me explore and learn different techniques to broaden my research skills. I sincerely feel grateful for his valuable feedbacks to navigate the adventure as well as confidence he gave me to make this adventure possible.

I still consider it a privilege to work in Exeter, so I would like to acknowledge the financial support from Chinese Scholarship Council and University of Exeter PhD scholarship for offering me possibility to pursuing my research in Exeter and to have opportunity to experience a new lifestyle.

I would like to acknowledge the contribution from those inspiring scientists that I worked with during my PhD. First, I very much appreciate having nano-fabrication training delivered by Mr Mark Heath who dedicated his valuable time to patiently guide me on fabricating my samples step by step. I would also like to express my gratitude to Dr Prarthana Gowda for the guidance and help to handle reflection system and FTIR. I am also grateful for Miss Hannah Barnard who help me to familiarised with FDTD tool at beginning of my PhD study and share an important algorithms on computing the optical chirality density which is a core idea that chapter 6 built upon.

My PhD study started right before 2020, as an international student, my life was heavily impacted by the pandemic. However, I am lucky that I had great company from my friends so here I would like extend my sincere thank you to them. Greatest appreciation to Dr Vicky kyrimi who showed me around in Exeter when I first came to the UK. Our friendship has provides me great company during pandemic. I feel very luck to build solid friendship with Ms Yu Qian with our countless memories where I always gain some comfort from and I would like to cherish it as long as I can. I also would like to thank Dr Kavya Sreeja Sadanandan, Dr Iago Rodriguez, Shi Guo, Dr Jessica Farrow, for those shared moments that have become precious memories. Last, I want to express the great thank you to my boyfriend Mr Toby Roberts who's presence bring me so much joy, comfort, peace and positivity.

Finally, from bottom of my heart, I want to express my deeply thank you and miss to my family in China. I want to sincerely thank my parents: Yiqing Zou and

Xiaoying Bao. I appreciate their unconditional support to offer me opportunity to pursue research in university they were never so lucky to have. I appreciate the love, care, and support from my grandparents: Yuquan Bao and Xuhua Tu who bring me up and shaped who I am.

Abstract

A pair of enantiomers are distinct from each other due to chiral structural arrangement which leads to selective interaction with chiral light. Vibrational circular dichroism spectroscopy in mid-infrared region provide a powerful label-free method to distinguish chiral enantiomers. Besides, mid-infrared sensing also significantly benefit from resolving compositional information of molecules due to molecular vibrational fingerprints which holds promising application in biological and medical sensing. However, the low signal-to-noise ratio associated with weak light-matter interaction is a continuing obstacle hindering the practical application. Recent demonstrations of chiral metamaterials have shown that due to the chirality of structure, local superchiral field can be produced in the vicinity of structure to interact with molecules and enhance vibrational circular dichroism response. However, a limitation factor in development of chiral structure is the narrow effective working bandwidth and the requirement of circular polarization excitation. This thesis introduces an achiral nanorod-based metausrface that enable to overcome these limitations.

First, the nanorod-based metasurface is present to achieve high efficient linear-to-circular polarization conversion in a broadband mid-infrared wavelength range in reflection mode. The model was firstly studied and optimised through simulation tool based on Finite Difference Time Domain method. The device was fabricated in a top-down approach based on electron beam lithography and characterised using Fourier transform infrared spectroscopy. We identified two

distinct resonances originated from gap-plasmon mode at 3.4μm and Fabry-Perot mode at 7.9μm. The demonstration of polarization state based on the measured Stokes parameters within off-resonance range from 4-7μm show that the reflected beam has converted into circular polarization state.

For practical application of vibrational circular dichroism spectroscopy, we numerically demonstrate the induced chirality in near-field under excitation of linear polarization with various polarization angles. These analysis suggest that superchiral field can be produced by nanorod-based metasurface and distributed spatially under linear polarization excitation. When polarization is parallel or orthogonal to rod, namely the symmetry exist in the combination of rod and incident polarization, the absolute chirality is zero due to the fact that same amount of optical chirality density with opposite handedness offset by each other. However it is showed that one handedness of the optical chirality density is dominant when the symmetry is broken, hence, holds potential for circular dichroism spectroscopy sensing. In an experimental feasibility study, we measured the polarization states of light in far-field and demonstrate that the absolute chirality in the far-field show similar behaviour as that in near-field.

Finally, we conduct a molecular sensing measurement based on the rod-shape metausrface for enantiomers (alanine) identification through circular dichroism spectroscopy. This thesis demonstrates with FDTD simulations that the metasurface can generate superchiral fields which enable to enhance interaction with molecules upon linear polarization excitation. By simply rotating sample with 90 degree, molecules can then interact with superchiral field with opposite

handedness. The circular dichroism is to record the intensity of reflected beam and characterise the differential intensity between the two. Despite the measured data do not show inverse pattern for L- and D-alanine, we confirmed that metausrface enable to enhance the light-matter interaction.

Contents

List of figures

1 Introduction

1.1 Motivation

Polarization, a crucial concept in electromagnetic waves, describe the oscillation direction of the electric field by tracing the tip of electric vector as the wave propagates. Polarization carries abundant useful information and has been widely used in communication industry [1], material properties analysis [2], display technologies [3] and biosensing [4], [5]. Depending on the tracing shapes, polarization are categorised into three types: linear, circular and elliptical. However, due to the fact that most of inherent light sources, such as sunlight or incandescent lamps, are unpolarised light, optical elements are employed to generate light with well-defined polarization states on demand. For example, a linear polarizer patterned with metal wire grid on crystal is designed to select linearly polarized light by filtering out the rest [6]. Another example is a waveplate made up of birefringence materials such as quartz [7], mica [8] or polymeric [9]. Waveplates enable the transformation of polarization of states from s- to p-polarized light, or linear-to-circular polarization depending on precisely designed thickness of the material to ensure phase retardation between two orthogonal polarized light beams is 90 degree[10], [11]. Quarter waveplates can achieve polarization transformation with low loss, but function within a very narrow band owing to the limited birefringence properties in natural materials. Also because of

this, wave plates are in bulky size in order to produce sufficient phase retardation as required.

Metasurfaces are a new class of artificial material that possess optical properties beyond materials in nature [12]–[14]. As there is growing requirement of miniaturization and dense integration in photonics device, there has been increasing research works on metasurface wave plate due to its unprecedented capabilities of manipulating polarization of light with just subwavelength thickness [15]–[18]. In addition, metasurface provides higher degrees of freedom to adjust its performance, such as operation wavelength, or phase delay through engineered building blocks. Benefiting from its subwavelength thickness and higher adjustment flexibilities, metasurface equivalents to waveplates are opening up a promising opportunity to revolutionize conventional bulky optical elements with ultrathin materials featuring broadband bandwidths, compactness, low-loss and integration capabilities.

Infrared light is part of electromagnetic spectrum encompassing wavelengths from around 1mm (300 GHz) to the nominal red edge of the visible spectrum, around 700 nm (430 THz). The mid-IR region of the spectrum is of particular interest in this thesis due to the important technique known as infrared spectroscopy, which is a powerful chemical analysis tool to identify and quantify almost any chemical species [19], [20]. Utilising the vibration of particular bonds within molecules, the interaction between light and compounds lead to an output spectrum with infrared absorption corresponding to the molecular frequencies. By obtaining the unique infrared absorption spectrum, there is an enormous

range of molecules that can be probed based on infrared spectroscopy such as: amino acid [21] and nucleotide [22].

However, the differentiation on chiral enantiomers is particularly challenging. Chiral refers to a geometric properties that objects cannot be superposed with their mirror image. When a pair of molecules have identical chemical configuration, but are mirror images of each other, they are known as a chiral enantiomer [23], [24]. Figure 1.1 (a) shows the structure of two thalidomide enantiomers. As you can see, enantiomers share the same molecular formula, however, the difference in their biological properties can be profound. A classic example is the well-known tragedy of chiral drug: thalidomide [25]. For many years, scientists have been blind to stereochemistry, thalidomide that mixed with enantiomers were prescribed to pregnant women to control nausea and vomiting, however, in later study, one of the enantiomer, (R)- enantiomer in thalidomide was found to cause fetal abnormalities such as phocomelia in pregnancy. The drug was withdrawn later from the world market. This example illustrates the extreme distinct consequence resulting from enantiomers and it provides the clearest indication that differentiation of enantiomers is crucial. Circular dichroism spectroscopy is a widely use analytical technique that measures the difference in absorption of left and right circularly polarized light as a function of wavelength. When enantiomers interact with circular polarized light, one state of circularly polarized light will be absorbed to a greater or less extent than the other and this lead to different absorption between right- and left-handed circularly polarized light. As a result, the circular dichroism spectra display positive and negative

resonances at particular frequencies. The circular dichroism spectra of enantiomers have the same intensity, but opposite sign as shown in Figure 1.1 (b), which is a clear way of identifying enantiomers. However, the difference in absorbance between left- and right- light is usually very small in the range of $(10^{-3} - 10^{-5})$ [26] therefore, the capability of enhancing weak circular dichroism effects for chiral molecules would be extremely beneficial. Recently, an emerging research works have been proposed to enhance the weak circular dichroism effects using plasmonic [27]–[30] or dielectric metamaterials [31]–[33] which show promising capability of confining the electromagnetic field to enhance the light-matter interaction at resonance frequency. The work presented in this thesis is an investigation of the potential of using a nanorod-based metasurface, operating in the important mid-infrared region, for enhanced vibrational circular dichroism spectroscopy in a broadband wavelength range.

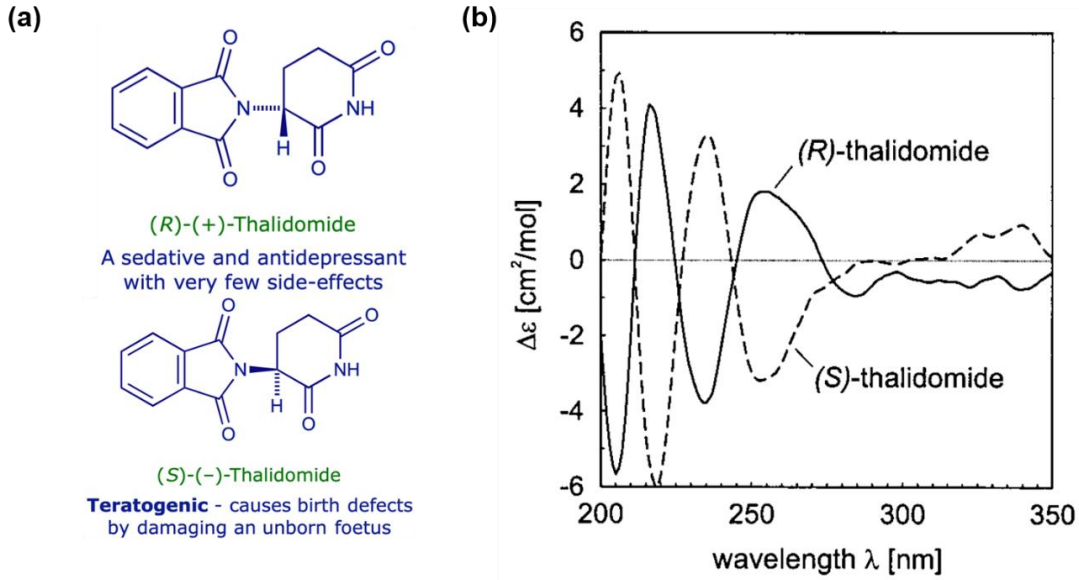

Figure 1.1 (a) Structures of the two enantiomers of thalidomide. (Illustration taken from [34]*) (b) CD spectra of (R)- and (S)- thalidomide. (Illustration taken from* [35]*)*

1.2 Overview

The aim of this PhD project was to design, fabricate and characterise a nanorod-based metasurface to investigate its capability to manipulate the polarization of light, and its potential use in the differentiation of enantiomers based on vibrational circular dichroism spectroscopy in the mid-infrared wavelength region.

First of all, we used commercial software Lumerical FDTD (Finite-difference time-domain method) solutions to design and optimise structures which enable the conversion of the polarization of light from linear to circular in mid-infrared region. Next, the metasurface were fabricated in an ISO Class 5 cleanroom using electron beam lithography techniques. Then, the fabricated samples were tested with a self-built reflection system via Fourier Transform Infrared spectroscopy. Since the measurement data shows that the light reflected from device is circularly polarized light with linearly polarized illumination, and simulations showed that the metasurface produces strong chiral near-fields, this led us to investigate the metasuface's capability to differentiate chiral enantiomers based on vibrational circular dichroism spectroscopy.

The thesis is organised into eight chapters and the contents in the following chapters are summarized below:

Chapter 2 provides background knowledge of polarization and vibrational circular dichroism spectroscopy along with a review of the relevant core literature. The first section gives a brief introduction to the polarization of light and the Stokes parameters that can characterise polarization of light in practice. The second

section is a literature review summarizing three common strategies to achieve linear-to-circular polarization conversion based on metasurfaces, leading to a discussion of the advantages of the approach taken in the work described in this thesis. The third section is an introduction to infrared spectroscopy and vibrational circular dichroism spectroscopy techniques followed by a summary of the latest developments on mid-infrared spectroscopy utilizing chiral metasurfaces.

Chapter 3 present details on the simulation tool, Lumerical FDTD solutions. This starts with an introduction to the background theory of FDTD method: Yee's theory. It's followed by the description on the simulation setup, analysis and optimization of simulation results.

Chapter 4 introduces the techniques used in the fabrication and characterisation of the nanorod-based metasurface. A brief description of the top-down nanostructure fabrication method used, based on electron beam lithography, is first given, followed by an introduction of the metasurface characterisation starting from the techniques including optical microscope and scanning electron microscope that were used to inspect fabricated samples. The next section provides details on the set-ups of the Fourier Transform Infrared Spectroscopy to characterise samples. This start with the introduction on background knowledge of Fourier Transform Infrared Spectroscopy, and is followed the description of the measurement setups, including transmission system, that were used to test the optical elements, and reflection system which was used to characterise the performance of the metasurface.

Chapter 5 presents the study of a nanorod-based metasurface, upon which my PhD project is built. With the aim of achieving broadband linear-to-circular polarization conversion, this chapter first summarise the anisotropic property of the metasurface with decomposed orthogonal polarizations through FDTD method. By optimising geometries, we demonstrate that the structure can achieve linear-to-circular polarization conversion within broadband off-resonance wavelength range from 4-7μm under linear polarization excitation. We also show that the effective operation wavelength range for linear-to circular polarization conversion will be reduced due to introducing an extra resonance at 4.8μm in some special cases of oblique incidence. These simulation analysis are verified experimentally by characterising absolute polarization states of reflected beam based on measured Stokes parameters. Part of this work has been published in Optical Materials Express [36].

Chapter 6 presents an analysis, via simulations, of the superchiral fields induced in the near-field of the nanorod-based metasurface, with the ultimate aim of exploiting these in enantiomeric sensing. We first introduce the optical chirality density as a useful concept to characterise the chirality of near-field, thus probing strength of light-matter interaction. We show that induced near-field chirality is spatially distributed and exhibits opposite handedness simultaneously. However, the absolute chirality, the sum of the opposite handedness across the unit cell, is the effective parameters to quantify the chirality of the near-field light. In order to utilise this superchiral field more effectively, we then investigated the dependence of the absolute chirality on incident polarization angles. We then discuss how the

absolute chirality in the near-field shows consistency with that measured in the far-field using Stokes parameters. The chapter finishes by considering the ideal excitation polarization to obtain maximum absolute chirality, and corresponded to light that excite linear-to-circular polarization conversion and its handedness can be switched by either rotating metasurface or incident polarization for 90 degree.

In Chapter 7 a label-free enantiomeric selection experiment scheme, built on the theoretical analysis in chapter 6, is described. Here a pair of enantiomers, L- and D-alanine are mixed in paraffin oil separately, and drop cast onto the metasurface. First experiments were undertaken to establish the optimum molecular concentration. Next, we confirm that the metasurface enhances light-matter interaction by orders of magnitude by comparing to the performance of substrate without resonators. Finally, we perform circular dichroism spectroscopy for D- and L-alanine. Although it wasn't possible to observe an enhancement of circular dichroism response, the results presented represent an important step towards using an achiral metasurface structure for the sensing of chiral molecules.

Finally, Chapter 8 summarises the conclusions of this work, and provides a perspective on future research avenues.

2 Fundamental concepts and background

2.1 Introduction

This chapter will serve as the background introduction on three important concepts discussed in this thesis, namely: polarization, metasurfaces and circular dichroism spectroscopy. The first section will mainly focus on the concept of polarization to understand the requirement for polarization conversion, and the method to characterise polarization in practice. It will describe the working principle of a traditional waveplate, which is an optical element that converts linear polarized to circularly polarized light, and their drawbacks. This will lead to the introduction of a metasurface that could potentially replace the conventional waveplate for manipulate polarization. There then follows a comparison between different approaches for achieving polarization transformation based on metasurfaces and a discussion on the advantages of our method. The last section is mainly focussed on the application of metasurfaces for the differentiation of chiral enantiomers. This will start with the introduction of infrared (IR) spectroscopy which is a powerful analytical technique as it allows the identification of chemical components by measuring the amount of light absorbed at specific frequencies, characteristic of specific chemical bonds. Then the focus will shift to vibrational circular dichroism spectroscopy witch is an analytical tool built upon infrared spectroscopy and which can used to differentiate between enantiomers. As this technique suffer from weak light-

matter interaction and hence a low signal-to-noise ratio, recent attention has been focused on using metasurfaces to enhance sensitivity. Finally, circular dichroism spectroscopy based on metasurfaces will be reviewed to illustrate the potential benefits of the metasurface explored in this thesis.

2.2 Polarization of light

2.2.1 Polarization definition

Light is an electromagnetic wave that is made up of mutually perpendicular, synchronized vibrating electric and magnetic field as shown in Figure 2.1. The vibration of the two fields are perpendicular to each other and perpendicular to the direction of wave propagation and energy, forming a transverse wave. It is worth noting that electric field in Figure 2.1 (a) only oscillates in one direction. In fact, natural sunlight and almost every artificial emission contain electric components vibrate in arbitrary direction in perpendicular plane with respect to the direction of propagation. Figure 2.1 (b) displays how natural light transmits through a linear polarizer (a grating structure). In this case, only the light with the electric field vibrating in a direction orthogonal to the grating can travel through polarizer, while the rest are completely blocked. This light is said to be polarized, whilst the light with randomly oriented electric components is described as non-polarized light [6]. In summary, polarization describes the vibration direction and magnitude of the electric field vector with respect to time and space in propagation.

Polarization is one of the most fundamental properties of light. It plays a crucial role in nature. Although human eyes are unable to sense the polarization state of light, it is very common ability amongst animals, such as insects or marine life, who use polarized light for assistance in predation [37], navigation [38] and intraspecific communication [39]. Polarization is also widely used in modern optical science and it extends its applications into area such as biology, astronomy and chemistry, and benefits our daily life [40]. In the entertainment industry, techniques known as stereoscopic display in 3D movies is by projecting superimposed images into both eyes differently based on polarizing filters to produce a 3D effect [41]. In a totally different sense, liquid-crystal display (LCD) technology used in computer monitors and television screen relies on the rotation of the axis of linear polarization by the liquid crystal array [42]. In the communication industry, the radiation are intrinsically polarized to match the physical structure of the antenna for a better signal receiving [43]. In chemistry, as chiral molecules interact differently with circularly polarized light, known as circular dichroism, circularly polarized light is used to determine the chirality of organic molecules [44].

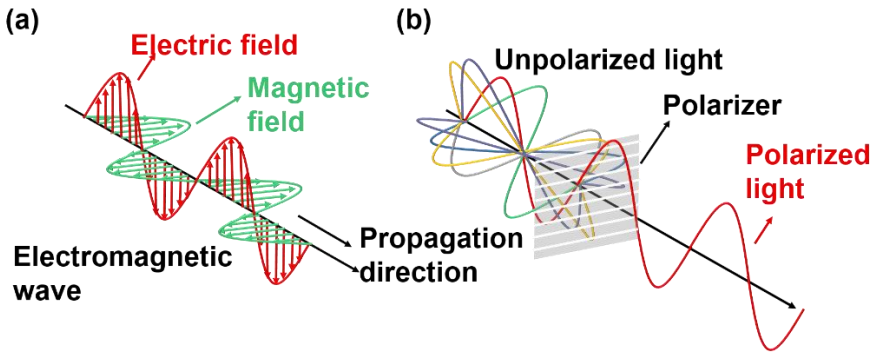

Figure 2.1 (a) Schematic of electromagnetic plane wave. (b) Unpolarised wave travel through grating polarizer.

2.2.2 Three types of polarizations of light

As the magnetic field always oscillates in the plane that is perpendicular to electric field, here we discuss the polarization of light only in terms of electric field components for simplicity. Light can be treated as transverse electromagnetic wave which consists of two orthogonal electric field components, also called optical disturbances, in the plane transverse to the direction of propagation. For reason of simplicity, the two orthogonal optical disturbances are assumed to travel along z axis. The wave function can be represented in the time-domain as [6]:

$$\boldsymbol{E}_x(z,t) = \hat{x}E_{0x}\cos(kz - \omega t) \tag{2.1}$$

$$\boldsymbol{E}_y(z,t) = \hat{y}E_{0y}\cos(kz - \omega t + \delta) \tag{2.2}$$

where $\omega = 2\pi f$ is the angular frequency, $k = \frac{2\pi}{\lambda}$ is the wave number magnitude, E_{0x} and E_{0y} are the maximum amplitudes and δ is the relative phase difference between the two components. The wave propagates toward the observation plane where the electric field to be measured is the sum of these two component:

$$\boldsymbol{E}(z,t) = \boldsymbol{E}_x(z,t) + \boldsymbol{E}_y(z,t) \tag{2.3}$$

There are three types of polarizations depending on the trace of electric vector tips during propagation: linearly polarized light, circularly polarized light and elliptically polarized light.

(1) Linearly polarized light

Linearly polarized light is given when the resultant electric vector only oscillates along one single direction, while its magnitude and sign varies in time. When the phase different δ is zero or an integer multiple of $\pm\pi$, the resultant wave is converted into:

$$\boldsymbol{E}(z,t) = \left(\hat{x}E_{0x} \pm \hat{y}E_{0y}\right)\cos(kz - \omega t) \tag{2.4}$$

In this particular case, the electric field vector of the resultant wave oscillates along a tilted line at an angle θ with respect to x axis. It has a fixed maximum magnitude equal to $\sqrt{{E_{0x}}^2 + {E_{0y}}^2}$. This tilted angle is determined by the amplitude of two components:

$$tan\theta = \frac{E_{0y}}{E_{0x}} \tag{2.5}$$

In particular, linearly polarized light only oscillates at $\theta = 45°$ if the two orthogonal components have equal magnitude: $E_{0x} = E_{0y}$ and the direction depends on their phase difference as shown in Figure 2.2. When $\delta = \pm n\pi$, where n is even number, the components are in phase, the combination wave vector oscillates at 45 degree with respect to x axis. When n is an odd number, the components are said to be out-of-phase, where the combination wave is still linearly polarized but the plane of oscillation is rotated by 90 degree.

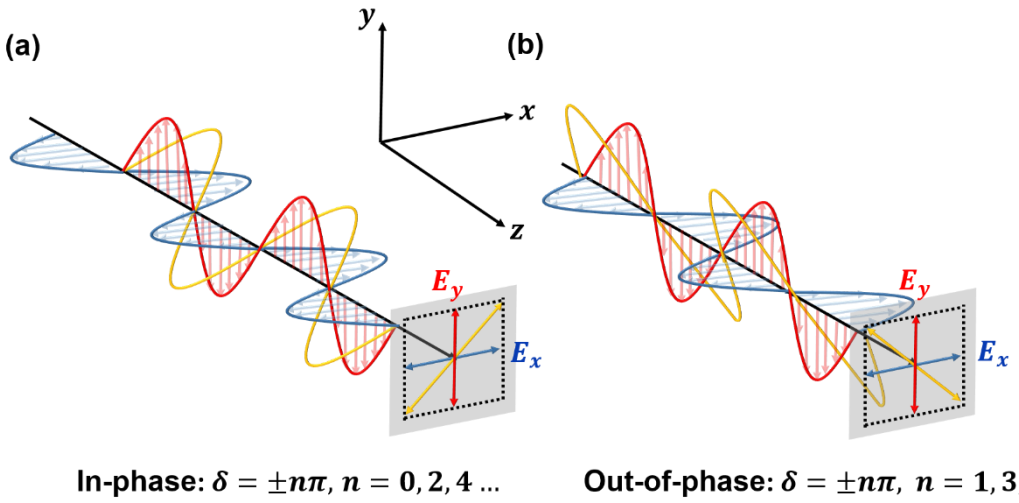

Figure 2.2 (a) Linearly polarized light when $\boldsymbol{E}_x$ and $\boldsymbol{E}_y$ are in phase. (b) Linearly polarized light when $\boldsymbol{E}_x$ and $\boldsymbol{E}_y$ are out of phase.

(2) circularly polarized light

Circularly polarized light is defined when the electric vector tip traces a circle in propagation. It can be accomplished when two orthogonal waves have equal amplitudes, i.e. $E_{0x} = E_{0y} = E_0$ and the phase difference have integer multiple of $\delta = \pm\frac{\pi}{2}$. In this special case, the orthogonal components become:

$$\boldsymbol{E}_x(z,t) = \hat{x}E_0\cos(kz - \omega t) \tag{2.6}$$

$$\boldsymbol{E}_y(z,t) = \hat{y}E_0\sin(kz - \omega t) \tag{2.7}$$

The consequent wave is given by:

$$\boldsymbol{E}(z,t) = E_0(\hat{x}\cos(kz - \omega t) \pm \hat{y}\sin(kz - \omega t)) \tag{2.8}$$

The angle of combination electric vector θ is:

$$\theta = arctan\left(\frac{E_y}{E_x}\right) = \pm(kz - \omega t) \tag{2.9}$$

It is clear from equation *(2.8)* that the magnitude of the combined wave is a constant E_0, however, equation (*2.9*) indicates that the electric field vector is steadily rotating at an angular frequency of ω as a function of time. As shown in Figure 2.3 , the trace of electric field tip form a circle and rotation direction can be clockwise or anticlockwise depending on the relative phase difference. When the phase difference is $-\frac{\pi}{2} \pm 2m\pi$ (m is an integer) where E_y is leading E_x, the resultant electric field rotation is clockwise. Such light is referred as right circularly polarized light. In comparison, if the phase difference is $\frac{\pi}{2} \pm 2m\pi$ (m is an integer), the combined wave is rotating anticlockwise and it is referred to as left circularly polarized light.

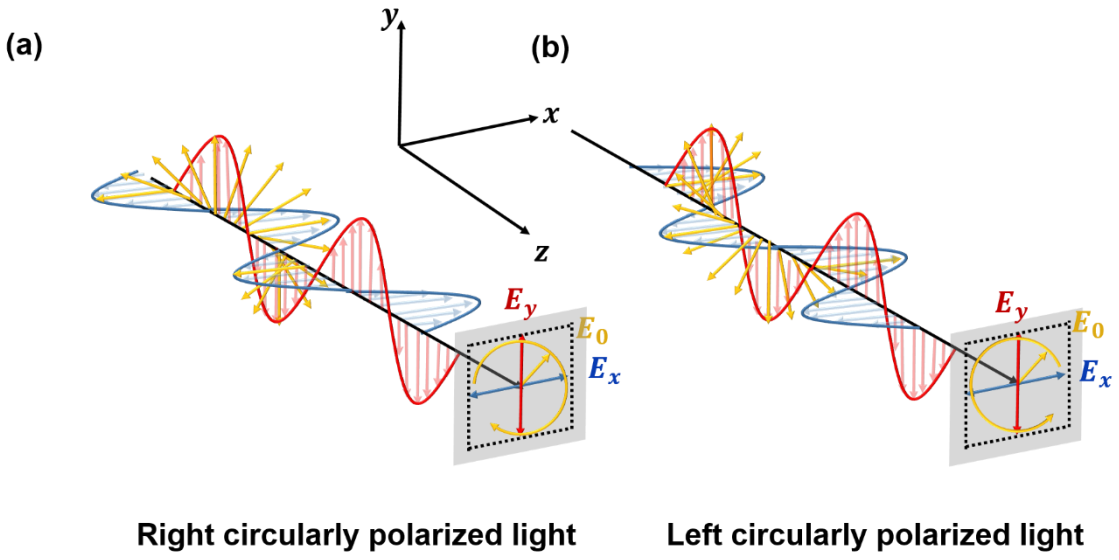

Figure 2.3 (a) Right-handed circularly polarized light. (b) Left-handed circularly polarized light.

By comparing equations (*2.4*) and (*2.8*), we can conclude that linearly polarized light at 45 degree can be converted into circularly polarized light by introducing $\frac{\pi}{2}$ phase delay between components and vice versa. This can be achieved by using a quarter wave plate, which are made out of a birefringent material such as quartz [7], mica [8] or organic polymeric plastic [9], and which have precisely adjusted thickness. Birefringent materials exhibit different refractive indexes along two certain orthogonal crystal axes. This birefringent property thus introduces a velocity difference between light polarized along optical axis. When linearly polarized light is passed through the wave plate, it will be divide into two components with identical magnitudes, but orthogonal polarization (components are marked in red and blue as shown in Figure 2.4. The speed of each polarization will be different due to the different refractive indexes, leading to a relative phase retardation between wavelets given as: $\Delta\varphi = \frac{2\pi L}{\lambda_0}\Delta n$ [6], where λ_0 is the wavelength in vacuum, L refers to the optical path length and Δn represent the difference of refractive indexes. As the optical path increases, the relative phase retardation accumulates, the state of polarization of the wave therefore gradually changes. The key to realise an ideal quarter wave plate is to precisely adjust the thickness of the crystal to $L = \frac{\lambda_0}{4\Delta n}$ to ensure a relative phase difference of 90 degrees. Similarly, it is possible to introduce a phase retardation of 180 degree by satisfying the expression: $L = \frac{\lambda_0}{2\Delta n}$. This defines a half wave plate, which enables the rotation of linearly polarized light vector with by a desired angle.

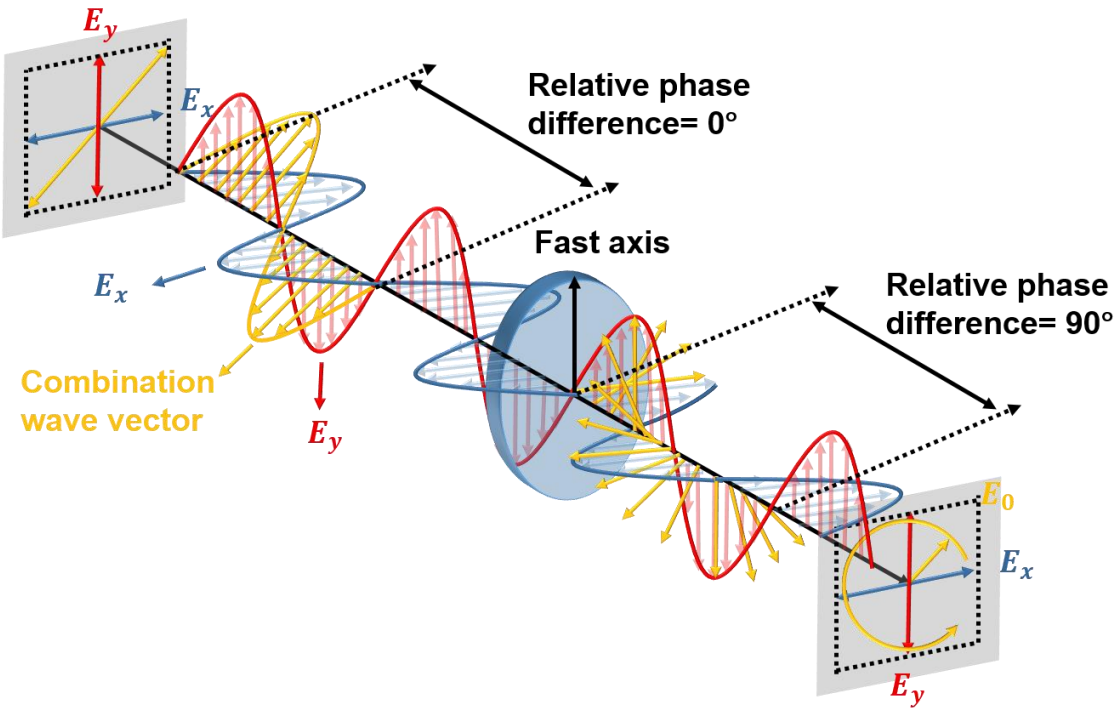

Figure 2.4 Working principle of quarter wave plate

A significant advantage of a wave plate is that it can manipulate polarization states with negligible loss. However, they also suffer from a limitation on the operational wavelength range. Due to the fact that the birefringent properties of materials is dispersive, wave plates are manufactured to function for a particular narrow range of wavelengths.

(3) elliptically polarized light

Elliptically polarized light is defined when the tip of electric field vector traces an ellipse in a fixed plane perpendicular to the propagation direction. In other words, the resultant electric field vector simultaneously rotates and changes its magnitude as a function of time. By eliminating the time-space propagator ($kz -$

ωt) in equation (*2.1*) and (*2.2*), the ellipse can be described by the expression known as polarization ellipse:

$$\frac{{E_x}^2}{{E_{x0}}^2} + \frac{{E_y}^2}{{E_{y0}}^2} - \frac{2E_xE_y}{E_{x0}E_{y0}} cos\delta = \sin^2\delta \tag{2.10}$$

This ellipse described in expression is tilted instead of standard ellipse in Cartesian coordinate system as shown in Figure 2.5. This tilted angle is defined as orientation angle ψ:

$$\tan 2\psi = \frac{2E_{0x}E_{0y}}{{E_{0x}}^2 - {E_{0y}}^2}\cos\delta \tag{2.11}$$

In addition to orientation angle, the polarization ellipse is also determined by the ratio of the length of the semi-minor axis to semi-major axis. This is known as ellipticity angle χ:

$$\sin 2\chi = \frac{2E_{0x}E_{0y}}{{E_{0x}}^2 + {E_{0y}}^2}\sin\delta \tag{2.12}$$

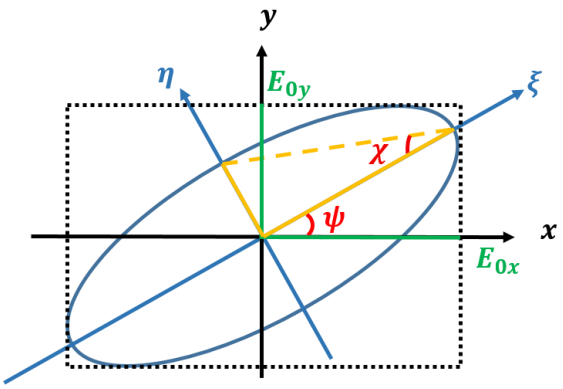

Figure 2.5 Polarization ellipse

In conclusion, equation (*2.10*) is a fundamental expression that governs the polarization of light, where the elliptical state is the most general case, whilst both linear and circular polarization states can be considered to be a special case of elliptically polarized light.

Next, we will introduce the Stokes parameters, which can be used to characterise polarized light.

2.2.3 Stokes Parameter

The polarization ellipse (*2.10*) is a general mathematical description of polarization. However, neither the orientation angle ψ nor ellipticity angle χ is directly measureable. In theory, the electric field makes a complete rotation as light propagates over a wavelength distance, however this is too short a distance to be able to measure the polarization in practice. In 1852, G. G. Stokes introduces four measureable parameters to quantify the polarization of electromagnetic waves, known as the Stokes parameters [45], [46]. In this method, the measurement are made in an average over a comparatively long time interval. In this context, we need to transform the time dependent field component from equation (*2.1*) and (*2.2*) into time averaged form [47], [48]:

$$\langle {E_x}^2 \rangle = \lim_{T \to 0} \frac{1}{T} \int_0^T E_x dt = \frac{1}{2} {E_{0x}}^2 \tag{2.13}$$

$$\langle {E_y}^2 \rangle = \lim_{T \to 0} \frac{1}{T} \int_0^T E_y dt = \frac{1}{2} {E_{0y}}^2 \tag{2.14}$$

where the time average is represented by the angular brackets <>, and T is the total averaging time. Similarly, the time average of $\langle E_x E_y \rangle$ is defined as [47]:

$$\langle E_x E_y \rangle = \lim_{T \to 0} \frac{1}{T} \int_0^T E_x E_y dt = \frac{1}{2} E_{0x} E_{0y} \cos \delta \tag{2.15}$$

Apply the time average definition to the polarization ellipse, it becomes:

$$\frac{\langle {E_x}^2 \rangle}{{E_{0x}}^2} + \frac{\langle {E_y}^2 \rangle}{{E_{0y}}^2} - 2 \frac{\langle E_x E_y \rangle}{E_{0x} E_{0y}} \cos \delta = \sin^2 \delta \tag{2.16}$$

After successive mathematic deduction, the polarization ellipse is transformed into:

$$\begin{aligned} &\left({E_{0x}}^2 + {E_{0y}}^2\right)^2 - \left({E_{0x}}^2 - {E_{0y}}^2\right)^2 - \left(2E_{0x}E_{0y} \cos \delta\right)^2 \\ &= \left(2E_{0x}E_{0y} \sin \delta\right)^2 \end{aligned} \tag{2.17}$$

The terms within the parentheses of (*2.17*) are now written as:

$$S_0 = {E_{0x}}^2 + {E_{0y}}^2 \tag{2.18}$$

$$S_1 = {E_{0x}}^2 - {E_{0y}}^2 \tag{2.19}$$

$$S_2 = 2E_{0x}E_{0y} \cos \delta \tag{2.20}$$

$$S_3 = 2E_{0x}E_{0y} \sin \delta \tag{2.21}$$

where S_0, S_1, S_2 and S_3 are defined as Stokes parameters [47]. The widely used form to arrange a set of Stokes parameters is called a column vector:

$$S = \begin{pmatrix} S_0 \\ S_1 \\ S_2 \\ S_3 \end{pmatrix} = \begin{pmatrix} {E_{0x}}^2 + {E_{0y}}^2 \\ {E_{0x}}^2 - {E_{0y}}^2 \\ 2E_{0x}E_{0y} \cos \delta \\ 2E_{0x}E_{0y} \sin \delta \end{pmatrix} \tag{2.22}$$

S_0 describes the total intensity of the optical beam. S_1 and S_2 together describe the shape and orientation of the polarization ellipse. S_3 describes the handedness of the ellipse. The four Stokes parameters can be linked by rewriting equation (*2.17*) into:

$$S_0{}^2 = S_1{}^2 + S_2{}^2 + S_3{}^2 \tag{2.23}$$

This expression indicates that the overall intensity of the polarized light can be obtained by calculating the sum of the square of S_1, S_2 and S_3. More importantly, it shows that the incident light is a complete polarized light where incident beam only have polarized waves. In the case of partially polarized light which is indicated as a mixture of completely polarized light and unpolarised light, and its Stokes parameters are represented by [47]:

$$S = \begin{pmatrix} S_0 \\ S_1 \\ S_2 \\ S_3 \end{pmatrix} = (1-p)\begin{pmatrix} 1 \\ 0 \\ 0 \\ 0 \end{pmatrix} + p\begin{pmatrix} S_0 \\ S_1 \\ S_2 \\ S_3 \end{pmatrix}, 0 \leq p \leq 1 \tag{2.24}$$

where p is known as degree of polarization (DOP), is defined by:

$$p = \frac{I_{polarized}}{I_{total}} = \frac{\sqrt{S_1{}^2 + S_2{}^2 + S_3{}^2}}{S_0}, 0 \leq p \leq 1 \tag{2.25}$$

where $I_{polarized}$ is the intensity of polarized light, I_{total} is total intensity. The result show that the relation between stokes parameters must be broadened to:

$$S_0{}^2 \geq S_1{}^2 + S_2{}^2 + S_3{}^2 \tag{2.26}$$

In summary, the four Stokes parameters together enable the representation of any form of complete polarization. In the most general case, elliptically polarized

light can be extracted with the orientation angle ψ and ellipticity angle χ. According to equations (*2.11*) and (*2.12*), these angle can be expressed by the Stokes parameters as:

$$\psi = \frac{1}{2}\tan^{-1}\frac{S_2}{S_1}, \qquad (0 \le \psi \le \pi) \tag{2.27}$$

$$\chi = \frac{1}{2}\sin^{-1}\frac{S_3}{S_0}, \qquad (-\frac{\pi}{4} \le \chi \le \frac{\pi}{4}) \tag{2.28}$$

As the four Stokes parameters are expressed in terms of intensities, as a result the polarisation of a given beam become measurable. Here are some examples for the degenerate polarization states escribed by Stokes parameters:

(1) Linearly polarized light

For the case of linearly polarized light that oscillate only along x axis, as there is no components along y axis $E_{0y} = 0$, we can calculate the Stokes parameters from equation (*2.18*) to (*2.21*):

$$S_{LP\_x} = {E_{x0}}^2 \begin{pmatrix} 1 \\ 1 \\ 0 \\ 0 \end{pmatrix} \tag{2.29}$$

Similarly, the linear polarized light along y axis can be described as:

$$S_{LP\_y} = {E_{y0}}^2 \begin{pmatrix} 1 \\ -1 \\ 0 \\ 0 \end{pmatrix} \tag{2.30}$$

The condition for obtaining linearly polarized light oscillate along $+45°$ degree with respect to x axis are: $E_{x0} = E_{y0} = E_0$ and the relative phase difference is $\delta = 0°$, then we have Stokes parameters as:

$$S_{LP+45} = {E_0}^2 \begin{pmatrix} 1 \\ 0 \\ 1 \\ 0 \end{pmatrix} \tag{2.31}$$

Similarly, for linearly polarized light oscillate along $-45°$ degree, the corresponding Stokes parameters can be:

$$S_{LP-45} = {E_0}^2 \begin{pmatrix} 1 \\ 0 \\ -1 \\ 0 \end{pmatrix} \tag{2.32}$$

(2) Circularly polarized light

The condition for obtaining right circularly polarized light are: $E_{x0} = E_{y0} = E_0$ and the relative phase difference is $\delta = 90°$. Substituting the condition into equation (*2.18*) to (*2.21*) then we have Stokes parameters as:

$$S_{RCP} = {E_0}^2 \begin{pmatrix} 1 \\ 0 \\ 0 \\ 1 \end{pmatrix} \tag{2.33}$$

Similarly, for left circularly polarized light oscillate, the corresponding Stokes parameters can be:

$$S_{LCP} = {E_0}^2 \begin{pmatrix} 1 \\ 0 \\ 0 \\ -1 \end{pmatrix} \tag{2.34}$$

In conclusion, any beam can be characterised by four stokes parameters. The measurement of Stokes parameters will be discussed with more details in chapter 5.

2.3 Polarization manipulation based on metasurfaces

As described previously in section 2.2.2, traditional optical elements rely on the intrinsic birefringent properties of the material to produce phase retardation between the components of light to accomplish polarization manipulation. The thickness of the optical element is critical in allowing control of the accumulated phase delay. As the birefringent properties of materials are wavelength-dependent, strong optical anisotropy can only be excited over a narrow band wavelength range. These drawbacks significantly restricts the functionality and potential integration of such optical components. In contrast, metasurfaces, which have been demonstrated to possess unprecedented capabilities to control light on a subwavelength scale, become a promising candidate to replace conventional optical components [49]. Matesurfaces, an innovative new class of artificial material, are typically periodic arrays of different shapes which are engineered at the sub-wavelength scale to interact resonantly with incident electromagnetic waves. Owing to the subwavelength size feature, metasurfaces derive their properties from the geometry of the internal elementary unit cells, rather than the properties of the materials that make up the metasurface. Specifically, the optical response of metasurfaces, including the number, energy and the direction of diffracted rays mainly depends on the corresponding individual structures of unit cells. This provide flexibility and versatility to produce desirable optical responses to manipulate electromagnetic radiation by optimising unit cell structures.

As the field of flat optics is rapidly growing, there has been increasing amounts of research investigating miniaturised optical wave plates based on metasurfaces that outperform conventional counterparts [50]. Early research was mainly focused on enhancing birefringence in optical antennas arrays to achieve polarization state modification [51]. The conceptual method for designing optical anisotropy is achieved by decomposing incident linearly polarized light into two orthogonal components, and manipulating the phase difference as demand between them. For example, L-shaped [17], [52] nanostructure was reported to support two dipole moments along arms. When incident light is polarized along the axis between arms, it results in a superposition of both dipole moments, which is a clear evidence that the perpendicular components along the arms are excited. Therefore, an abrupt phase continuity was produced and results in polarization manipulation. Examples of other pioneering works including, cross-shaped[1], [53], V-shaped[54], Y-shaped resonator[55], split ring[56], and U-shaped[57] structures were studied to exhibit giant birefringence properties. However, there are specific requirements that must be satisfied for components to achieve linear-to-circular polarization conversion: 1), equal amplitudes. 2), 90 degree phase shift. In the following discussion, three typical mechanisms categorised according to the underling physics to achieve linear-to-circular polarization conversion will be introduced along with published examples.

1) Uniformed metasurface in transmission mode

Early works have shown that uniform metasurfaces designed with an array of identical metallic resonators can be exploited to enable linear-to-circular

polarization conversion. The unit cell is formed by resonators that support an anisotropic optical response, as shown in Figure 2.6 (a). Through the optimization of the resonator geometries, the two orthogonal electric field components can have approximately equal amplitude and a 90 degree phase delay. However, linear-to-circular polarization conversion can be achieved only over a relatively narrow wavelength range (marked in the grey area in Figure 2.6 (a), determined by the overlapping optical response of the electric field vector components. For example, an early work in 2008 demonstrated a split-ring resonator supporting two dipole resonances which was designed into a rectangular shape with different length of bar along x and y-axis to shift away resonances [56]. Figure 2.6 (b) displays the design of the metasurface. Figure 2.6 (c) plots the transmission of the metasurface for x and y-polarized light, where there are two well-separated resonances with the aim of creating a useable bandwidth over which a 90 degree phase shift occurs (for this case is at 0.639THz), as shown in Figure 2.6 (c). Although 99.9% of transmitted beam was circularly polarized according to the axial ratio spectrum, the design is constrained to operate at single wavelength. In addition, the transmission efficiency was only 70%.

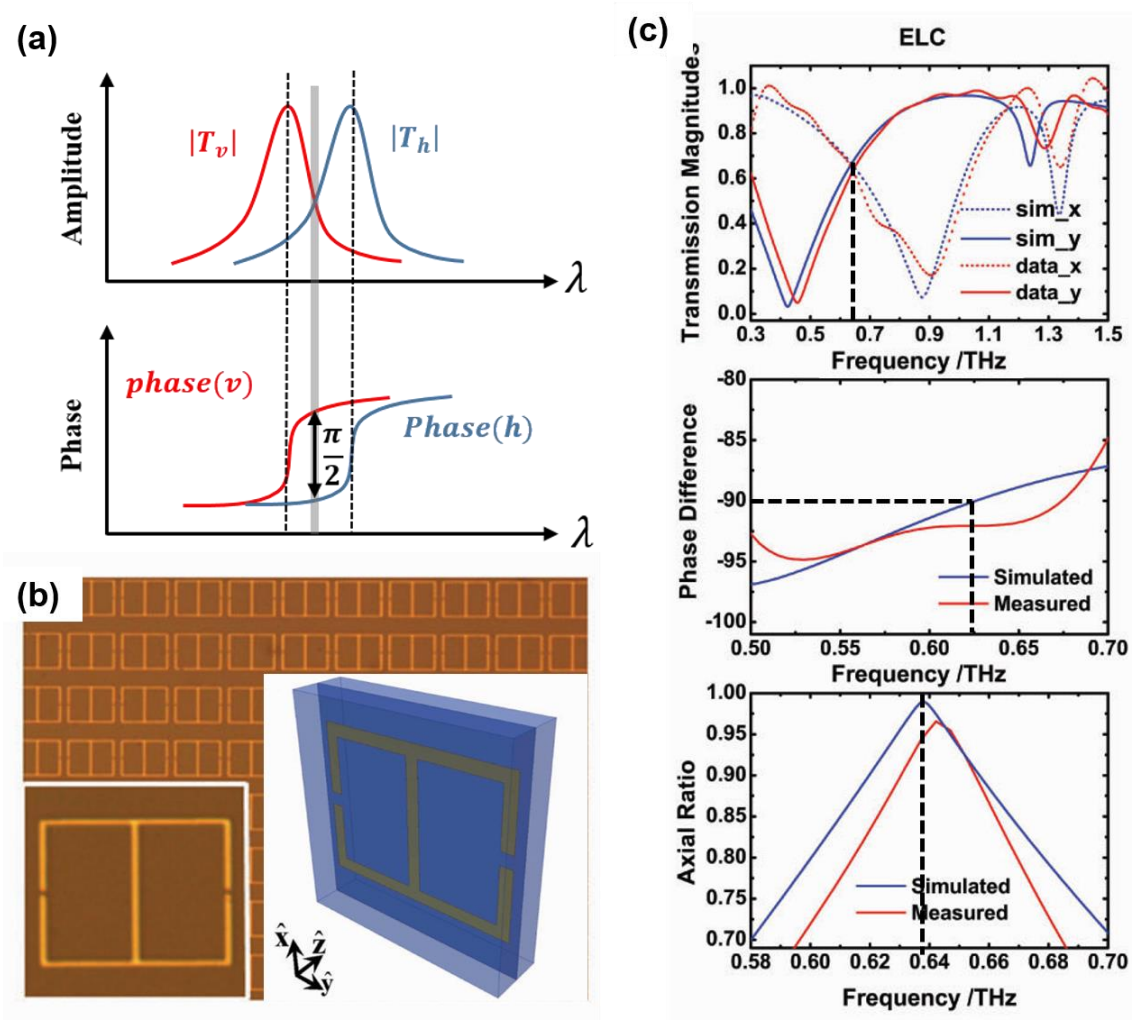

Figure 2.6 The operation principle of uniform metasurface in transmission mode with an example adopted from [56]. *(a) Amplitude and phase spectrum for orthogonal electric field components (E_v, E_h) of uniform metasurface in transmission mode. (b) The picture of waveplate adapted from* [56]. *(c) The simulation and measurement results adopted from* [56]. *They are amplitude, phase difference of x and y polarization, axial ratio of transmission beam.*

As metasurfaces based on an array of identical resonators have narrow bandwidths, their complementary counterparts have studied to allow a 90 degree phase shift in a relatively broad wavelength range [58]. In Figure 2.7, the resonator consists of two orthogonal nano-slits and its complementary structure was studied. As shown in Figure 2.7 (b) and (d), it is clear that both structures support two distinct resonances under x and y-polarized incidence. The same amplitude were produced between resonances at the bandwidth where the phase

difference is close to 90 degree (Figure 2.7 (c) and (e)). By comparing the phase spectrum, it is clear that the complementary structure possesses broader bandwidth allowing 90 degree phase shift. However, despite significant progress achieved to maintaining phase shift, the effective working bandwidth is still narrow as the wavelength range of equal amplitude remain the same. Therefore, subsequent works utilise complementary designs for circular-to-linear polarization conversion [59], [60].

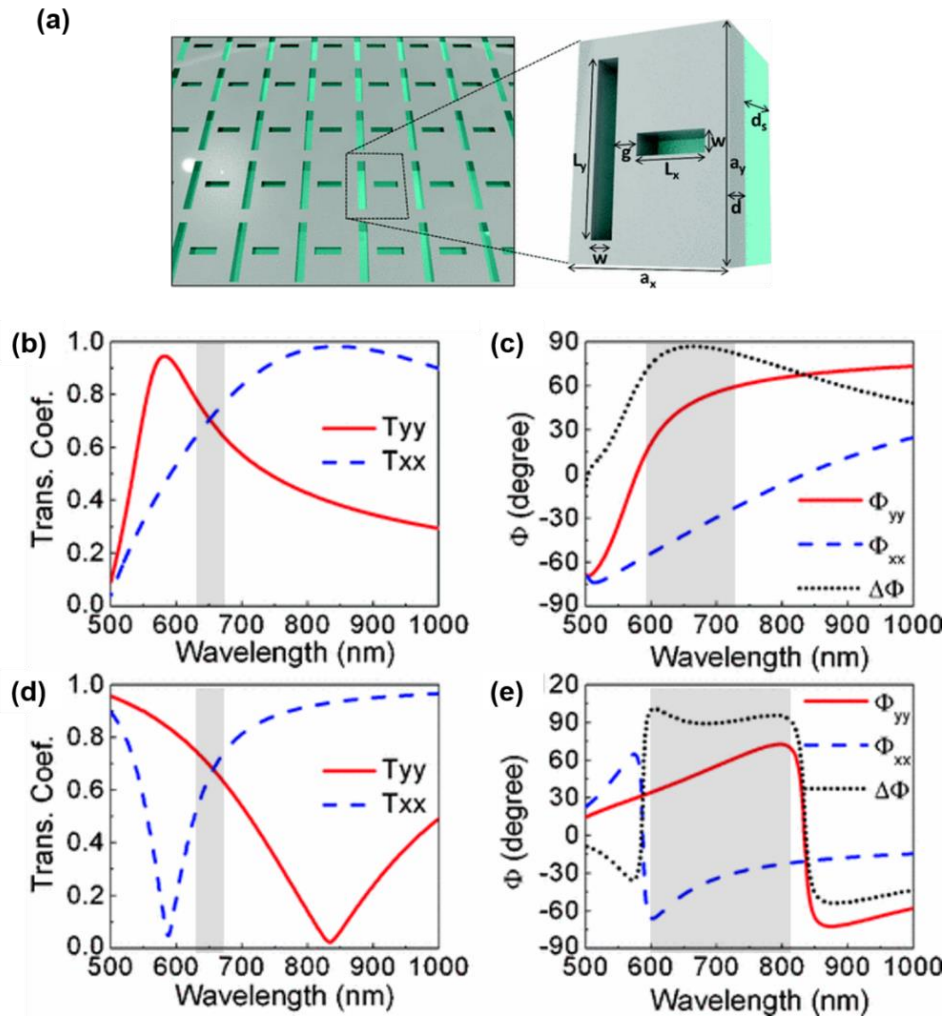

Figure 2.7 Complementary metasurface to enable quarter wave plate. All figures are adopted from [15]*. (a) Schematic diagram of metasurface. (b) Transmission coefficients and (c) phase information for metasurface and similar plots in (d) and (e) for complementary metasurface.*

2) Non-uniform metasurface in transmission mode

Instead of utilizing uniform metasurface where the anisotropic property relies on each identical resonator that supports single resonance, Yu *et al*. [18] investigated a multi-resonances metasurface to achieve broadband polarization manipulation in transmission mode. As shown in Figure 2.8 (b), this particular design consists of subunits which is formed by eight V-shaped antennas, with varying orientation angle and optimized geometry to provide multi-resonances. The effective operation wavelength range was broadened by combining these resonances. The operation principle of non-uniform metasurfaces as broadband quarter waveplate is summarized in Figure 2.8 (a). As the subunits are assembled from the same resonators, the amplitude of decomposed polarizations stay equal over a broad wavelength range which is indicated with the black line by near unit ratio of amplitudes in Figure 2.8 (c). The 90 degree phase difference between the two polarization components of the light as depicted in Figure 2.8 (c) is induced by the offset distance between subunits, rather than a dipole resonance from a single element. Upon excitation of incident light, the metasurface acts like a quarter wave plate, producing two co-propagating waves with equal amplitude as and 90 degree phase difference, bending the light away from the original incident direction through spatial phase gradient. Despite the degree of circular polarization light being over 0.97, as shown in Figure 2.8 (d), one limitation of this approach is that only 10% of the incident light can be scattered and converted into circularly polarized light in this particular case.

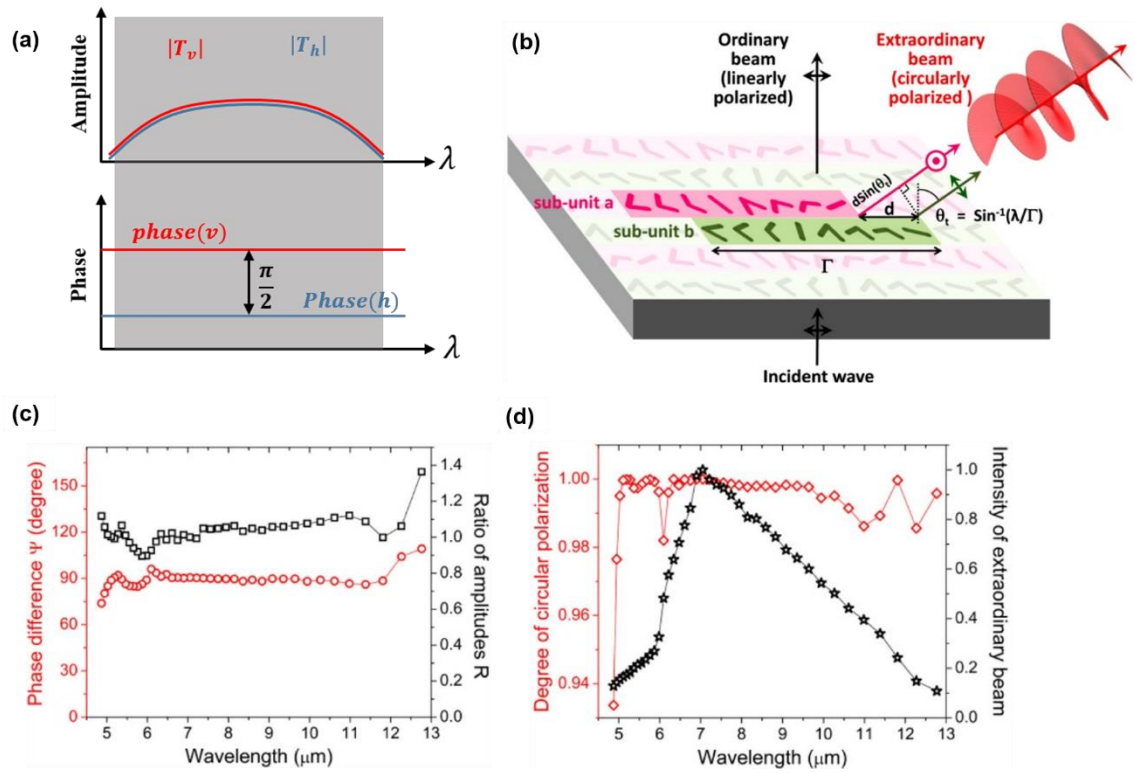

Figure 2.8 The operation principle of non-uniform metasurface in transmission mode with an example adopted from [18]*. (a) Amplitude and phase spectrum for orthogonal electric field components (E_v, E_h) of non-uniform metasurface in transmission mode. (b) The picture of waveplate. (c) The experimental spectrum of phase difference and ratio of reflectivity. (d) The measured spectrum of degree and intensity of circular polarization. (b), (c) and (d) are adopted from* [18]*.*

3) Uniform metasurface in reflection mode

In order to enhance the conversion efficiency, a homogeneous design strategy based on metal-dielectric-metal (MIM) sandwich structure has been widely employed to realise efficient metasurface waveplates [61]–[65]. More specifically, this design is formed by a metallic resonator, dielectric spacer and a metal ground plane. In contrast to previous reported metasurfaces, where light simply excite electric dipole-like resonance, for MIM structure, the incident light is able to propagate through the metasurface and undergo multiple reflections in the dielectric spacer where the light self-interferes. The hybridization of

electromagnetic field interference in dielectric spacer and collective coupling from inter-elements are known as gap-plasmon mode (GSP) [66]. Anders and co-workers [62], demonstrated that the GSP mode excited in MIM structure offer improved degrees of freedom to tailor the spectral dispersion of light, making it promising candidate to design broadband and efficient metasurface waveplates. In this work, they demonstrate a nano-brick metasurface, a typical MIM structure as shown in Figure 2.9. Figure 2.9 (a) displays the spectrum of reflectivity and phase difference for x- and y-polarized light. The GSP mode is excited at 800nm, where the phase shift was maintained at 90 degree with 160nm of effective operation bandwidth. By optimised spacer thickness and resonator size, the GSP mode coupling strength therefore provides high efficient reflectivity for both polarizations. The reflectance shown in Figure 2.9 (b) demonstrates that 82% of light has been converted from circular to linear polarization.

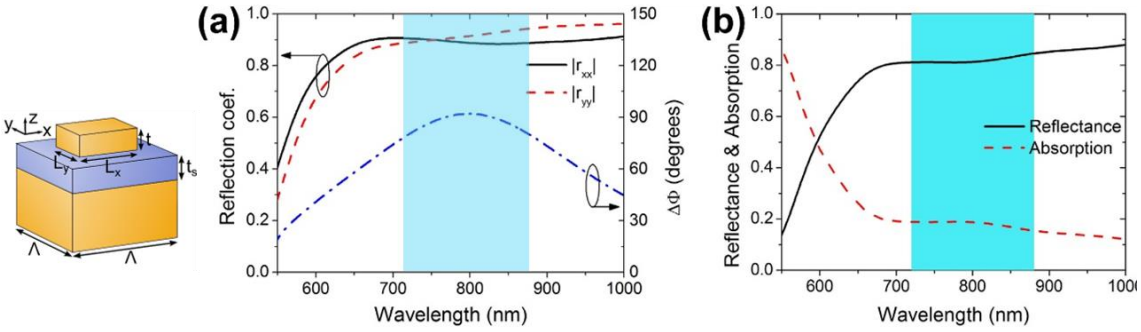

Figure 2.9 (a) Reflectivity and phase difference for x- and y-polarized light. (b) Reflectivity and absorption for circular polarization light.

As discussed above, the GSP mode introduce extra degrees of freedom for phase manipulation, meanwhile reflection is generally low at resonance. Therefore, minimization of the reflection minima becomes the main task for designing subsequent metasurface waveplates, and there is always a trade-off

between additional phase manipulation and high efficiency. In addition, the phase modulation based on excitation of signal resonance inherently limits the effective working bandwidth. Impressively, this issue has been overcome by designing a broadband quarter wave plate that operates in the off-resonance wavelength range, a novel concept (Figure 2.10 (a)) proposed by Chang, *et al* [67] in 2019. The working principle behind this strategy is to design anisotropic resonators that only interact with one polarization to introduce a non-linear phase dispersion as indicated in by red line in Figure 2.10 (a). For orthogonal component excitation, the metasurface become non-resonant which gives near unit reflection efficiency and linear phase dispersion as indicated by blue line in Figure 2.10 (a). As a consequence, an approximately constant phase difference between the orthogonal components over the off-resonance wavelength range allows the design of waveplates operating in broadband wavelength range. In this work, a metasurface based on an array of rod resonators (Figure 2.10 (b)) was investigated to enable broadband linear-to-circular polarization conversion with relatively low loss in reflection mode in the terahertz region. Figure 2.10 (c) and (d) plot the measured reflectivity and phase spectrum for orthogonal polarization. When light is parallel to rod ($r_{\parallel}$), the interaction with rod excite a resonance at 1.3THz (230μm) with an associated minimum in reflection which introduces a nonlinear phase dispersion as shown in Figure 2.10 (d). The mechanism of the observed nonlinear phase modulation is due to the coupling between unit cells and between incoming and outgoing light, and can be understood by modelling the system using coupled mode theory [68]. When light is orthogonal to the rod

(r⊥), there is no interaction and no phase discontinuity. The results shown in Figure 2.10 (e) confirm that the conversion efficiency is largely over 90% from 0.7-1.4THz. In addition, the measured axial ratio as shown in Figure 2.10 (f) is less than 3dB indicating a high degree of circularly polarization light.

Instead of controlling phase response at resonance, this strategy focuses on the off-resonance bandwidth, where ideal quarter wave plates with high efficiency and broadband operation wavelength range become possible. Inspired by this mechanism, we introduce a nanorod-based metasurface operating in the mid-infrared region in chapter 5.

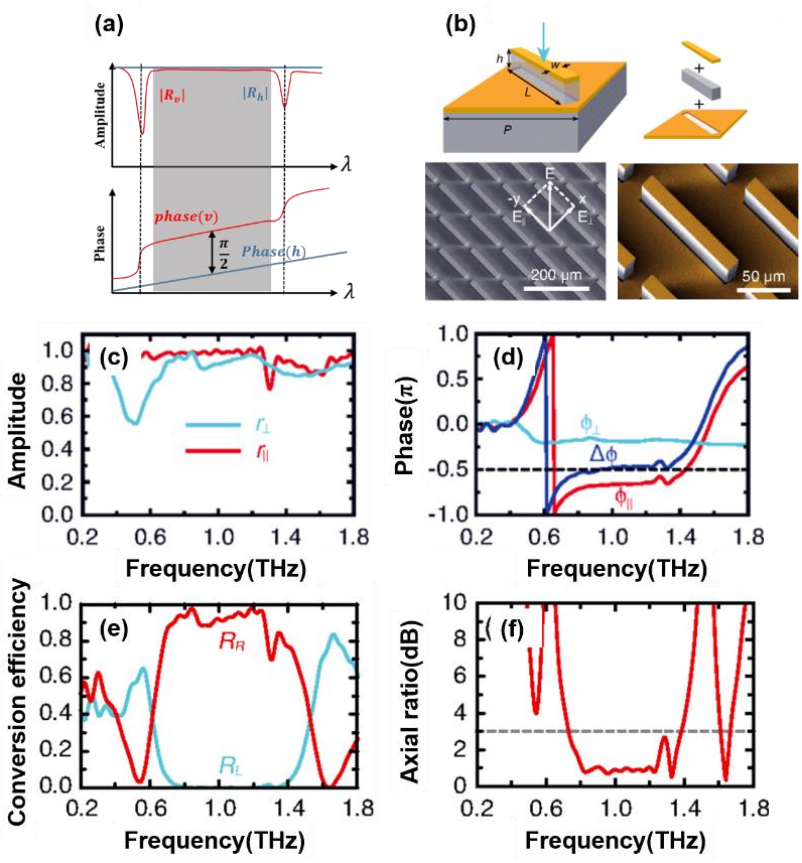

Figure 2.10 (a) The operation principle of uniform metasurface in reflection mode with an example adopted from [67]. *(b) Schematic of the nanorod-based metasurface structure. Measured (c)reflectivity amplitude, (d) phase spectra, (e) conversion efficiency and (f) axial ratio spectrum adopted from* [67].

2.4 Spectroscopy

2.4.1 Infrared spectroscopy

Infrared light is part of the electromagnetic spectrum encompassing wavelengths from around 1mm (300 GHz) to the nominal red edge of the visible spectrum, around 700 nm (430 THz). The infrared region can be further separated into three categories, namely: near infrared, mid infrared and far infrared as shown in Figure 2.11 [69]. The mid-infrared range is of particularly useful because of a technique known as infrared spectroscopy which enable to identify unknown substance and its functional groups [70]. Covalent bonds in molecules experienced two main vibrational motions: stretching and bending at particular frequency. It can absorb infrared light that contain matching frequency. As a consequence, infrared light spectrum will contain absorption dips at multiple frequencies, each of which can be associated with a particular bond type. This absorption spectrum carrying molecular structural information become a unique 'DNA' reflection to identify molecule. Infrared spectroscopy is therefore a powerful, cost-effective, analytic technique that can be used to resolve information on the chemical makeup of almost any sample in almost any state.

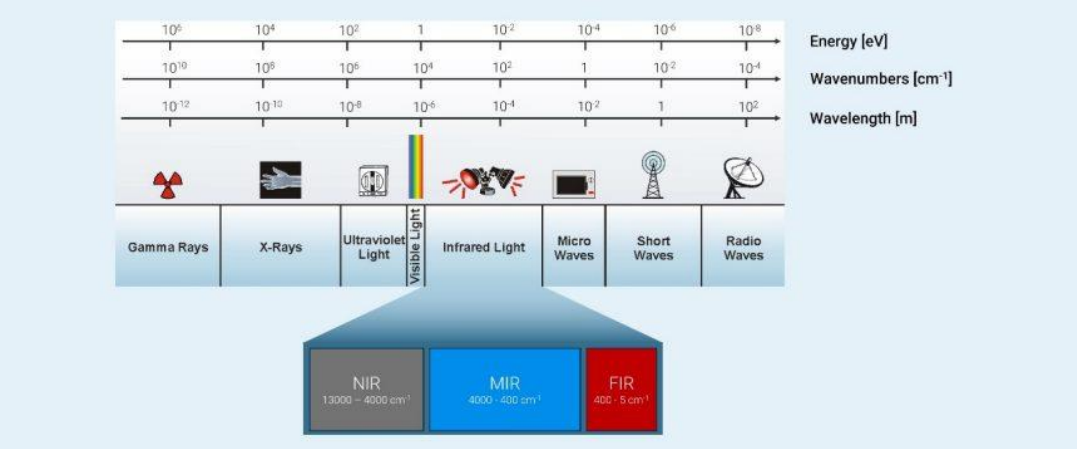

Figure 2.11 Spectrum of electromagnetic wave. illustration is adopted from [69].

2.4.2 Vibrational circular dichroism spectroscopy

Although infrared spectroscopy provides absorption spectra that can identify bonds in molecules, by itself it cannot be used to distinguish chiral enantiomers. In this section, we will introduce concept of chirality and vibrational circular dichroism spectroscopy, which has been widely used for distinguishing chiral enantiomers.

Chirality is a three dimensional geometrical concept that describes a pair of objects that are mirror image to each other, which are not superimposable even by rotations or translations [24]. The word chirality is derived from the Greek χειρ (*kheir*) which means "hand", which is a perfect example of chirality.

Chiral molecules are defined when they cannot be exactly superposed to its mirror configuration of the atoms of the molecule. Figure 2.12 shows the chiral and achiral molecules configuration in the sense of organic chemistry. The chirality is given when a tetrahedral carbon bond with four different substituents.

The sp^3-hybridized centre (usually a carbon) with its substituents are thus asymmetric and is defined as chirality centre [24]. As a comparison, an achiral molecule are however includes some equal substituents therefore symmetric without chirality centre as sown in Figure 2.12.

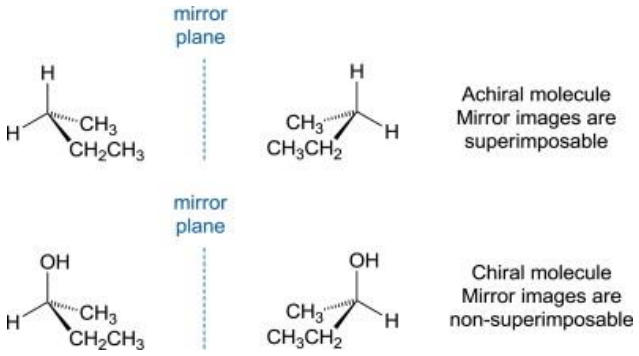

Figure 2.12 Comparison of achiral and chiral molecules. Illustration is adopted from [24].

Chiral molecules share identical atomic elements, as well as chemical bonds, but the reason that makes them different from each other is attributed to the spatial arrangement of atomic particles in three-dimensional space. A pair of molecules with chiral arrangement is known as enantiomers [24]. The concept of chirality is very important in organic and biological molecules.

Chiral materials/molecules are especially unique due to the fact that the interaction with circularly polarized light can cause chiroptical effect, including optical activity linking to the degree of polarization rotation and circular dichroism which defines the different absorption to right- and left-handed circularly polarized light [6]. Based on a fact that a pair of enantiomers shows mirror symmetric spectra with identical amplitude but opposite sign under circular polarization excitation, a powerful tool known as circular dichroism spectroscopy has been developed and widely used to detect and distinguish enantiomers [5], [71]–[73].

In the work described in this thesis, we are concerned about an extension to this known as vibrational circular dichroism spectroscopy [74], which is particularly focused on exploiting circular dichroism response in mid-infrared region. Because the circular absorption is associated with the infrared vibrational absorptions bands, the measured circular dichroism spectra yields the handedness of enantiomers, and more importantly the spectra contains absolute configuration of a chiral molecule. With these benefits, this techniques is realising its potential as a powerful stereochemical tool for chiral structure elucidation.

2.4.3 Chiral sensing based on metasurface

However, the vibrational circular dichroism of most small molecules in nature is intrinsically weak due to the mismatch size of small molecules and relatively big wavelength of light. The factor of 10^{-3} to 10^{-6} for the differential right circularly polarised (RCP)/ left hand polarised (LCP) absorption is typical for vibrational circular dichroism [26]. Although this is measurable with tools such as lock-in amplifiers, and high sensitive liquid nitrogen cooled detectors, vibrational circular dichroism still suffer from low signal-to-noise ratio. Therefore, enhancing vibrational circular dichroism are major challenge for efficient enantiomer-selective sensing system.

In order to improve the sensitivity, substantial effort has been devoted to investigate the insight mechanism of near-field interaction. It has been reported that the optical chirality density which describe the chirality of electromagnetic field is suggested as the main mechanism offering enhancement of circular

dichroism spectroscopy [75]. The computed optical chirality density in the vicinity of a material enables to evaluate the strength of chiroptical interactions between local electromagnetic field with chiral molecules due to the fact that optical chirality density carry expressions for enantio-selective absorption for chiral molecules [76]. Based on the work from D.M.Lipkin [77], Tang and co-worker identified locally electromagnetic chirality for time-harmonic field in free space in its time-average form [76]:

$$C(\boldsymbol{r}) = -\frac{\omega\varepsilon_0}{2} Im(\boldsymbol{E}^*(\boldsymbol{r}) \times \boldsymbol{B}(\boldsymbol{r})) \tag{2.35}$$

where ω is the angular frequency, ε_0 is electric permittivity of free space, $\boldsymbol{E}^*$ and $\boldsymbol{B}$ are the complex conjugate electric and magnetic field vectors, respectively. Tang and co-worker discovered that equation (*2.35*) appears in the expression of rate of excitation for chiral molecules and identified that $C(\boldsymbol{r})$ determines the differential absorption of chiral molecules with left- or right-handed circularly polarized light therefore it was recognised as the quantity of chirality. Based on equation (*2.35*), chirality is nonzero only when some electric and magnetic components are parallel and exhibit phase shift. In this context, circularly polarized light is the best exemplification because its electric and magnetic field are parallel and out of phase. For circularly polarized light in free space, the optical chirality density is:

$$C_{CPL}^{\pm} = \pm\frac{\omega\varepsilon_0}{2c}|E_0|^2 \tag{2.36}$$

where $\pm$ represent for left-handed circularly polarized light $(+)$ and right-handed circularly polarized light $(-)$, E_0 is the magnitude of the incident electric field.

Equation (*2.36*) displays that the optical chirality density for plane wave is limited by circular polarization sate.

Recently, it has been reported that engineered plasmonic nanostructures are able to generate optical chirality density in the vicinity of structure enhanced by a few orders magnitude or more than that induced by circularly polarized light without resonators [5], [72], [78], [79]. For this reason, the enhanced chiral field has been known as superchiral field [71], [73]. The limits of optical chirality density can be overcome by plasmonics/dielectric metamaterials which excel at focusing light on nanoscale creating intense light field on the surface. As a consequence, the enhanced local electric field can achieve few orders of magnitude than plain film which make the contribution on chirality enhancement. In addition, by forming geometric dissymmetry of structure (such as chiral shape), the local electromagnetic field can become far more twisted than circularly polarized light, resulting in a superchiral field. With these advantages, metamaterials are able to provide a powerful platform for strong interaction between local fields and molecules. The local enhancement of optical chirality generated by nanostructure is quantified with the optical chirality density normalised by that for circularly polarized light:

$$\hat{C}(\boldsymbol{r}) = \frac{C^{\pm}}{C^{\pm}_{CPL}} = -\frac{c}{|E_0|^2} Im(\boldsymbol{E}^*(\boldsymbol{r}) \cdot \boldsymbol{B}(\boldsymbol{r})) \tag{2.37}$$

$C^{\pm}_{CPL}$ are the reference values calculated under circularly polarized incident light without resonators. Equation (*2.37*) indicates that superchiral field is spatially variable, the sign corresponds to its handedness and the region with magnitude

of $\left|\hat{C}(\boldsymbol{r})\right| > 1$ is so called superchiral field with the enhancement could be at few order of magnitude larger than expected for circularly polarized light depending on structure.

In the following discussion, we will briefly introduce three different strategies to generate strong near-field chirality based on chiral structure. In general, chiral plasmonic nanostructure with intrinsic dissymmetry in geometry exhibits advantages of producing local electromagnetic field with greater chirality. In reference [78], the authors aim to explore the chiroptical near-field response of multiple planar and three-dimensional chiral structure. It was concluded that compact three-dimensional structure such as stereometamaterials composed by overlapping resonators in space or 3D helixes are the better candidate to increase the chiral response, rather than a planar metasurface. However, as strong superchiral field are located inside 3D centre, it is challenging to locate molecules at the customised region. Therefore, planar chiral structures with easier fabrication are preferred in practical situation for chiral molecule sensing.

As indicated in equation (*2.37*), a rather straightforward design strategy to create chirality density in a planar structure is by establishing an electric field that has a component parallel to the magnetic field with certain phase shift. Early work from Hendry and co-workers [80] assemble pairs of nanoslit with certain displacement as shown in Figure 2.13 (a). The physical mechanism can be understood with Babinet's principle where an electric dipole can be excited with nanorod as shown in Figure 2.13 (a). By applying Babinet's principle, a nanoslit can excite a magnetic diploe with strong magnetic field at the ends, and a strong electric field

in centre. By staggering nanoslits with a displacement, the electric and magnetic field can overlap in the middle of slit and generate chiral field. The computed chirality at the centre of structure is plotted in spectrum in Figure 2.13 (a) where a symmetric pattern was observed for nanoslit and its mirror-imagined structure. This is an indicator of strong chiroptical response. A similar structure composed of staggered nanorods was design to excite superchiral field as shown in Figure 2.13 (b). Displacement between nanorods allows the localised electric field overlap with the magnetic field thereby producing strong near-field chirality between gaps. This approach has been widely used for enantiomer sensing such as detection of alanine enantiomer based on vibrational circular dichroism spectroscopy [81]. The spatial distribution of superchiral field show that the maximum chirality is localised at the gap between rods with the handedness opposite signs for left- and right-handed chiral structures. Following similar mechanism of Babinet's structure, Tullius and co-workers [73] introduced a novel way of overlapping electric and magnetic fields. The structure is shown in Figure 2.13 (c), consisting of a solid 'shuriken' chiral nanostructure overlapping with indentation of identical structure. The purpose of this particular arrangement is to overlap the equivalent electric and magnetic fields in the solid and inverse structure. It is demonstrated that by controlling the film thickness, the coupling between top and bottom layer can be tailored to generate chiral optical properties. This design has been widely used to detect the higher order structures of biomolecules.

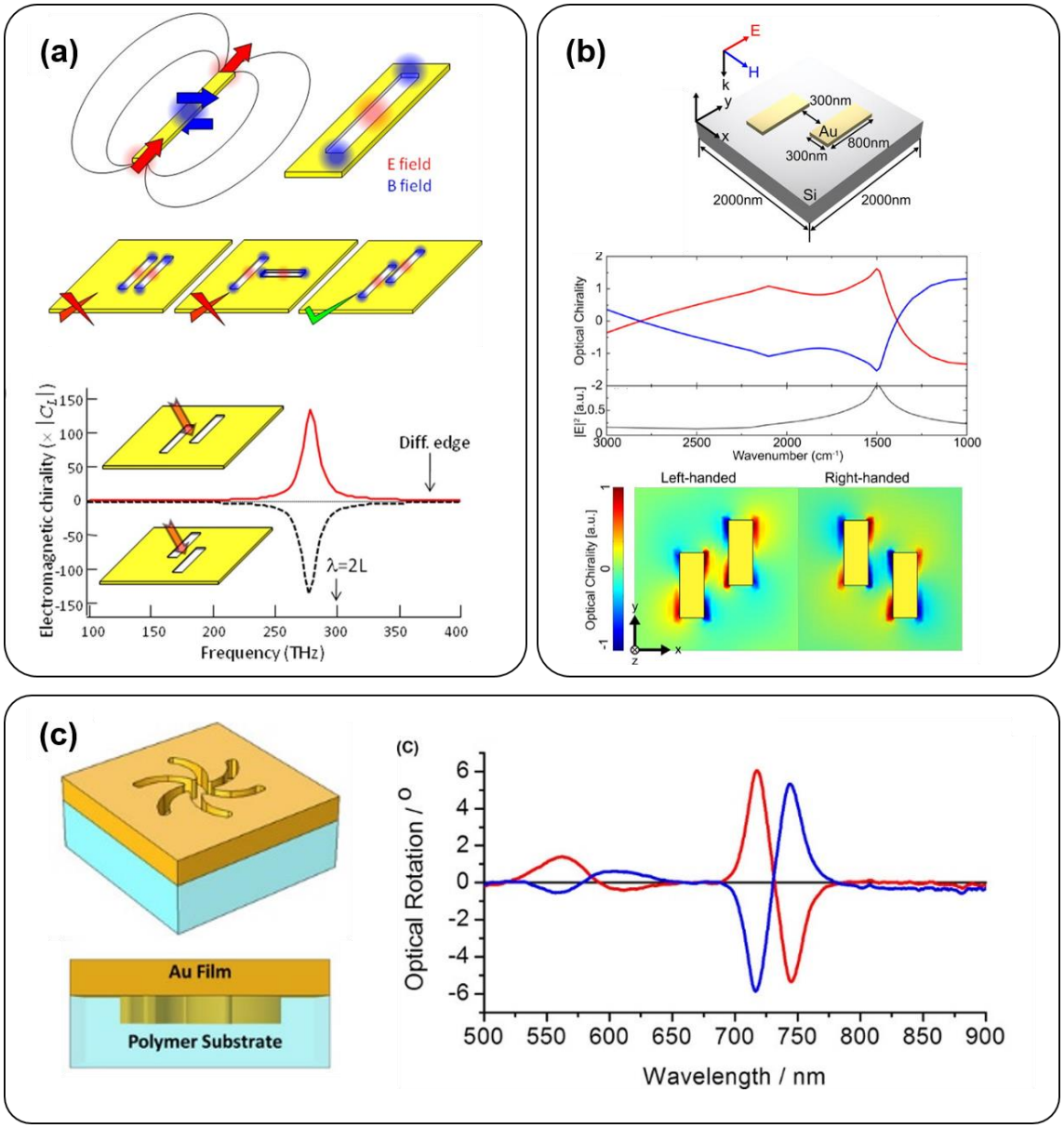

Figure 2.13 (a ⅰ) Dipole resonance of nanorod, red and blue area indicates enhanced electric and magnetic field. (a ⅱ) Dipole resonance of a nanoslit. (a ⅲ) Pairing arrangement of nanoslits. Only the arrangement on the right enable to excite chirality in near-field. (a ⅳ) Local chirality at centre of unit cell as a function of frequency, black dash line shows the chirality for mirror-imagined structure. (a) is adopted from [80]*. (b ⅰ) Nanorod metasurface. (b ⅱ) Chirality at central of metasurface for left- and right-handed structure as a function of wavenumber. (b ⅲ) Colormap of chirality for metasurface. (b) is adopted from* [81]*. (c ⅰ) Schematic of 'shuriken' metasurface. (c ⅱ) Optical rotation spectrum for left- and right-handed structure. (c) is adopted from* [73]*.*

2.5 Summary

This chapter introduced three categories of polarization states of electromagnetic plane wave and provided two criteria that must be met to achieve linear-to-circular polarization conversion: 1) 90 degree phase shift and 2) equal amplitude of decomposed polarizations, which is a key concept for designing metasurface based quarter waveplates. In addition, we introduced Stokes parameters which are a group of measurable parameters to characterise the actual polarization state of plane waves. In Chapter 5, the utilisation and measurement of Stokes parameters will be discussed with more detail. Next, typical examples of metasurface quarter-wave plates, along with their advantages and drawbacks including narrow bandwidth and high loss, were then described. This led to the introduction of the design used in this work, which is holds promise for addressing these challenges. With the aim of practical application in metasurface-enhanced chiral sensing, we introduced the chiroptical effect of chiral molecules, and techniques including infrared spectroscopy and vibrational circular dichroism spectroscopy which are core for enantiomer sensing. Finally, a brief overview of chiral metasurface enabled enantiomer sensing was discussed

Numerical modelling underpins and enables much optical nanostructure research, and in the next chapter we will introduce the simulation technique that was used to study the metasurface in this thesis.

3 Finite Difference Time Domain (FDTD) solver introduction

3.1 Introduction

Finite difference time domain (FDTD) method is a computational technique that enables the solution of Maxwell's equations by discretized equation and space through the finite-difference principle in the time domain. It was originally proposed by Kane S.Yee in 1966 [82] where he derived a full three-dimensional formulation, but only validated the method in two-dimensions. Later in 1975, Taflove [83] and Brodwin [84] applied Yee's method in three-dimensions to solve the scattering by dielectric cylinders which has driven the growth of the FDTD method in the decades after it was first proposed. Building on the rapid advances in computer technology, Yee's algorithm for is recognised as the fast numerical way of solving Maxwell's equations, and therefore complex electromagnetic problems.

This chapter is divided into five sections. The first section is an introduction of Maxwell's equations, and is followed by the description of Yee's method to solve the Maxwell's equations in the second section. The third section covers the details of setting up a simulation using the commercial software Lumerical FDTD solutions. This contains the materials setting, boundary conditions, mesh setting and normalisation that was applied to study nanorod-based metasurfaces discussed in this thesis. The next section focuses on visualisation of simulation

results, including field profile and optical spectrum and post data processing in the Lumerical software to analysis data. Finally, the last section describes the optimization of simulation structure and convergence testing to guarantee the accuracy of the simulation results.

3.2 Maxwell's equations

Maxwell's equations which govern optical and electromagnetic phenomena are a set of four equations that show the mathematical relationship of the electromagnetic fields. In the time domain, these can be described as:

(1) Faraday's Law

$$\nabla \times \boldsymbol{E} = -\frac{\partial \boldsymbol{B}}{\partial t} \tag{3.1}$$

(2) Ampere's Law

$$\nabla \times \boldsymbol{H} = \frac{\partial \boldsymbol{D}}{\partial t} + \boldsymbol{J} \tag{3.2}$$

(3) Gauss's Law

$$\nabla \cdot \boldsymbol{D} = \rho \tag{3.3}$$

(4) Gauss's Law for magnetism

$$\nabla \cdot \boldsymbol{B} = 0 \tag{3.4}$$

where MKS units are used. These equations link the four macroscopic fields $\boldsymbol{E}$ electric field intensity (V/m), $\boldsymbol{H}$ magnetic field intensity (A/m), $\boldsymbol{B}$ magnetic flux density (Wb/m^2) and $\boldsymbol{D}$ electric flux density(C/m^2) with external $\boldsymbol{J}$ electric current density (A/m^2) and ρ electric charge density (C/m^3). Throughout the

mathematical analysis of this chapter, for reasons of simplicity, the medium, is considered to be isotropic, homogeneous and linear. With this condition, these four macroscopic fields are further linked:

$$\boldsymbol{D} = \varepsilon \boldsymbol{E} = \varepsilon_0 \varepsilon_r \boldsymbol{E} \tag{3.5}$$

$$\boldsymbol{B} = \mu \boldsymbol{H} = \mu_0 \mu_r \boldsymbol{H} \tag{3.6}$$

where ε_0 ($8.854 \times 10^{-12} F/m$) and μ_0 ($4\pi \times 10^{-7} H/m$) are the electric permittivity and magnetic permeability of vacuum, respectively. ε_r and μ_r are the relative permittivity and magnetic permeability of the media.

In the Cartesian coordinate system, the time-domain Maxwell's equations have six electromagnetic components: E_x, E_y, E_z, H_x, H_y and H_z. The subscript refers to the projection of the field on the corresponding axis. Faraday's law can be described as:

$$\frac{\partial E_y}{\partial z} - \frac{\partial E_z}{\partial y} = \mu \frac{\partial H_x}{\partial t} \tag{3.7}$$

$$\frac{\partial E_z}{\partial x} - \frac{\partial E_x}{\partial z} = \mu \frac{\partial H_y}{\partial t} \tag{3.8}$$

$$\frac{\partial E_x}{\partial y} - \frac{\partial E_y}{\partial x} = \mu \frac{\partial H_z}{\partial t} \tag{3.9}$$

Similar to (1) Ampere's Law:

$$\frac{\partial H_z}{\partial y} - \frac{\partial H_y}{\partial z} = \varepsilon \frac{\partial E_x}{\partial t} + J_x \tag{3.10}$$

$$\frac{\partial H_x}{\partial z} - \frac{\partial H_z}{\partial x} = \varepsilon \frac{\partial E_y}{\partial t} + J_y \tag{3.11}$$

$$\frac{\partial H_y}{\partial x} - \frac{\partial H_x}{\partial y} = \varepsilon \frac{\partial E_z}{\partial t} + J_z \tag{3.12}$$

3.3 Finite-difference Time Domain (FDTD) algorithm and software

All of these first-order spatial derivatives and time derivative can be approximated via central differences. For instance, the first-order derivative with respect to x for the formulation $f(x)$ can be approximated with second-order accuracy by:

$$\frac{\partial f(x)}{\partial x} = \frac{f\left(x + \frac{\Delta x}{2}\right) - f\left(x - \frac{\Delta x}{2}\right)}{\Delta x} + O\left(\frac{\Delta x^2}{4}\right) \tag{3.13}$$

This central difference approximation is the foundation of FDTD's algorithm which provide discrete solutions to Maxwell's equations [85]. In Yee's method [82], the simulation geometry is discretized into a regular and rectangular grid in three dimension with grid step of Δx, Δy and Δz along each axis, as illustrated in Figure 3.1 . As mentioned previously, Maxwell's equations are solved on a Yee cell in both space and time, as a result, the electric and magnetic field are also discrete accordingly. In this system, the coordinate of a node of the grid can be described in discrete form as:$(x, y, z)_{i,j,k} = (i\Delta x, j\Delta y, k\Delta z)$, where i, j, k are integers referring to the location of the unit cell. In terms of temporal discretisation the time can be

expressed by: $t = n\Delta t$. The electric and magnetic field are discretized as $\boldsymbol{E}^{n\Delta t}_{i\Delta x, j\Delta y, k\Delta z}$ and $\boldsymbol{H}^{n\Delta t}_{i\Delta x, j\Delta y, k\Delta z}$.

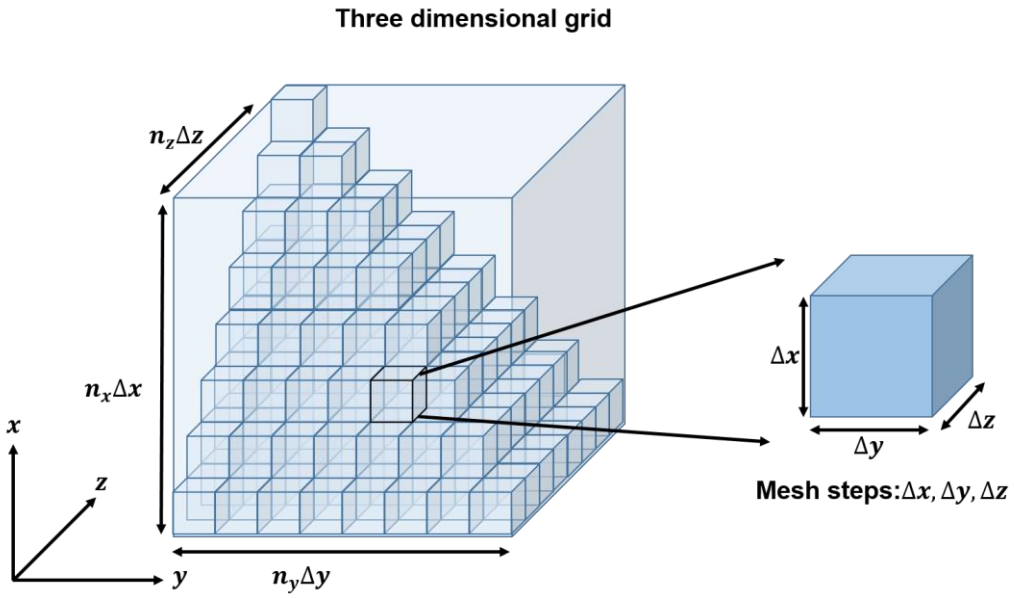

Figure 3.1 Cubic grid defined in Yee's method.

The novelty of Yee's method is the staggering of the electric and magnetic field in both space and time. In other words, rather than locating all the field components at a single point within a grid cell, Yee's method interlaced E- and H-field in a primary grid and a secondary grid, separately as shown in Figure 3.2.

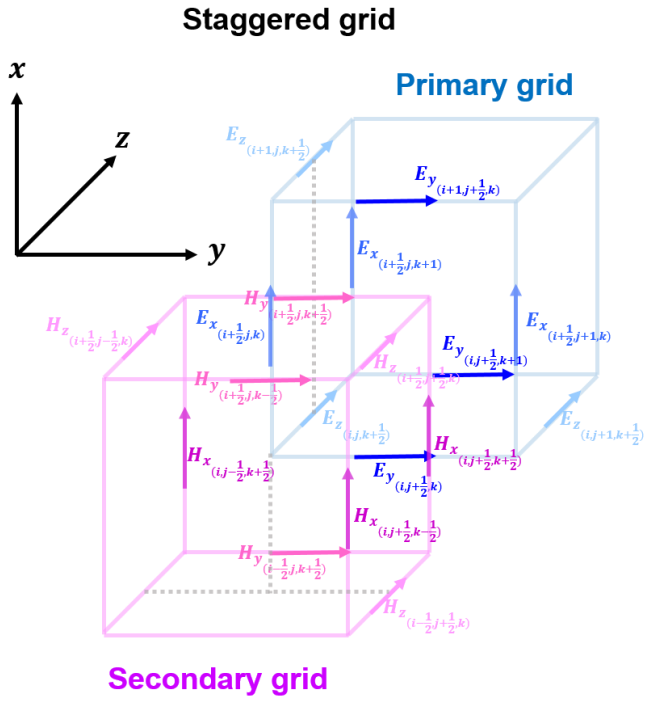

Figure 3.2 Staggered grid

In this primary grid, the electric field vector has components along x, y, z axis and is projected along the grid edge. As shown in Figure 3.2, the projections of magnetic field is at centre and orthogonal to grid face. Then the Faraday's Law become:

$$\frac{E_{y_{i,j+\frac{1}{2},k+1}}^{n+\frac{1}{2}} - E_{y_{i,j+\frac{1}{2},k}}^{n+\frac{1}{2}}}{\Delta z} - \frac{E_{z_{i,j+1,k+\frac{1}{2}}}^{n+\frac{1}{2}} - E_{z_{i,j,k+\frac{1}{2}}}^{n+\frac{1}{2}}}{\Delta y} = \mu \left(\frac{H_{x_{i,j+\frac{1}{2},k+\frac{1}{2}}}^{n+1} - H_{x_{i,j+\frac{1}{2},k+\frac{1}{2}}}^{n}}{\Delta t} \right) \tag{3.14}$$

$$\frac{E_{z_{i+1,j,k+\frac{1}{2}}}^{n+\frac{1}{2}} - E_{z_{i,j,k+\frac{1}{2}}}^{n+\frac{1}{2}}}{\Delta x} - \frac{E_{x_{i+\frac{1}{2},j,k+1}}^{n+\frac{1}{2}} - E_{x_{i+\frac{1}{2},j,k}}^{n+\frac{1}{2}}}{\Delta z} = \mu\left(\frac{H_{y_{i+\frac{1}{2},j,k+\frac{1}{2}}}^{n+1} - H_{y_{i+\frac{1}{2},j,k+\frac{1}{2}}}^{n}}{\Delta t}\right) \tag{3.15}$$

$$\frac{E_{x_{i+\frac{1}{2},j+1,k}}^{n+\frac{1}{2}} - E_{x_{i+\frac{1}{2},j,k}}^{n+\frac{1}{2}}}{\Delta y} - \frac{E_{y_{i+1,j+\frac{1}{2},k}}^{n+\frac{1}{2}} - E_{y_{i,j+\frac{1}{2},k}}^{n+\frac{1}{2}}}{\Delta x} = \mu\left(\frac{H_{z_{i+\frac{1}{2},j+\frac{1}{2},k}}^{n+1} - H_{z_{i+\frac{1}{2},j+\frac{1}{2},k}}^{n}}{\Delta t}\right) \tag{3.16}$$

The discrete form of Ampere's law is conducted via a secondary Yee cell as shown in Figure 3.2. The secondary cell is equal to the primary cell but located at the centre of the primary grid. This means the edges of the secondary cell are normal to the grid faces of the primary cell. As a result, the magnetic field components line along the edge of the secondary cell whereas the electric field is sampled at the centre of grid face. Ampere's law is expressed in a discrete form as:

$$\frac{H_{z_{i+\frac{1}{2},j+\frac{1}{2},k}}^{n} - H_{z_{i+\frac{1}{2},j-\frac{1}{2},k}}^{n}}{\Delta y} - \frac{H_{y_{i+\frac{1}{2},j,k+\frac{1}{2}}}^{n} - H_{y_{i+\frac{1}{2},j,k-\frac{1}{2}}}^{n}}{\Delta z} = \varepsilon\left(\frac{E_{x_{i+\frac{1}{2},j,k}}^{n+\frac{1}{2}} - E_{x_{i+\frac{1}{2},j,k}}^{n-\frac{1}{2}}}{\Delta t}\right) + J_{x_{i+\frac{1}{2},j,k}}^{n} \tag{3.17}$$

$$\frac{H_{x_{i,j+\frac{1}{2},k+\frac{1}{2}}}^{n} - H_{x_{i,j+\frac{1}{2},k-\frac{1}{2}}}^{n}}{\Delta z} - \frac{H_{z_{i+\frac{1}{2},j+\frac{1}{2},k}}^{n} - H_{z_{i-\frac{1}{2},j+\frac{1}{2},k}}^{n}}{\Delta x} = \varepsilon \left(\frac{E_{y_{i,j+\frac{1}{2},k}}^{n+\frac{1}{2}} - E_{y_{i,j+\frac{1}{2},k}}^{n-\frac{1}{2}}}{\Delta t} \right) + J_{y_{i,j+\frac{1}{2},k}}^{n} \tag{3.18}$$

$$\frac{H_{y_{i+\frac{1}{2},j,k+\frac{1}{2}}}^{n} - H_{y_{i-\frac{1}{2},j,k+\frac{1}{2}}}^{n}}{\Delta x} - \frac{H_{x_{i,j+\frac{1}{2},k+\frac{1}{2}}}^{n} - H_{x_{i,j-\frac{1}{2},k+\frac{1}{2}}}^{n}}{\Delta y} = \varepsilon \left(\frac{E_{z_{i,j,k+\frac{1}{2}}}^{n+\frac{1}{2}} - E_{z_{i,j,k+\frac{1}{2}}}^{n-\frac{1}{2}}}{\Delta t} \right) + J_{z_{i,j,k+\frac{1}{2}}}^{n} \tag{3.19}$$

These six first-order difference equations are the fundamental principle of the FDTD method. The staggering of the fields in space determine that the electric fields are solved at time $n+\frac{1}{2}$,whilst magnetic fields are solved at time n. The first step of the FDTD algorithm is to initialise field values as zero: $\boldsymbol{E}^{-\frac{1}{2}} = \boldsymbol{H}^{0} = 0$. It is clear from Ampere's law that $\boldsymbol{E}^{n+\frac{1}{2}} = \boldsymbol{E}^{n-\frac{1}{2}} + \frac{\Delta t}{\varepsilon}\boldsymbol{\nabla} \times \boldsymbol{H}^{n} + \boldsymbol{J}^{n}$, thus the electric field at the time $n+\frac{1}{2}$ can be solved using the electric field at the previous time, and the magnetic field at time of n. This process is shown in Figure 3.3. It is clear from Faraday's law that H_x^{n+1} can be solved if $E_y^{n+\frac{1}{2}}$, $E_z^{n+\frac{1}{2}}$ and H_x^{n} are known at all spatial samples. Therefore, once the electric field has been updated to time $+\frac{1}{2}$,

the magnetic field can be updated to time step of $n+1$ based on the function of $\boldsymbol{H}^{n+1} = \boldsymbol{H}^{n} - \frac{\Delta t}{\mu}\boldsymbol{\nabla} \times \boldsymbol{E}^{n+\frac{1}{2}}$. This repetitive process, as shown in Figure 3.3, allows the electric and magnetically fields to be continuously updated as the time step increases, until the termination point.

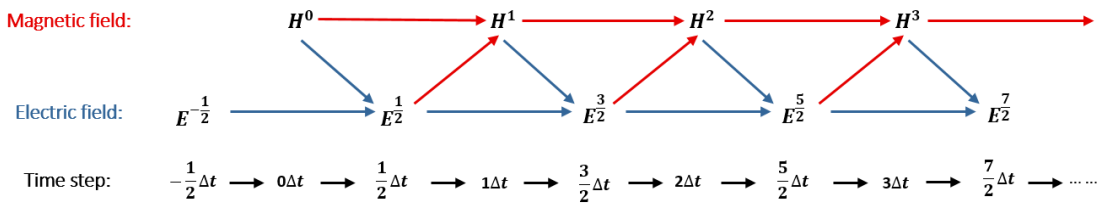

Figure 3.3 Data processing steps in FDTD methods

Consequently, the interlaced electric and magnetic fields in space and time provide a recursive scheme to solve Maxwell equation with second-order accuracy of the central difference operators. In addition to that, there are other advantages to use staggered grid. First, the electric and magnetic fields in staggered grid are divergence free, as a result, the field satisfies Gauss's Law solely [85]. Second, the permittivity ε is also discretized to correspond to each component in Yee the cell [85]. This is very beneficial when an interface passes through a Yee cell, as each component could be located in a different media due to the different spatial point, as a result, the permittivity is assigned accordingly to the component for more accurate results. Last but not the least, the physical boundary conditions are automatically satisfied in the staggered grid.

There are approximately 30 commercial software packages available that utilise the FDTD method to investigate the fundamental electromagnetic properties of a media. Lumerical FDTD Solutions [86], which is specialised for optical simulations,

was chosen to conduct all the numerical simulations described in this thesis. This is a widely used simulation software and mainly focus on photonics, plasmonics, and other areas when the objective feature size is on the order of the wavelength. The software offers a user-friendly graphical interface for setting up simulations, and allows users to the plot power efficiency spectrum and field distributions. In addition, the integrated function provide extensive post-processing and scripting capabilities such as to visualise field profile, allowing the analysis of results, and the optimisation of structures.

3.4 Simulation Setup

3.4.1 Structures and materials

Physical structure can be added by clicking the corresponding icon button where FDTD provide the primitives shape, for instance, triangle, rectangle, circle, etc. The size and thickness of the object can be specified by defining the geometric parameters. The material can be specified by mesh order in the case of overlapping areas.

Once structures are built, materials can be added to corresponding shapes. Some of most common and well-studied materials, for example, gold, silver, silicon, etc. are available for use in FDTD material database, but users can also define complex materials using measurement data, theoretical results or parameterized models. For the metasurfaces discussed in this thesis, silicon dioxide, gold and aluminium are the main materials used in simulations.

Silicon dioxide is a dispersive material over the mid-infrared region. For the structures studied in this thesis, silicon dioxide is defined with sampled 3D data mode by experimental data from Palik [87] consisting of the real and imaginary part of refractive index as a function of wavelength.

The relative permittivities of gold and aluminium are defined using the Drude model:

$$\varepsilon_{total}(f) = \varepsilon + i\frac{\sigma}{2\pi \cdot f\varepsilon_0} \tag{3.20}$$

where ε is the permittivity, σ is conductivity with units of $(\Omega m)^{-1}$, and f is the frequency. In FDTD, the conductive 3D mode is used to define material following equation (*3.20*) where permittivity $\varepsilon = 1$ and σ is the corresponding conductivity. Values of the conductivity for the gold and aluminium are set as $4.5 \times 10^7/\Omega m$ and $3.75 \times 10^7/\Omega m$ respectively to be consistent with those used in previously reported mid-infrared studies [88], [89].

Defining the material is important in simulations as the dispersion properties of materials contribute significantly to differences with experimental results. In the FDTD method, it is not possible to use the dispersive refractive index defined by the user straight away. Instead, the FDTD will reset a set of data according to provided data for the material to fit the model that can be solved efficiently through FDTD algorithm. Therefore, it is important to obtain a good fit especially for highly dispersive materials. Material explorer is provided to check the materials fits. If the fit is not good enough, tolerance and max coefficient can be adjusted to improve the fit. However. There is a trade-off between simulation time and

accuracy so it is important to consider the acceptable level of error and efficient simulation time. More details will be discussed in the section on convergence tests.

3.4.2 Source and Monitor

The plane wave source is used to inject electromagnetic wave along a plane in three dimensional simulations. Period plane wave type is used when investigating periodic system such as periodic metasurfaces. The polarization state of the incident wave can be set through polarization angle. The amplitude of the source is set as 1 for simplicity. Monitors can be added into simulation region to collect spatial simulation data in frequency domain including near-field profiles, far-field projections and refractive index. Multiple monitors can be grouped by analysis, which allows the efficient use of multiple monitors, and the associated script functions allow user to obtain more complicated results such as complex reflection S-parameter coefficients with its phase information rather than raw monitor data.

3.4.3 FDTD solver

FDTD solver is the defined region that is applied with FDTD algorithm to solve Maxwell's equations. Figure 3.4 (a) displays the illustration of FDTD solver region in a perspective view which are indicated by an orange cuboid. In this region, the unit cell is placed in the middle, plane wave source and monitors are added to excite metasurface and record data. Among the various parameters in FDTD

solver, the mesh size and boundary conditions are of the most important settings in making sure that results are accurate.

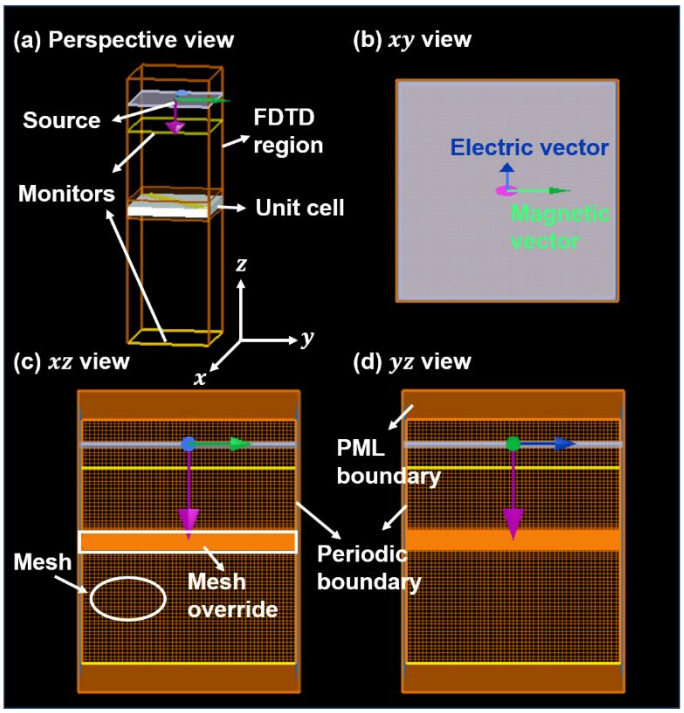

Figure 3.4 The illustration of FDTD solver region for nano-rod based metasurface in (a) perspective view (b) xy view (c) xz view and (d) yz view.

As the electromagnetic field are characterised at each mesh point, a finer mesh can provide higher accuracy of the results. However, as the mesh size become smaller, the required simulation time and memory space increases. Therefore, it is crucial to find a good balance to run simulations effectively. By default, the simulation mesh is automatically generated non-uniformly according to the specified mesh accuracy level, and the FDTD solver provide 8 level of mesh accuracy. The target is 6 mesh cells per wavelength (PW) for a mesh accuracy of 1, 10 (PW) for a mesh accuracy of 2, etc [90]. The mesh size at certain points of the structure for a broadband wavelength range is defined by the smallest operation wavelength and the refractive index of the materials. For example, the

mesh size with mesh accuracy level of 2 in gold will be λ_0/n_{gold} divided by 10 where λ_0 refer to the smallest wavelength in vacuum. This means that the mesh size is inversely proportional to the refractive index, with higher index materials resulting in smaller mesh size. Additionally, if the wavelength range is different, or if the materials refractive index is changed, this will potentially affect the mesh size. Obviously finer meshes provide more reliable results, however, using coarse mesh such as mesh accuracy of 1 or 2 is recommended to begin with.

In some cases, when a certain area needs alternative mesh size, the mesh override functions allows a small volume of space to be defined with a new mesh. The mesh size defined in mesh override regions will be the absolute global mesh size in this specified area, even if it is a larger mesh size than the automatically generated mesh. This can help save simulation time with larger defined mesh, or can force the mesh to be smaller where the structure is a more complex shape. Mesh size can be viewed in Figure 3.4 (b) and (c) in the layout of small orange grid.

Boundary conditions which define the boundary of each side of simulation region are another crucial aspect in any simulation. The FDTD solver provide boundary options including perfectly matched layers (PML), metal, periodic, symmetric, Bloch and perfectly matched (PMC) boundary conditions. In the modelling of the nano-rod based metasurface, PML and periodic boundary are applied as shown in Figure 3.4 (b) and (c).

PML boundary conditions are the most common option and are applied on at least some boundaries in most simulations. Notably, in any reflection, the outgoing wave can potentially re-interfere with the source, resulting in incorrect power normalisation or scattering fields and therefore reducing the accuracy of results. PML boundaries in the FDTD solver simulates an absorbing material which absorbs incident light with zero reflections. The FDTD solver provide options including different PML types and customized PML thickness, allowing reflections to be minimized without increasing simulation time. For metasurface simulations with normal incidence, PML boundaries will be applied on two sides along the transmission axis in order to absorb outgoing waves. In this case, the default PML setting with appropriate thickness is sufficient. Another important boundary condition for the simulation of metasurface is the periodic boundary condition. In the case of simulating a periodic system, periodic boundaries allow entire system to be simulated using only one unit cell, which saves an enormous amount of time. For the metasurfaces discussed in this thesis, the simulation region is set to be the same size as a unit cell, with the four sides of the region set as periodic boundaries. In the simulation, both the physical structure and the optical response are periodic. The boundary simple copy the EM fields that occur at one side of the simulation and inject them at the other side. It is worth to mention that for the case of periodic structure illuminated by a plane wave at oblique incidence, Bloch boundary conditions will be the option as the EM field is not periodic anymore. For system that are both periodic and symmetric in physical structure and EM field, symmetric boundary conditions can be used, which

significantly reduced the simulation time by simulating only one half of the unit cell.

3.4.4 Normalisation

The frequency domain field monitors in the FDTD record the electric and magnetic field as a function of time, and then convert the simulated time domain into frequency domain using the Fourier transform:

$$\vec{E}_{sim}(\omega) = \int \exp(i\omega t)\vec{E}(t)dt \tag{3.21}$$

where $\vec{E}_{sim}(\omega)$ is the electric field returned by monitor, and $\vec{E}(t)$ is the time domain field information recorded by monitors.

Normalised simulation results are much more useful than the impulse response of the system because it is completely independent of the magnitude of the excitation source. Continuous wave normalisation (CWnorm) is a default state to return normalised results as a function of frequency in most applications. In the CWnorm state, the field are normalised by the Fourier transform of the source pulse, thereby yielding the impulse response of the system and given the optical response only cause by simulated objects [91]:

$$\vec{E}_{nor}(\omega) = \frac{1}{s(\omega)}\int \exp(i\omega t)\vec{E}(t)dt = \frac{\vec{E}_{sim}(\omega)}{s(\omega)} \tag{3.22}$$

where $s(\omega)$ is the frequency signal of the source:

$$s(\omega) = \int \exp(i\omega t)s(t)dt \tag{3.23}$$

3.5 Analysis of simulation results

3.5.1 Visualisation of results

In FDTD, with the setting of CWnorm state, the frequency domain field profile monitor collecting data in frequency domain is a response of the source injecting a continuous wave at a given frequency with amplitude of 1. This returns the normalised fields that are completely independent of source at a given frequency across the spatial region. A result manager 'Visualizer' is provided to visualise, analysis and output simulation results. This can return the profile of electric, magnetic and Poynting vector at a specific position and frequency in the form of a colour map. Example of 2D electric profile in xy plane 6nm above nanorod-based metasurface at 6μm is shown in Figure 3.5. The x and y axis of the colormap provides dimensions of unit cell and the values of electric intensity are indicated using colorbar. This result provides quantitative information of electric field enhancement by metasurface.

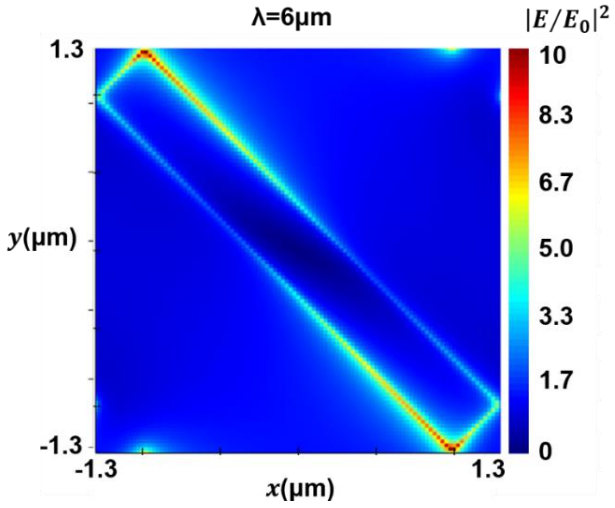

Figure 3.5 The electric field intensity at 6μm on xy plane 5nm above nanorod-based metasurface.

This tool can also plot raw data of transmission and reflection as a function of frequency.

3.5.2 Analysis group and script editor

In the simple cases, the monitors collect the data of near field profile and far field projection which are enough to analyse the structure. However, in some cases, the analysis group with its scripting function is a useful tool that can provide additional complicated results. For example, instead of returning the transmission and reflection profile of the given system, the analysis group can be used to provide the far field projection including polarization information when the simulated structures may rotate the polarization sates. In addition to the electric and magnetic field, the analysis group can also calculate results such as the charge distribution and current density.

The process of an entire simulation start from adding structures, setting up their properties, running simulations and analysis of the results. This process can be done manually as discussed above by clicking the relevant menus and specify values for each variables. The FDTD solver also has a script editor window which provide scripting function allow user to automate all the setting tasks by scripting. This significantly reduces the amount of time required for multiple simulations, such as the optimization of structures by parameter sweeping and convergence testing (this will be discussed in the next section). It also allows simulations to be compared by plotting results together into one graph, and it is also a useful tool to analysis complicated results from the analysis group. For instance, it can break

down S-parameter according to polarization state, and only plot the S-parameter with specific polarization along with phase information scripting also allows simulation results to be outputted in different formats for further analysis.

3.6 Optimization simulation

3.6.1 Parameter sweep

One of the most common tasks in simulation is to find the suitable value for variables in order to obtain an optimised design. Running simulations step by step with varying values of each parameter is extremely time consuming and uses a large amount of memory The parameter sweep utility is a built-in algorithm to study the sensitivity of the design performance to certain parameters. This function allows the automation of a series of simulations with a set of varying variables to find the optimum value. If there is more than one parameter to optimise, the optimization utility provides an advanced optimization algorithm which can efficiently run a large number of simulation to optimize a design.

3.6.2 Convergence testing

FDTD numerical simulations can never provide absolutely precise results due to the discretization of space and time, the artificial PML absorbing boundaries, and errors arising from the material dispersions.

For a limited size of mesh, the dispersion relation of FDTD can be calculated precisely for a given mesh size. However, the discretization of the simulation

region in space make it impossible to resolve objects into arbitrary resolution. This can introduce errors as a curved, rotated or sharp object will not be resolved exactly. There can also be some monitor interpolation errors that are introduced when field components are interpolated from locations where they are calculated on the Yee cell. The discrete mesh can also cause discrepancy between the simulated light wave on the mesh and in practical space. In principle, due to the discrete mesh, all of the discussed errors can be reduced by refining the spatial and temporal mesh size.

When PML boundaries are applied in simulation, there can be errors introduced when the boundaries are too close to objects. When the simulated structure generates non-negligible evanescent fields, there can be coupling between the evanescent fields comes from structures and PML boundaries. This can reduce the quality factor of a resonance or shift the frequency of a resonance. PML can also generate artificial reflections which can re-interfere with scattering field or the source, causing incorrect normalisation. This source of error can be reduced by placing the PML boundary farther away from objects, and increasing the thickness of PML materials.

As discussed in the section on materials (3.4.1), the dispersive materials fit model is likely to be the dominant source of error in the simulation since FDTD will re-fit the materials properties into a model that can be solved by the FDTD algorithms. This can be reduced by modifying the material fitting parameters in order to obtain a good fit however, there will always error in the fit.

Convergence testing is used as the final step to investigate the source of errors in simulations, so that the design can be improved further to meet the desired level of accuracy of the simulation results. It is a procedure similar to the parameter sweep and it is used to find the optimum setting by varying the value of variables. However, to obtain more accurate results often involves increased simulation time and memory. While running convergence tests, it is important to consider the acceptable level of error so that the simulation can finish in a reasonable amount of time. For example, it is not necessary to refine the size of object down to a precision of 1nm when the manufacturing process can only achieve the accuracy of 10nm.

After narrowing down the range of variables using the parameter sweep, the sources of error only cause very small effects on the simulation results, and it is difficult to identify the 'correct' answer among all the similar results. Therefore, it is necessary to quantify the level of convergence. At each step of a parameter sweep, the difference with the results of the previous step is defined as [92]:

$$\Delta\sigma(i) = \sqrt{\frac{\int(\sigma_i - \sigma_{i-1})^2 d\lambda}{\int(\sigma_i)^2 d\lambda}} \tag{3.24}$$

where i refers to each sweep step for each parameter, $\Delta\sigma(i)$ is the corresponding simulation results. Ideally, when this quantity becomes close to 0, it means the parameter has finds its optimum value. However, if $\Delta\sigma(i)$ reaches a constant value, it means that the error is being dominated by another parameter, although the current parameter still has an effect.

In order to quantify the absolute error, it is useful to consider the difference between the current parameter σ_i and that 'correct' answer σ_N at sweep step of N. This quantity can be defines as [92]:

$$\Delta\sigma_N(i) = \sqrt{\frac{\int(\sigma_i - \sigma_N)^2 d\lambda}{\int(\sigma_i)^2 d\lambda}} \tag{3.25}$$

This will provide a good estimate of the absolute error when i is away from N.

A set of convergence tests have been conducted to the structure studied in this thesis. The simulations were undertaken with a single unit cell modelled with periodic boundary conditions in the x- and y-directions over a period of 2.6μm. The structure of a unit cell consists of a 50nm thick aluminum ground plane at the bottom, followed by a 600nm thick silicon dioxide layer, with a 3.2μm by 400nm gold rod resonator oriented at 45 degrees x axis on the top. Values of gold and aluminum conductivity were taken as $4.5 \times 10^7/\Omega m$ and $3.75 \times 10^7/\Omega m$ respectively to be consistent with those used in previously reported mid-infrared studies [88], [89], [93], with the refractive index of silicon dioxide taken from the Lumerical database from Palik [87]. PML absorbing boundary conditions are set along the z direction to absorb incident light with minimal reflections. The excitation is polarized along rod resonators expected to excite two resonances at 3.49μm and 7.9μm in reflectivity spectrum.

In order to test the simulation more efficiently, the convergence test is started from the parameters that can be swept on a coarse mesh quickly, such as PML distance and layers, leaving the tests that take longest, like finer mesh size to the

end. To begin with, the minimum PML layer was set to 16 cells. The mesh accuracy is set to be level 2. The inner mesh size was set as 50nm in the x and y directions, 25nm in z direction, with the mesh boundary along the interface of metal and silicon dioxide to guarantee the accuracy of simulation results. In the convergence tests, we only need to investigate the reflection of metasurface when the light source is linearly polarized in the direction along the rod, so the polarization angle of incident light is set to be 45 degree.

(1) PML distance

To test the PML distance, to reduce the PML reflectivity, a parameter sweep function was used to first perform 10 steps which will vary the simulation span from 10 to 100 microns. The distance between the source and PML layer was set to 1/5 of the simulation span, and the source position changes accordingly at each PML distance. In the simulations, the wavelength range is from 3 to 10 microns, and the thickness of metasurface is only 0.7 microns, so the distance from the structure to the PML, which ranges from 4.65μm to 49.65μm, is larger than ¼ of the wavelength. Figure 3.6 shows the results of the convergence test, and it can be seen that the difference between each sweep is constant across the entire sweep. The value of $\Delta\sigma(i)$ and $\Delta\sigma_N(i)$ are relatively small and flat. Therefore increasing the PML distance make no obvious change to the reflection results, indicating that other parameters dominate the errors.

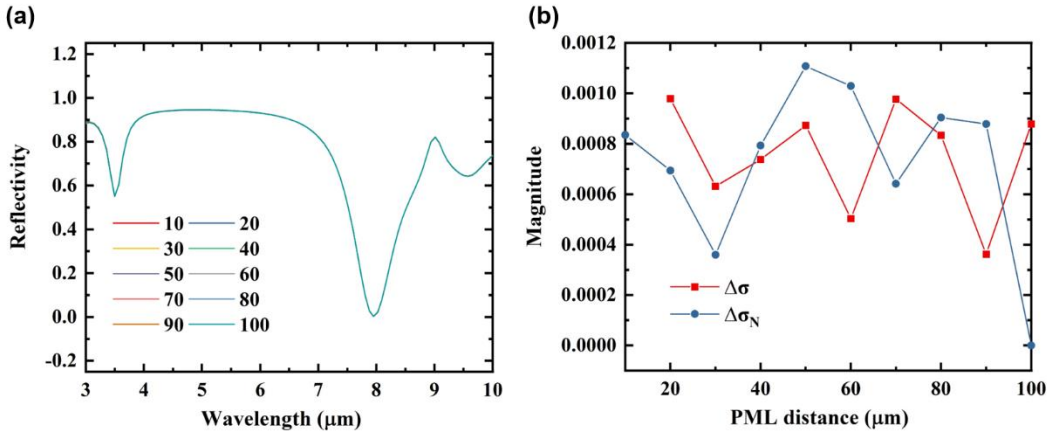

Figure 3.6 Convergence testing result on PML distance. (a) Reflectivity spectrum for various PML distance. (b) Calculated $\Delta\sigma(i)$ and $\Delta\sigma_N(i)$ as a function of various PML distance.

(2) PML layers

In order to test various PML layers, we set the simulation span at 40 microns, source offset at 8μm, the same mesh accuracy settings and inner mesh size as before. In this test, PML layers are swept with 6 points including 4, 8, 16, 32, 64 and 128 layers. The simulated results are shown in Figure 3.7. At the minimum number/thickness of PMLs, the simulated spectrum contains interference fringes due to the reflectivity from the PML boundary. As the number of PML layers increase, the interference fringes due in the simulated reflection, and the value of $\Delta\sigma(i)$ shrink significantly until it reaches a constant value of 32. This is an indication that the error from PML reflection is not dominant. Both $\Delta\sigma(i)$ and $\Delta\sigma_N(i)$ contribute less than 0.1% after 32. For the best results, we can operate our simulation at PML layer of 64 that will be enough to reduce the error from the PML boundary.

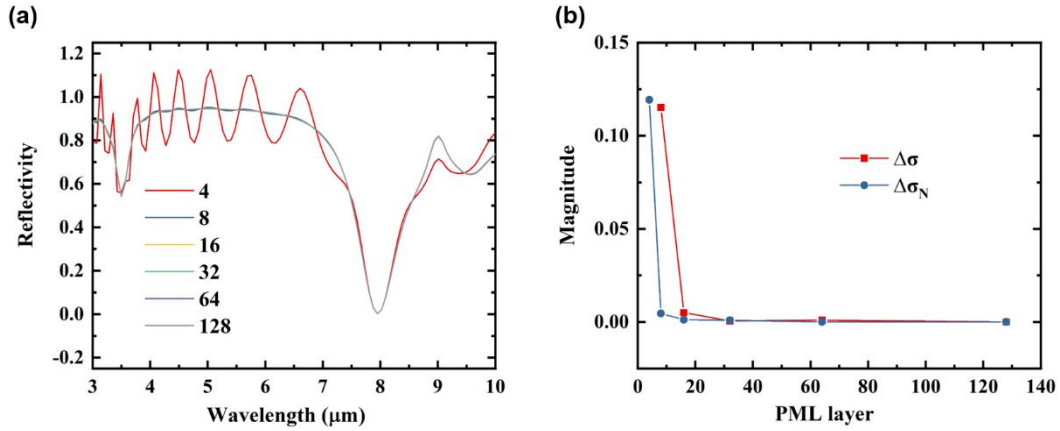

Figure 3.7 Convergence testing result on number of PML layers. (a) Reflectivity spectrum for various PML layers. (b) Calculated $\Delta\sigma(i)$ and $\Delta\sigma_N(i)$ as a function of various PML layers.

(3) Mesh accuracy

After setting the PML layers to the 64, the mesh accuracy level was swept from level 1 to 5, with the resulting simulated reflection, and error, plotted in Figure 3.8 (a) and (b) respectively. From these results, the mesh accuracy level introduces an error up to 0.8% at level of 2. As expected, higher levels of mesh accuracy reduce the errors, and both $\Delta\sigma(i)$ and $\Delta\sigma_N(i)$ drop significantly and below 0.1% at level 4. Based on the results, a mesh accuracy of level 4 was chosen, corresponding to a target mesh size of 18 points per wavelength, was chosen for the simulations described in this thesis

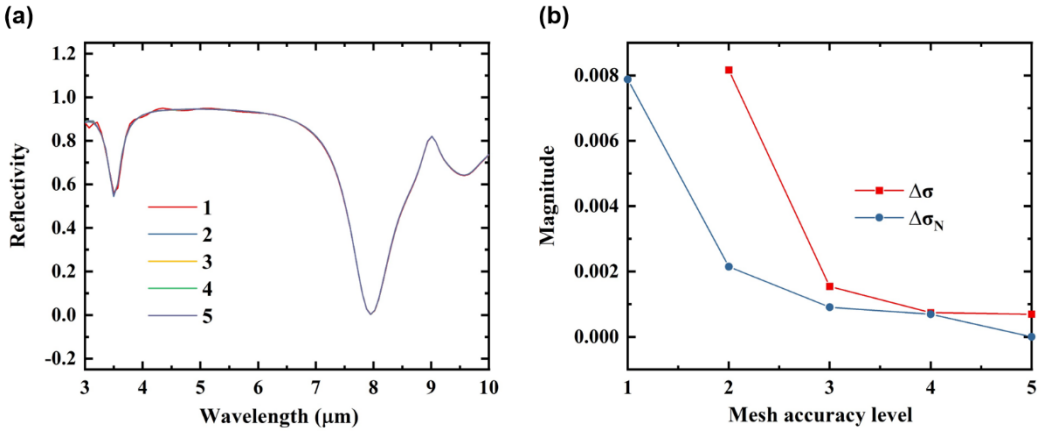

Figure 3.8 Convergence testing result on Mesh accuracy. (a) Reflectivity spectrum for various mesh accuracy level. (b) Calculated $\Delta\sigma(i)$ and $\Delta\sigma_N(i)$ as a function of various mesh accuracy level.

(4) Inner mesh dx and dy

Based on analysis from the testing described above. The mesh accuracy was set at level 4, PML layer of 64 and PML span of 40μm. The inner mesh of dx and dy were then swept into 13 points between 0.01μm and 0.26μm. The value of each mesh resolution were selected to be: 0.01μm, 0.02μm, 0.025μm, 0.04μm, 0.05μm, 0.065μm, 0.1μm, 0.2μm and 0.26μm so that the mesh boundary can line along the edge of unit cell with size 2.6μm*2.6μm. The effect of the inner mesh on the simulated reflection spectrum, and associated errors, are plotted in Figure 3.9, which clearly show that the inner mesh size has considerable influence on the both the frequency and strength of the resonances. The coarsest mesh sizes, such as 0.1μm, 0.2μm and 0.26μm, introduces error up to 7%. As the mesh size is decreased to values below 0.065μm, the resonances in the reflection spectrum have negligible changes between steps. At dx= dy =0.05μm, the absolute error is below approximately 1%, and continues to reduce as the mesh size is

decreased. Considering the balance between simulation efficiency and results accuracy, a mesh of dx=dy=0.025μm was chosen, so that typical simulations took approximately 1 hour.

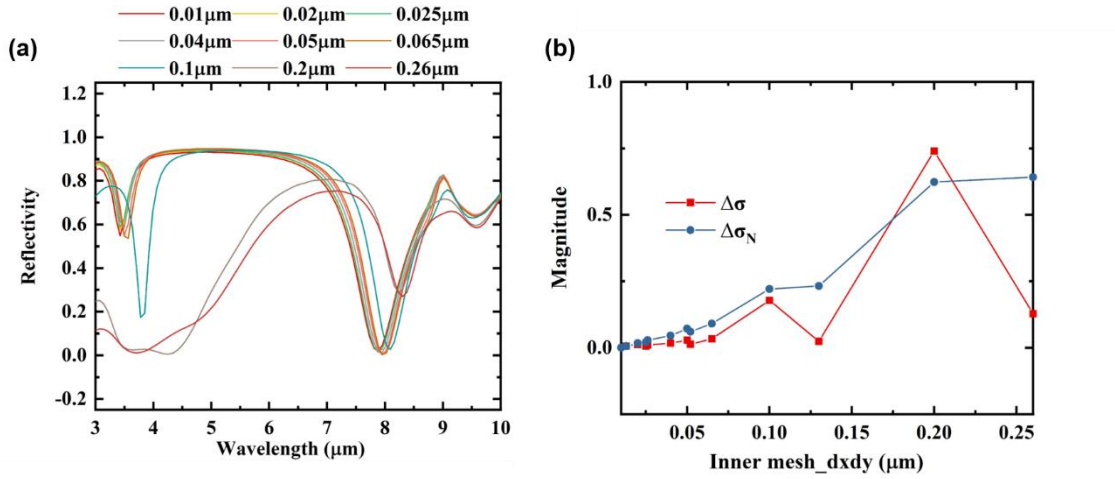

Figure 3.9 Convergence testing result on inner mesh of dx and dy. (a) Reflectivity spectrum for various inner mesh size of dx and dy. (b) Calculated $\Delta\sigma(i)$ and $\Delta\sigma_N(i)$ as a function of various inner mesh size of dx and dy.

(5) Inner mesh dz

The last parameters to be analysed was the inner mesh size dz, which was found to be the dominant source of error. In order to ensure that all of the mesh is lined at the interface of different materials, dz was swept with 5 points: 0.0025μm, 0.005μm, 0.01μm, 0.0125μm and 0.025μm. As shown in Figure 3.10, the parameter dz has a small effect on the resonance at 3.4μm in the simulated reflection spectrum. At dz=0.025μm, the absolute error $\Delta\sigma_N(i)$ shows a maximum value at 6%. For dz smaller than 0.025μm, the error starts to drop and then $\Delta\sigma(i)$ becomes essentially constant between 1% and 2%. This indicates that the error from mesh size dx and dy starts to play an important role. Comparing with the

values of $\Delta\sigma(i)$ from the other sources of error, $\Delta\sigma(i)$ of dz is still the largest. However, the level of error is acceptable as it still allows accurate values of the resonance frequency to be obtained with reasonable simulation time.

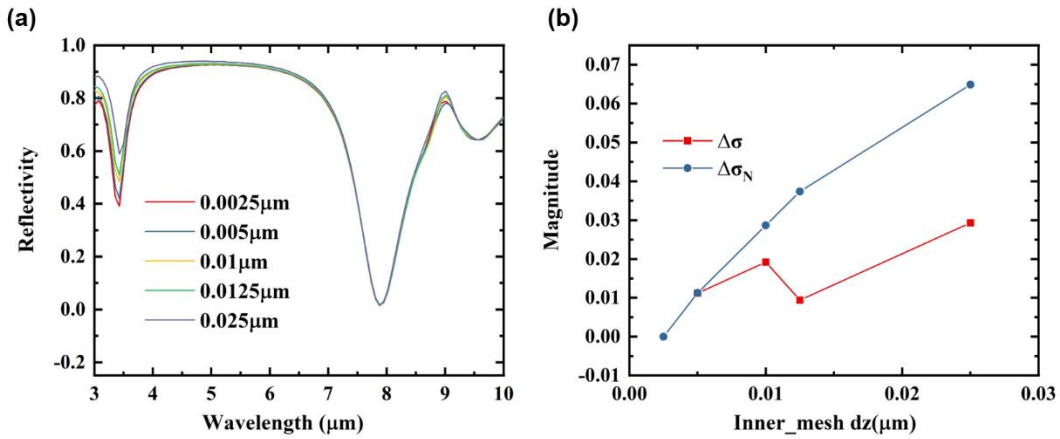

Figure 3.10 Convergence testing result on inner mesh of dz. (a) Reflectivity spectrum for various inner mesh size of dz. (b) Calculated $\Delta\sigma(i)$ and $\Delta\sigma_N(i)$ as a function of various inner mesh size of dz.

In summary, after conducting a set of convergence tests, the structure studied in this thesis is simulated with PML span of 40μm and 64 layers. The mesh accuracy is set to level of 4 and the inner mesh size is set to be $dx = dy$=0.025μm, dz=0.005μm.

3.7 Summary

This chapter summarised the principles behind the finite difference time domain (FDTD method) used in this work. The chapter begun by introducing Maxwell's equations that govern the behaviour of electromagnetic wave. Next we introduced the central difference approximations upon which the FDTD algorithm is built. We then walked through the setup of the FDTD including building the

structure, selecting materials, the simulation region and mesh setting. This followed by post simulation actions which cover tools that offer visualisation of results and post-processing of data. Finally, the workflow of simulation optimization including parameter sweep and convergence testing was discussed.

Once an optimised metasurface design was obtained, metasurface samples were fabricated to be characterised experimentally. In the next chapter, we will introduce the top-down nanostructure fabrication method used, based on electron beam lithography, to realise samples.

4 Sample fabrication and characterization

4.1 Introduction

The minimum feature of metasurfaces can be on the order of ten nanometres with subwavelength thickness. In the metasurface studied in this thesis the minimum geometric parameter is the width of rod; 40nm. Therefore a reliable fabrication process is required to guarantee the precise scale of the geometric parameters of the metasurface. The fabrication of the metasurface employed a top-down fabrication technique in which electron beam lithography and thermal evaporation were used for nano-patterning and metal deposition.

This chapter is divided into two big sections that introduce the sample fabrication process and characterization. The first section describes the details of the sample fabrication process. It start off by introducing cleaning of the substrate wafer to prepare for electron beam lithography. Then follows by the summary of the lithography etching process, and includes a discussion of important factors including: beam current size, exposure dose, datum level and development process, that impact the quality of sample. The next is an introduction of thermal evaporation and lift off process. Finally, an example set of data setting and image for the fabricated nanorod-based metasurface sample is provided.

The next section focusses on the characterisation of the metasurface, with the first section an introduction to metrology including optical microscope and scanning electron microscope, and the section an introduction to infrared

spectroscopy. Optical microscopy serves as an inspection tool during the fabrication process to assess the quality of the pattern, while scanning electron microscopy was used to precisely verify the geometric parameters of a fabricated sample. The section starts with an introduction to the key part of the sample characterisation, Fourier Transform Infrared spectroscopy (FTIR), and includes details of the particular instrument used, a Brucker Vertex 80v FTIR spectrometer, and its operation principle. The measurement setups used to obtain the transmission and reflection spectra, and polarisation characterisation, are descried.

4.2 Fabrication process

4.2.1 Cleaning

Metasurfaces were fabricated on silicon based wafers (contain 600nm SiO_2 on top of 100nm aluminium and silicon) purchased from ePAK, which were first sawn into 1cm x 1cm chips. The fabrication started by cleaning the sample using ultra-sonication in acetone for 20 minutes, followed by 10 minutes ultra-sonication in isopropyl alcohol (IPA) to remove any chemical impurities or particles. Acetone dissolves grease, wax, or any organic particles, and can therefore be used to remove dust and other contamination, but also leaves residues. Therefore, subsequent isopropanol soaking is essential steps to removes these residues. Cleaning with IPA allows the surface to dry without spotting, but blowinging the surface with compressed nitrogen gas is better for providing a completely moisture-free environment for substrates. A final baking out step at the end of

cleaning procedure, 200°C for 20 minutes on a hot-plate, is used for the desorption of water and other solvent molecules.

4.2.2 Electron beam lithography

Derived from the early scanning electron microscopes, electron beam lithography is a direct writing lithographic process of scanning a focused electron beam on an electron-sensitive film to deposit energy with the desired pattern. The electron sensitive film is called a resist, and changes its solubility under exposure from the electron beam. The most common electron-sensitive film in use is polymethyl methacrylate (PMMA) as a high resolution positive e-beam resist, and hydrogen silsesquioxane (HSQ) as a negative resist. As depicted schematically in Figure 4.1, a positive resist becomes easily dissolved by developer after electron beam exposure, while a negative resist works in the opposite way to enable selective removal of the non-exposure area.

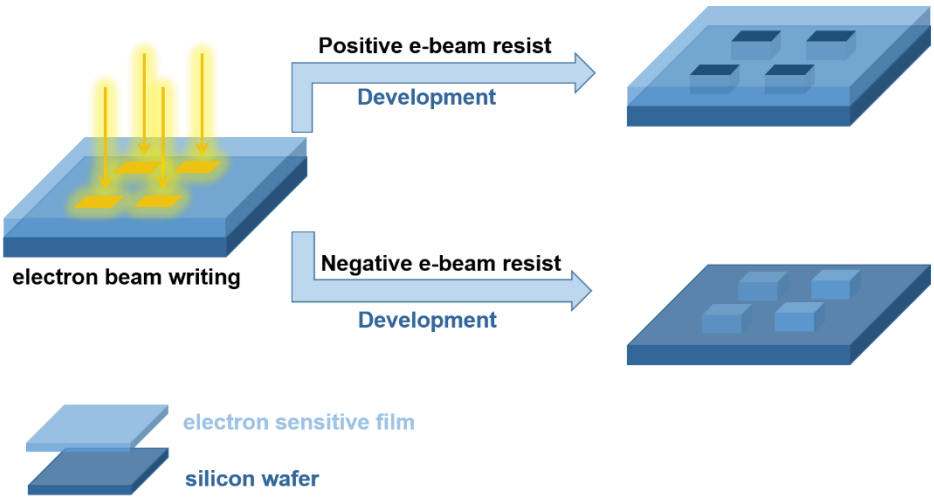

Figure 4.1 Schematic of development process for positive and negative resist.

The metasurface described in this thesis were fabricated using a NanoBeam NB4 el. In the lithography process, there are various parameters directly relevant to sample quality that need to be optimised: beam current size, exposure dose, datum level and development process.

Smaller current beam diameter, with lower throughput, always results in a better resolution. However, the resolution is not only determined by the current beam diameter, but is also influenced by a scattering effect from electrons also known as proximity effect [94], which expands the interaction volume in the resist thus broadening the diameter of the irradiated area. The e-beam dose, which determines the number of electrons per unit area of exposure, is a critical exposure variable for proximity effect correction. The interaction of the electron beam-resist and electron beam-substrate means that that the required exposure dose depends on the resist materials, thickness etc., and has to be determined experimentally. The first lithography run was always therefore a set of dose tests, where different doses were applied to each pixel, to find the exact dose required for a particular pattern

A set of built in calibration packages are available in the e-beam system, including with reference to the datum level. The datum level is an important factor in ensuring that the beam is focussed on the surface of the sample, allowing for different sample thicknesses. The system has 11 datum levels, with a height difference of 110μm per step, to accommodate different sample thicknesses. Datum 1 is the highest level, which is suitable for thick substrates, while datum 11 is the lowest level for thinner substrate.

The development process, which is used to dissolve the exposure area of a positive resist, is another crucial process that has to be controlled precisely so that the exposured area can be dissolved completely. The pattern fidelity is affected by parameters such as developer concentration and developing time.

In the fabrication process for the nanorod-based metasurface investigated in this thesis, 4% single layer polymethyl methacrylate formulated with 950,000 molecular weight resin in sanisole was used as a positive resist. The resist was spin-coated, at a speed of 4000rpm, to form an evenly distributed thin layer of 400nm thick resist over the sample. The coated sample was exposed using the electron beam system to precisely pattern a 77x77 array of 3.2μmx0.4μm rods, in turn these arrays were written on a 40x40 grid, where each grid square consisted of one 77 x 77 array . Once the writing is completed, the irradiated area was dissolved in developer, consisting of a compound solution of 4methylpentan-2-one, methyl ethyl ketone and IPA in a ratio of 5:1:15, for 30 seconds. The sample was then rinsed in IPA, and then dried using compressed nitrogen gas. The developed patterns was inspected under an optical microscope, to check for errors, before the next step (metallisation) was undertaken.

4.2.3 Metallisation

After the exposure and development process, the resist layer can be used as a template to transfer the design into a metal layer, a process called metallisation. This starts by coating a thin layer of metal all over the sample. Dissolving an unexposed resist using a solvent, will then leaving the deposited metal in the

areas where there was no resist. Thermal evaporation of metals in vacuum is one of the most commonly used methods to deposit a thin film coating on a substrate, where metal are heated until they boil thus developing a vapour that then condenses on the substrate for an even thin layer. An Edwards HHV Auto306 was used for the fabrication of the samples described in this work, with gold used to form the metasurface due to its high conductivity and stability. To aid adhesion of the gold to the substrate, a thin layer of chromium (5nm thick) was first deposited, followed by 50nm of gold.

The lift off process is an important step to remove unwanted metal deposited on the electron resist PMMA in order to obtain the final pattern. After evaporation, a sample will be soaked into acetone for several hours, which will dissolved the unexposed PMMA, so that metal deposited on the PMMA will be lifted off, while metal deposited directly on the substrate will remain. To aid the lift-off, for small gaps of metal on the PMMA, acetone was sometimes gently squirted directly at the gap using a glass pipette, or the sample was placed in an ultrasonic bath for a few seconds. Inspection under an optical microscope was used to check that the PMMA has been dissolved entirely during the lift off process, before rinsing the sample in IPA and blowing dry with compress nitrogen gas to complete the fabrication process.

The schematic process flow for the nanorod-based metasurface investigated in this thesis is shown in Figure 4.2.

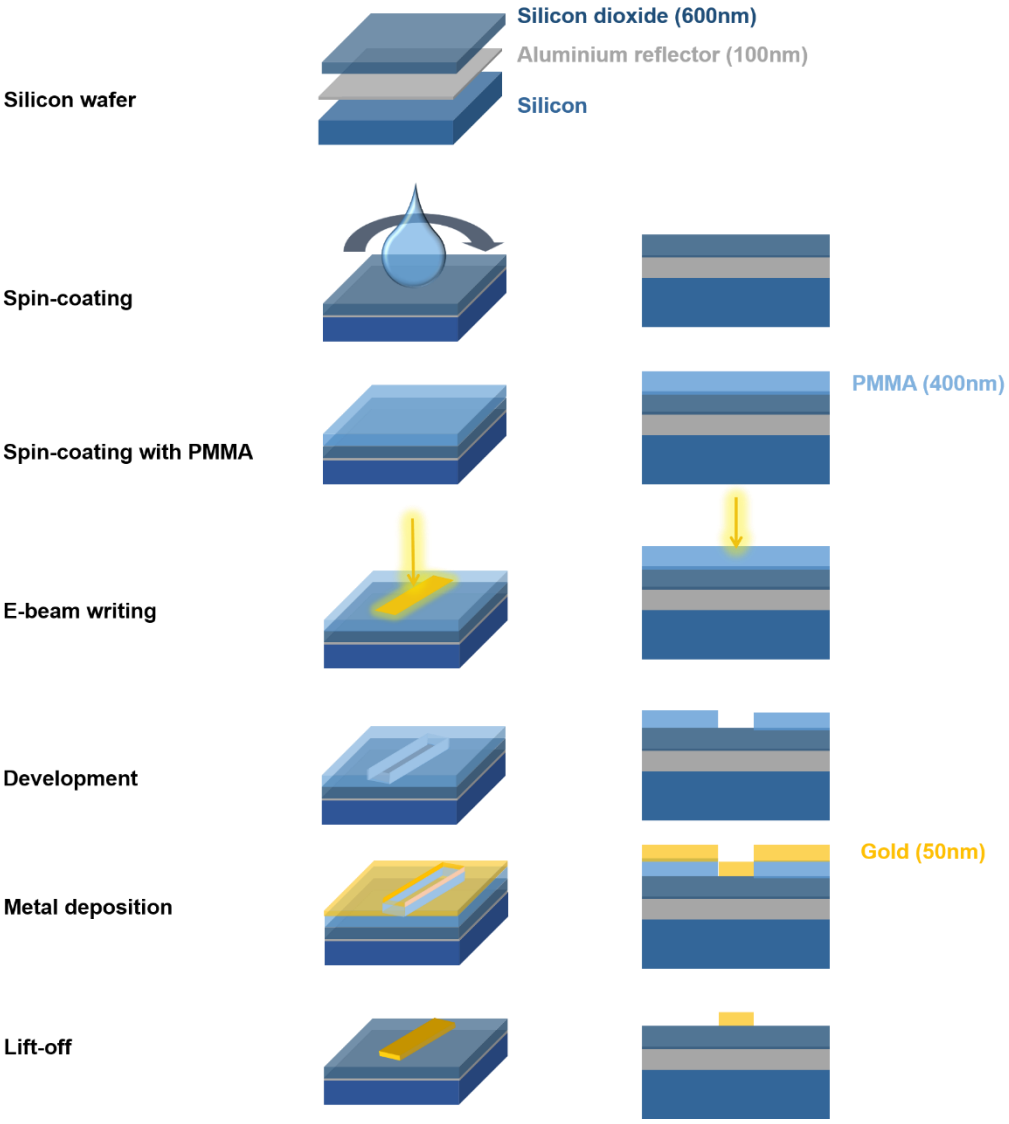

Figure 4.2 Workflow for fabrication of nanorod-based metasurface on silicon wafer

4.2.4 Fabricated sample

Figure 4.3 shows the fabricated metasurface on Natural Science department sticker. Figure in magnifier displays the image under Scanning electron microscope with 6500x magnification.

*Figure 4.3 Images of the nanorod-based metasurface studied in this thesis. 1cm*1cm sample on Natural Sciences badge. Figure in magnifier is SEM image.*

4.3 Metasurface characterization

4.3.1 Optical microscope

A Nikon LV150 upright optical microscope equipped with 5x, 10x, 20x, 50x and 100x bright field objective lenses was used in the fabrication process to inspect sample patterns after e-beam lithography or the lift-off process. With the maximum magnification provided by 100x lens, it is feasible to check 3.2μm x0.4μm rod resonator. Figure 4.4 shows an optical microscope image of a

fabricated metasurface after the development and lift-off processes under optical microscope under 100x magnification. It is clear to see that the structure was patterned with complete and equal unit cells without any unexpected connection. Therefore, optical microscope can be used for inspection to predict errors in fabrication and save time.

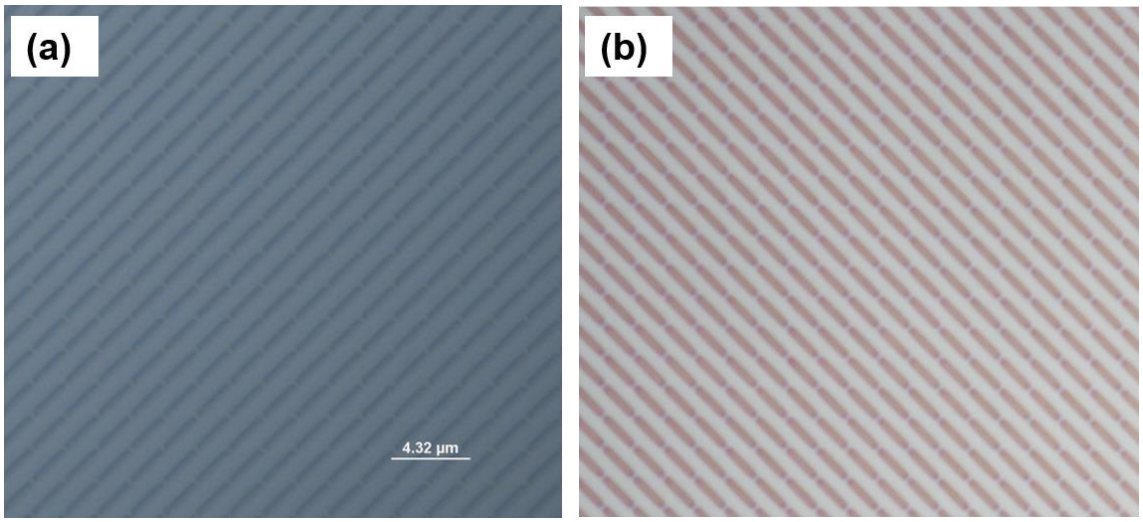

Figure 4.4 Images of the nanorod-based metasurface studied in this thesis under optical microscope. (a) Nanorod-based metasurface after development process. (b) Nanorod-based metasurface after lift-off process.

4.3.2 Scanning electron microscope (SEM)

Due to the fact that the smallest size of the metasurface features are in nanoscales, final inspection of fabricated metasurface patterns was conducted by scanning electron microscope (SEM) to precisely measure the geometric parameters of the resonator structure.

SEM is a type of microscope using electron instead of visible light. The wavelength of visible light limits the resolution of images. By using a beam of

electron with much shorter wavelength, SEM can overcome the limitation of optical microscope for higher resolution imaging purpose. Some electron microscope techniques employ resolution of 0.2 nanometres which is more than 1000 times better than light microscope allowing researchers to study the surface topography and composition of the sample.

Figure 4.5 shows the images of the fabricated nanorod-based metasurface under optical microscope and SEM (TESCAN VEGA3). Although the image provided by optical microscope is with the maximum magnification of 100x, the resolution is not high enough to inspect individual resonator shapes and their spacing, whereas the use of SEM enables much better quality image with higher resolution allowing to check the outline of shape and measure the geometric parameters precisely.

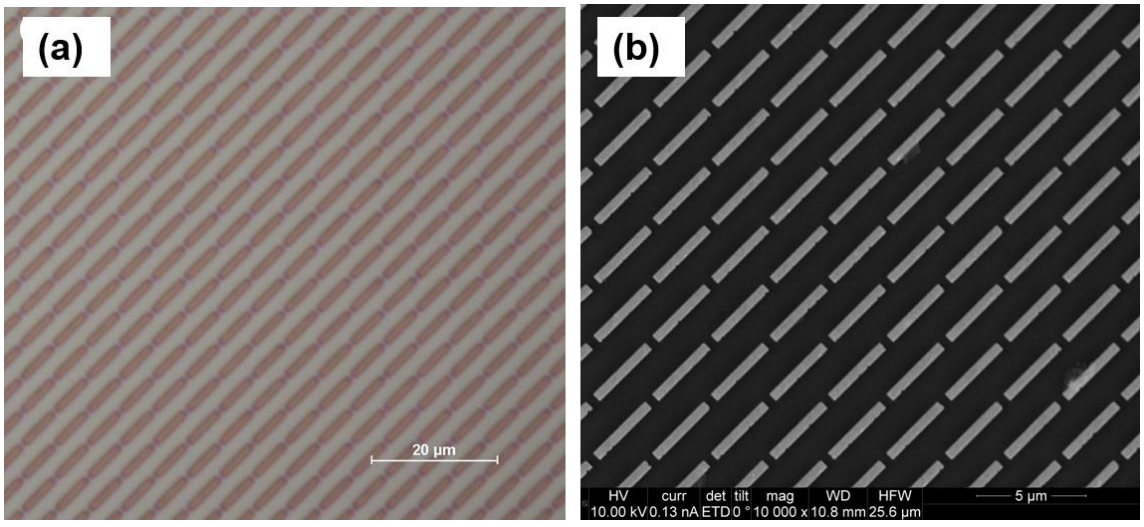

Figure 4.5 Images of the nanorod-based metasurface. (a) Image taken under optical microscope with 100X magnification. (b) Image taken under SEM.

4.3.3 FTIR

Fourier-transform infrared spectroscopy (FTIR) is an analytical technique used to characterise the metasurface, and their interaction with chiral molecules, studied in this thesis. FTIR spectroscopy is often used to identify and characterise the chemical composition of substance based on their interaction with infrared light, where a beam of infrared light in a broadband wavelength range is directed onto a sample. The interaction with sample causing specific bond in the detected small molecules to vibrate at multiple characteristic frequencies leading the multiple absorption dips in the output infrared spectrum. These vibrations are unique to all basic building blocks of life such as lipids, proteins and nucleic acids in this spectral range and allow for the identification of composition and determination of their structures. This significant advantage not only allow to collect high-resolution spectral data over a wide spectral range all at once and saving much time but also provide more accurate results to resolve the chemical bonds mode.

A Brucker Vertex 80V instrument, a high resolution, ultra-fast rapid-scan FTIR, was used in this work. Figure 4.6 (a) depicted the internal components and Figure 4.6 (b) shows the schematic optical beam path inside system. With standard air-cooled MIR source, convergent polychromatic infrared light is emitted from a globar, which is a U-shaped piece of silicon carbide. The emitted infrared light is focussed at a point, then passes through an aperture wheel allowing adjustment of beam size in the range 8mm to 0.25mm. After collimation by a parabolic mirror, the infrared beam will travel through a Michelson interferometer, and then is

focussed at the sample position using a parabolic mirror. The output beam is then directed to a liquid nitrogen cooled detector which can measure the intensity of infrared light as a function of time. Finally, the time-domain signal will be Fourier-transformed into a frequency-domain spectrum that represents the intensity of the infrared light as a function of wavelength or wavenumber.

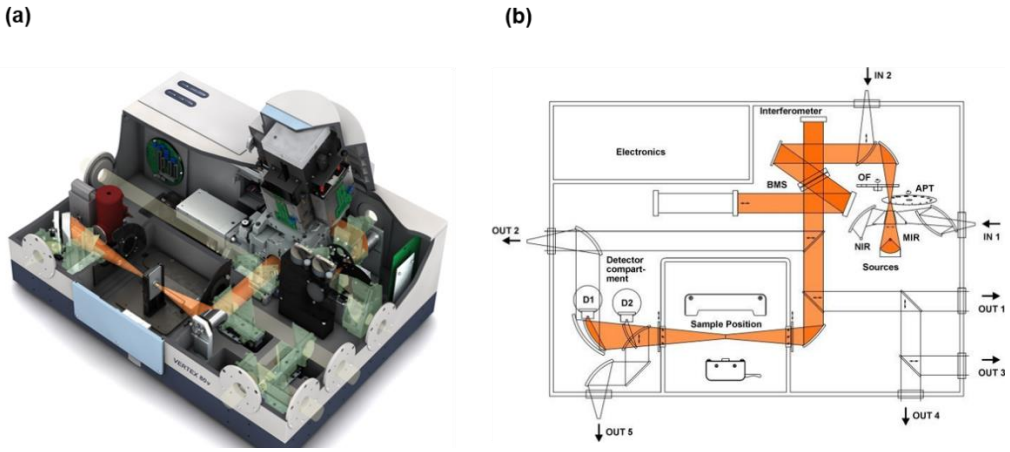

Figure 4.6 Schematic diagram and beam path of Bruker Vertex 80v FTIR spectroscopy (illustration taken from [95]*)*

The Michelson interferometer, consisting of a beam splitter, a stationary mirror and a movable mirror on a precise linear scanner, is a core component in FTIR. The basic setup of this interference system is shown in Figure 4.7 (a). The beam splitter is designed to split the incident beam into two (shown in blue), with one beam directed to a stationary mirror, and the other to a movable mirror. The separated beams will then be reflected by each mirror (the reflected beam are marked as red and yellow and then recombined at the beam splitter, generating an interference wave which is then guided to the sample chamber.

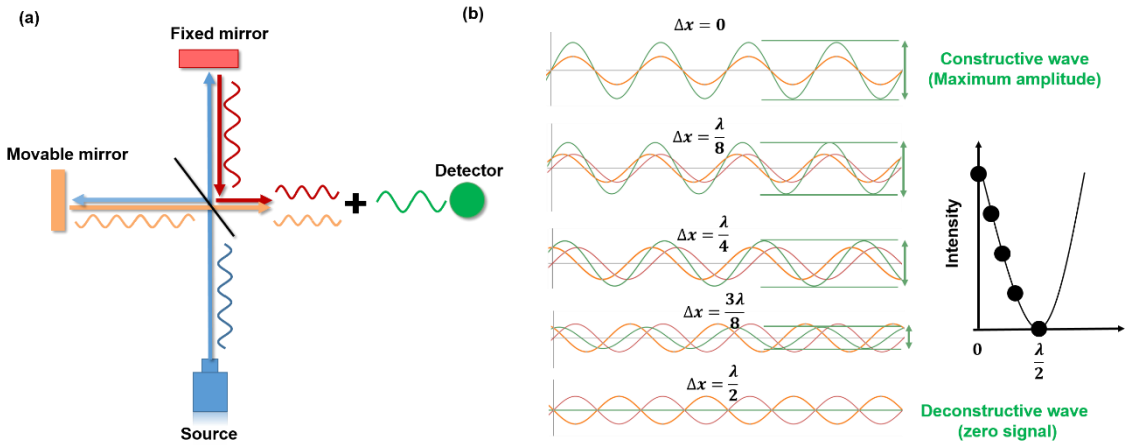

Figure 4.7 (a) Schematic diagram of Michelson interferometer. (b) Two separate beam (marked in red and orange) with the combined signal (marked in green) for five different optical path difference. The figure of right side display amplitude of the combined beam as a function of optical path difference.

The movable mirror is designed to actively control the beam path difference between the separated beams. Figure 4.7 (b) shows how the amplitude of the combined beam (marked in green) changes as the optical beam path difference increases. First case is when the two beams are all in phase ($\Delta x = 0$), constructive interference occurs, in which case the combine beam reach to its maximum amplitude. When the two beams are out of phase ($\Delta x = \frac{\lambda}{2}$), destructive interference occurs, in which case two beams are offset to each other resulting combined beam with zero amplitude. The diagram in Figure 4.7 (b) reveals that the light intensity of the combined beam is a maximum value in the case of constructive interference when the difference in optical beam path is zero ($\Delta x = 0$). As the mirror starts to move, the intensity of combination beam gradually decreases to zero, when the optical beam path difference is $\lambda/2$. The diagram on the right in Figure 4.7 shows the combined wave intensity as a function of optical path difference for a wave with single frequency. As expected, if the mirror keeps moving further away, the combined wave intensity will start to increase again.

The case discussed above is only for a single wavelength, we can plot the equivalent results for various frequencies as shown in Figure 4.8 (a). The initial condition is recorded when waves have zero path difference at which point the combined wave for various frequencies have maximum amplitude. As the mirror moves away from its initial position, the optical path difference start to increase. As a result, the intensity of the light will decrease to zero due to destructive interference with speed corresponding to their frequncies. In FTIR, the sum of complex oscillatory signal with decreasing amplitude as a function of optical path difference is referred as interferogram (depicted in Figure 4.8 (b)). The further the mirror moves, the less the combined signal can be detected until at a point where the light signal will converge to zero when light are out-of-phase completely.

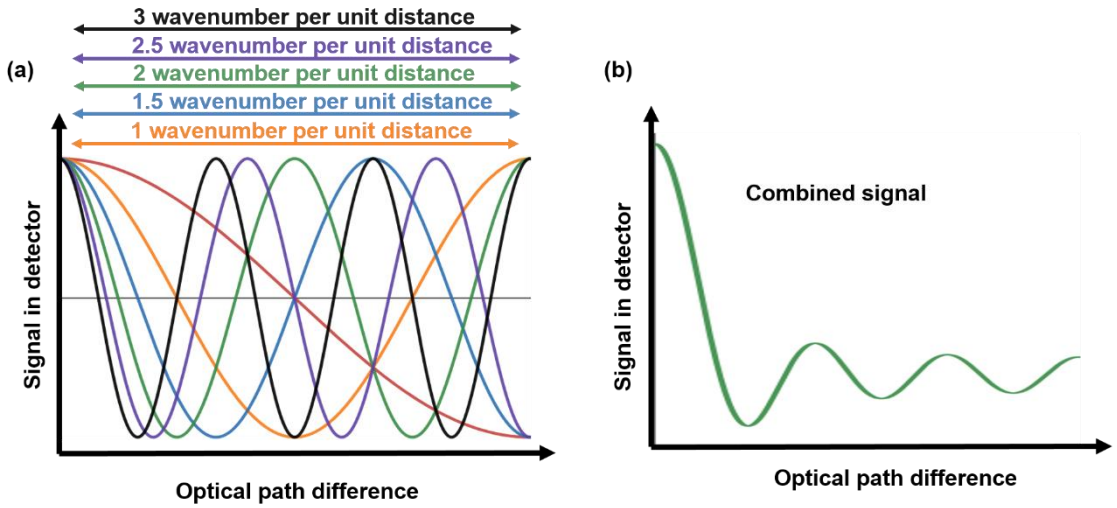

Figure 4.8 (a) Intensity of combined wave as a function of optical path difference for different frequencies. (b) Sum of multiple frequency as a function of optical path difference

In practice, a typical interferogram diagram is shown in Figure 4.9 (a). The x-axis represents the optical path difference in units of centimetre and the y-axis represents the intensity of beam. The interferogram carrying information of

sample's optical properties will be collected and Fourier-transformed into infrared transmission or absorption spectrum with light intensity against wavenumber, which is defined as reciprocal of wavelength in centimetres with unit of cm^{-1}, as shown in Figure 4.9 (b). To better visualise the optical properties of test sample, the spectrum will be normalised by background signal. The final spectrum will be plotted as shown in Figure 4.9 (c).

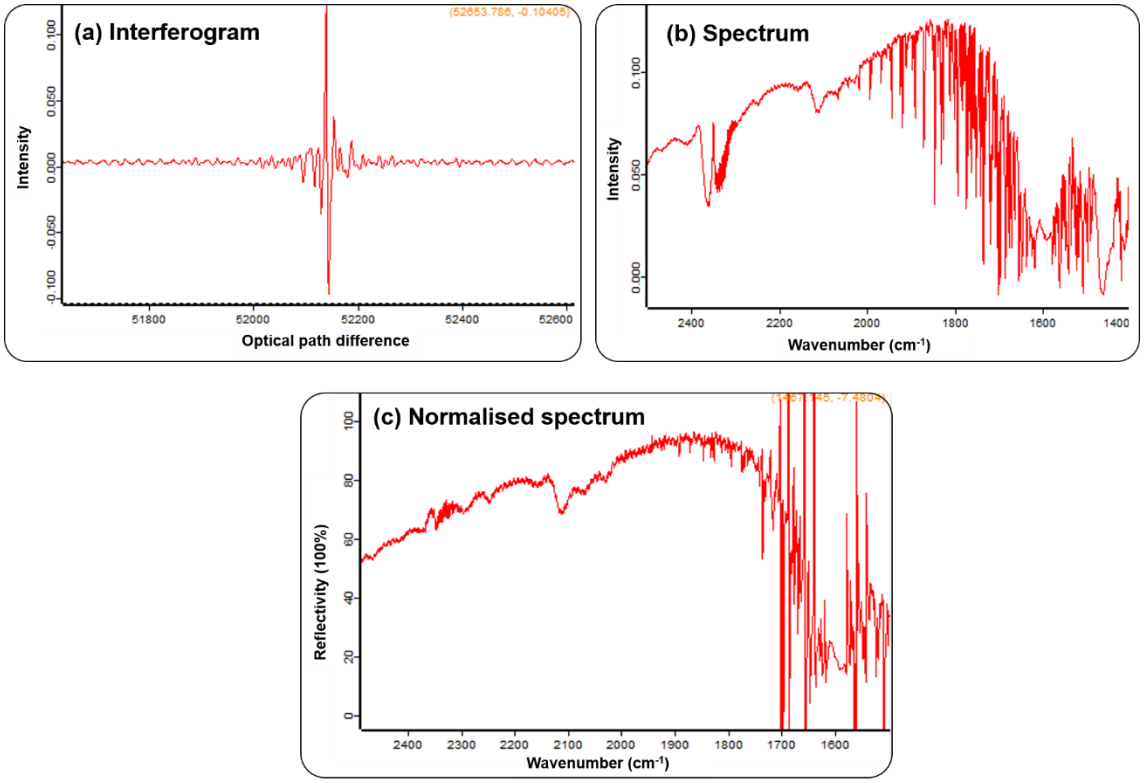

Figure 4.9 The process of collecting spectrum in FTIR spectrometer. (a) The diagram of interferogrm. (b) The transmission spectrum of a device. (c) The normalised spectrum by background signal

In FTIR spectroscopy, the use of the Michelson interferometer offers many significant advantages:

1. Multiplex Advantage

In FTIR, the broadband infrared source is not separated into individual frequencies for measurement. Each scan contains all wavelengths as the mirror moves allowing measurement be completed all at once.

2. The Throughput Advantage

Because of the multiplex advantage, this slit-free system dramatically improves the optical throughput which leads to more light reaching the detector. The higher signal leads to an improved signal-to-noise ratio and improved sensitivity, which allows small details in the sample optical response to be distinguished that would be almost impossible to resolve in a classical dispersive infrared spectroscopy instrument.

3. High Resolution

The maximum achievable resolution in FTIR is determined by number of data points, and this is controlled by sampling rate and maximum optical path difference. The VERTEX 80v instrument is equipped with a Helium-Neon (HeNe) laser that emits red light with a wavelength of 632.8nm. This stable monochromatic light source travels the same path as the infrared beam generating a sinusoidal interferogram and is employed as an internal reference to measure the optical path difference. In addition, this stable laser source is used to trigger a clock which precisely controls the sampling rate when the laser signal pass through zero. This means that the IR discrete signal can be collected at very small wavelength intervals offering high resolution.

The resolution is also determined by the maximum optical path difference, simply because the longer the maximum movement distance the mirror can reach, the more data points can be collected to produce the interferogram, with higher resolution and lower noise. The VERTEX 80v standard configuration provides spectral resolution of better than 0.2 cm^{-1}.

4.3.4 Transmission system

The Brucker VERTEX 80v FTIR instrument comes with a wide range of optional light sources, detectors and beam splitters. These optical components are mounted on dovetail slides allowing them to be easily changed as demand. The diagram in Figure 4.6 only display the most important internal components inside spectrometer. As shown in that diagram, the Bruker Vertex 80v has a built-in well-aligned transmission measurement system. In transmission mode, the standard air-cooled MIR source is employed to emit mid-infrared light, with potassium bromide (KBr) used for the infrared beam splitter as it is transparent across the 8000-350 cm^{-1} spectral region. For detecting signal, a liquid nitrogen cooled cadmium-mercury-telluride (CMT) detector is used for the measurements described in this thesis.

A typical measured transmission spectrum for air (background) is shown as in Figure 4.10. As expected, IR-active atmospheric molecules (CO_2, H_2O) are clearly visible as minima in the measured background spectrum. There is a strong doublet at around 2300 cm^{-1}, which corresponds to absorption from carbon dioxide [96]. The strong absorption features centred around 3800 cm^{-1} and

1600cm^{-1} are due to the absorption of H_2O [97]. The overall shape of the background spectrum reflects the optical response of the overall system, including the output of the source, transmission thought the optical components (e.g. beam-splitter, and response of the detector).

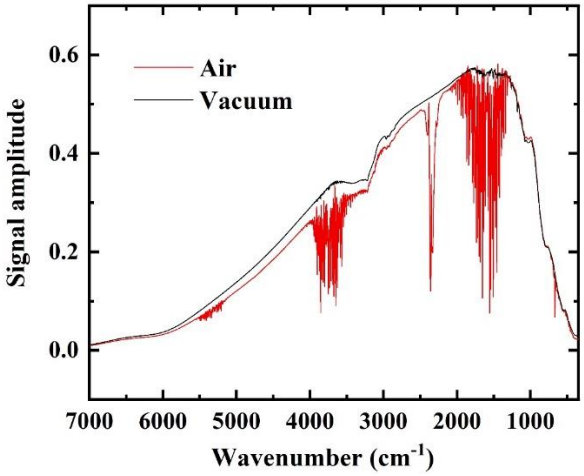

Figure 4.10 The transmission spectrum of background in Air and vacuum.

In the measurement, a reference spectrum of air/vacuum taken as a background before measurements are performed on a sample. Sample spectra are then normalised to the background spectra to remove the effects of atmospheric absorption, and the response of the system, leaving just the response of the sample.

The built-in transmission system was used to characterise the properties of the optical components, such linear polarisers and quarter wave plates that were used in the testing of the metasurfaces in an external reflection system. The linear polarizer used in the experiments was a holographic wire grid polarizer from Thorlabs which operates over the 2-30μm spectral range. It is consists of a

periodic array of metal wire, deposited patterned onto a calcium fluoride substrate, such that only incident light polarised orthogonal to the wires is transmitted. The polarizer can therefore be used to create linearly polarized light from an unpolarised light source. Figure 4.11 (a) the measurement setup where two linear polarizers are positioned one after the other, and Figure 4.11 (b) shows the measured transmission spectrum. The MIR light source in the FTIR is unpolarised, only the fraction of incident light which is polarized orthogonal to polarizer grating (marked as white line in diagram) can travel through. From the measured transmission spectrum in Figure 4.11 (b), It is clear that the transmission of a single polarizer is approximately 0.5, which means half of the incident light is transmitted. When the two polarizers are placed in line, the transmission decreases as one is rotated with respect to the other, thus no signal can be detected across the entire spectrum when the polarizers are orthogonal to each other.

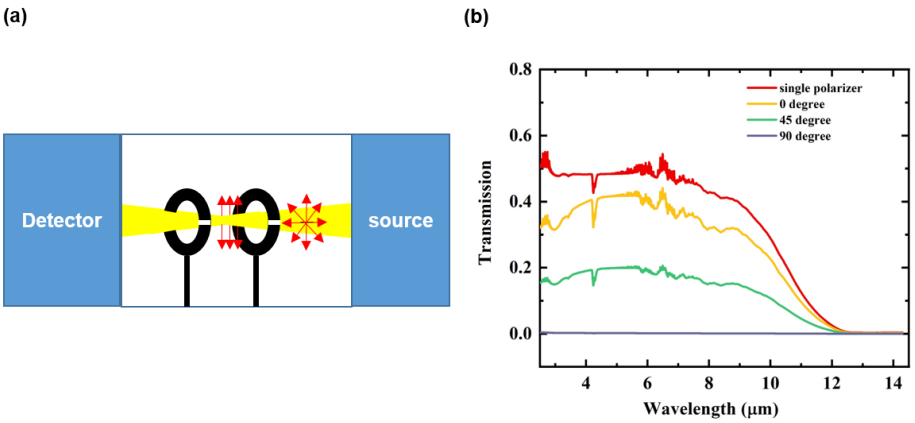

Figure 4.11 (a) The setup to measure transmission of linear polarizer. (b) Transmission spectrum of two aligned linear polarizer

The quarter wave plates used in the measurement were assessed in the same way.

4.3.5 Reflection system

Unlike the built-in transmission system, the reflection system used to characterise metasurfaces was a self-built external setup to conduct linear-to-circular polarization conversion measurements, and is shown schematically in Figure 4.12.

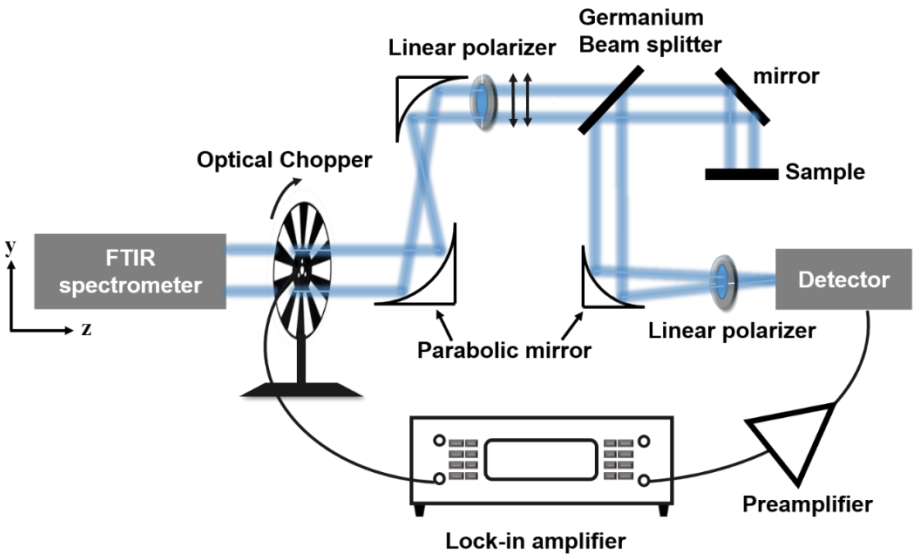

Figure 4.12 Schematic diagram of reflection measurement setup.

In the reflection system, the collimated infrared beam from outport port 4 (details in Figure 4.6) of the FTIR system is first incident on a pair of parabolic mirrors, of different sizes, to reduce the diameter of the collimated beam from 8mm to approximately 1mm. The beam then passed through a 2mm thick germanium beam splitter, which divides the beam into two equal parts, but without effecting its polarization. One beam is then directed into the sample using a gold mirror. The reflected beam from the sample will follow the same beam path back to the beam splitter, and is then guided to a third parabolic mirror which focuses the light into a MCT detector. Parabolic mirrors were chosen for this system as they

have >97% average reflectance over a broadband wavelength range up to 20μm, with no polarization dependence (Figure 4.13), and have focal points which do not depend on wavelength.

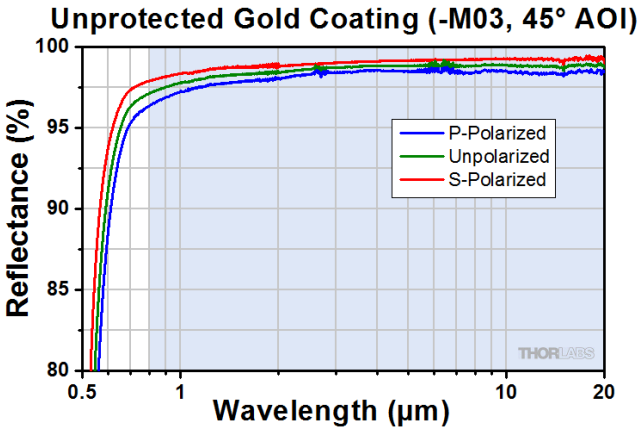

Figure 4.13 The reflectance of unprotected gold parabolic mirror for p-, s- and un-polarized light. (illustration taken from [98]*)*

Unlike the transmission system, where the red HeNe laser could be used to help align to the sample, the germanium beam splitter in the reflection system completely blocks visible light. In order to precisely align the system, a lock-in amplifier with an optical chopper was employed to help improve the signal-to-noise level of the system. This allowed measured reflection signals to be displayed and optimised during the alignment process. For all the experiments conducted in this thesis, the rotation frequency of the chopper was set at 533Hz (to avoid mains pick-up and reduce 1/f noise in the MCT detector). During alignment, the MCT detector was directly connected to the lock-in amplifier output, and the displayed signal maximised through positioning of the detector. The aim of alignment process is to get the as maximum signal as possible by adjusting position of the MCT detector Once the alignment process was finished, the optical

chopper was removed from the beam path, and the MCT detector was re-connected to the FTIR system to conduct reflection measurements.

The reflection system was designed to measure the linear-to-circular polarization conversion performance of metasurface samples, and strict maintenance of polarization states in the system is crucial. As mentioned above, the parabolic mirrors have negligible effects on polarization states. However, different beam splitters could potentially twist the polarization, causing errors in the characterization of the metasurfaces.

Four types of beam splitters were therefore tested: calcium fluoride, sapphire, and germanium with 1mm and 2mm thickness. To characterise the beam splitters, unpolarised infrared light transmitted through the beam splitter was reflected back by a gold mirror, then followed the beam path to pass through a linear polarizer before incident on the detector, as shown schematically in Figure 4.14.

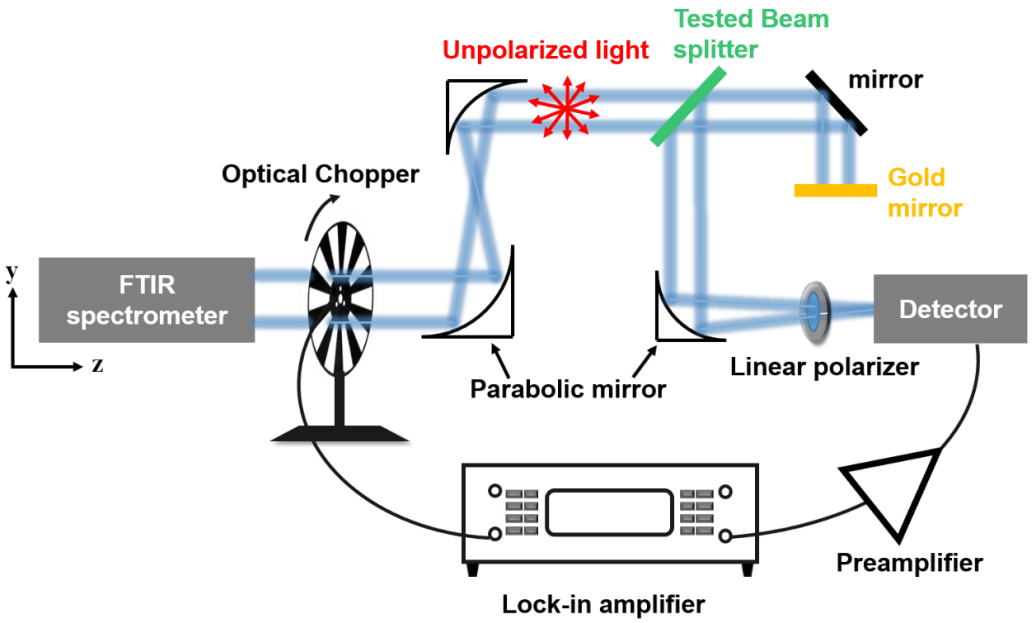

Figure 4.14 Schematic diagram of reflection system to test beam splitters

For each beam splitter, the reflected signal were measured with linear polarizer at 4 different angle: 0, 45, 90 and 135 degree, where the wire grid on polarizer is aligned on 0 degree. The 45 increment is set to cover 180 degrees of direction. The measured reflection signal from four different beam splitter are shown in Figure 4.15.

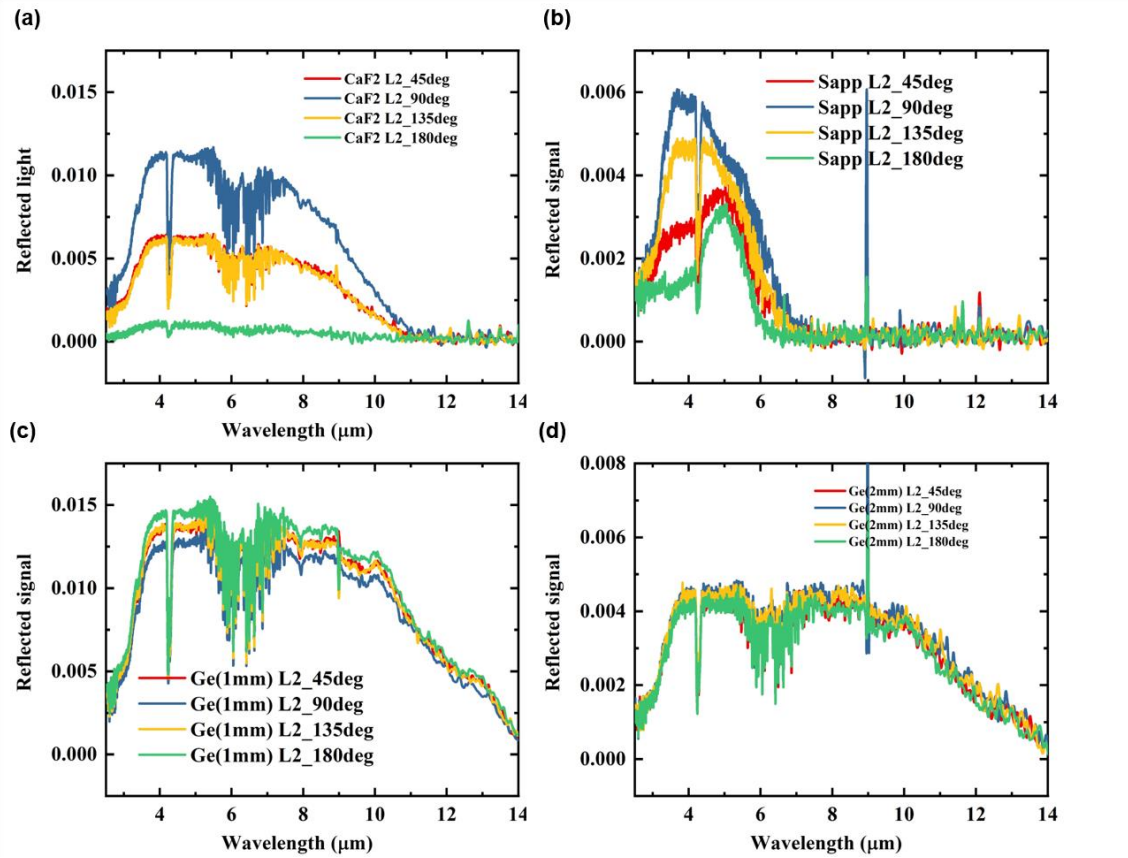

Figure 4.15 Measured reflection of (a) CaF_2 (b) Sapphire (c) 1mm thick germanium (d) 2mm thick germanium beam splitters

In Figure 4.15 (a) and (b), there are different levels of signal detected when the linear polarizer is at different angle. This indicates that the detected light is not unpolarised and so the calcium fluoride and sapphire beam splitter selectively transmit and reflect light with certain polarizations. For germanium with 1mm thickness, there is an observable difference in the measured reflection for

different angles of the linear polarizer as shown in Figure 4.15 (c), but this not the case for the 2mm thick germanium in Figure 4.15 (d). In comparison, the light almost equally pass through germanium beams splitter at tested angles indicating the light still consists of polarized components in all direction. In conclusion, the 2mm thick germanium beam splitters show good maintenance on the polarization state in the system and was therefore chosen for the reflection system

4.4 Summary

The first of this chapter was an introduction to the metasurface fabrication process, which starts with substrate cleaning. Electron-beam lithography, which is the used to define individual nano-resonators was then described. The metallisation and lift-off process, the last stages of the fabrication were then discussed. The second section of the chapter is focussed on sample characterisation. First we describe two methods, namely: optical microscope and scanning electron microscope, to inspect fabricated sample on nanoscale. Next, there was an introduction to mid-infrared FTIR spectroscopy, along with a summary of the operation mechanism. Finally, the extra self-built reflection measurement setup was described. Together with the FTIR spectrometer this allows measurement of the reflectivity spectrum, and also the Stokes parameters, to characterise the performance of the metasurface.

The next chapter describes the characteristics of a mid-infrared nanorod-based metasurface using both simulation and experiments.

5 Broadband efficient mid-infrared linear-to-circular polarization conversion using a nanorod-based metasurface

5.1 Introduction

Building on the work on metasurfaces for the terahertz region [67], this chapter mainly investigates metasurfaces, consisting of arrays of nanorod-based resonators, for efficient linear-to-circular polarization conversion in the technologically important mid-infrared spectrum. In simulation, two resonances at 3.4μm and 7.9μm are detected, and the metasurface is verified to convert linearly incident polarized light into circularly polarized light in reflection, with near unity conversion efficiency, within the off-resonance range. A thorough analysis of the two resonances is undertaken to understand the design by exploring the current density distribution, the near field distribution profile of the structure and the dependence on geometric parameters. The angular dependence characteristic is studied to prove that normal incidence is the key for the metasurface to work with a large bandwidth. Fabricated metasurfaces were then characterised, with the polarization state of the reflected beam determined by measuring four Stokes parameters using a reflection system based on a FTIR spectrometer (see Section 4.3). Experimental results were in good agreement with those from simulations, showing that the structure enables conversion of linearly polarized light into circularly polarized light across the wavelength range

4-7μm with polarization conversion efficient up to 83%. Such metasurfaces, which have subwavelength thickness, could potentially replace conventional quarter wave plates, but could also be used for circular dichroism spectroscopy in the mid-infrared region, allowing the relative easy differentiation of chiral enantiomers.

5.2 Design of nanorod-based metasurface

A schematic diagram, and scanning electron microscope (SEM) image of a fabricated sample, of the metasurface studied are shown in Figure 5.1 (a) and (b) respectively. Simulations were undertaken using the FDTD software Lumerical, as described in Chapter 3, with a single unit cell modelled with periodic boundary conditions in the x- and y-directions over a period of 2.6μm, and a light source linearly polarized in the y-direction incident along the z-direction. PML absorbing boundary conditions are set along the z direction to absorb incident light with minimal reflections.

The structure of a unit cell consists of a 100nm thick aluminium ground plane at the bottom, followed by a 600nm thick silicon dioxide layer, with a 3.2μm by 400nm gold rod resonator oriented at 45 degrees to the edges of the device (x axis) on the top. Values of gold and aluminium conductivity were taken as $4.5 \times 10^7/\Omega m$ and $3.75 \times 10^7/\Omega m$ respectively to be consistent with those used in previously reported mid-infrared studies [88], [89], [93], with the refractive index of silicon dioxide taken from the Lumerical database (in turn taken from Palik [87]). The mesh size was set as 5nm in the z-direction, with the mesh boundary along

the interface of metal and silicon dioxide to guarantee the accuracy of simulation results.

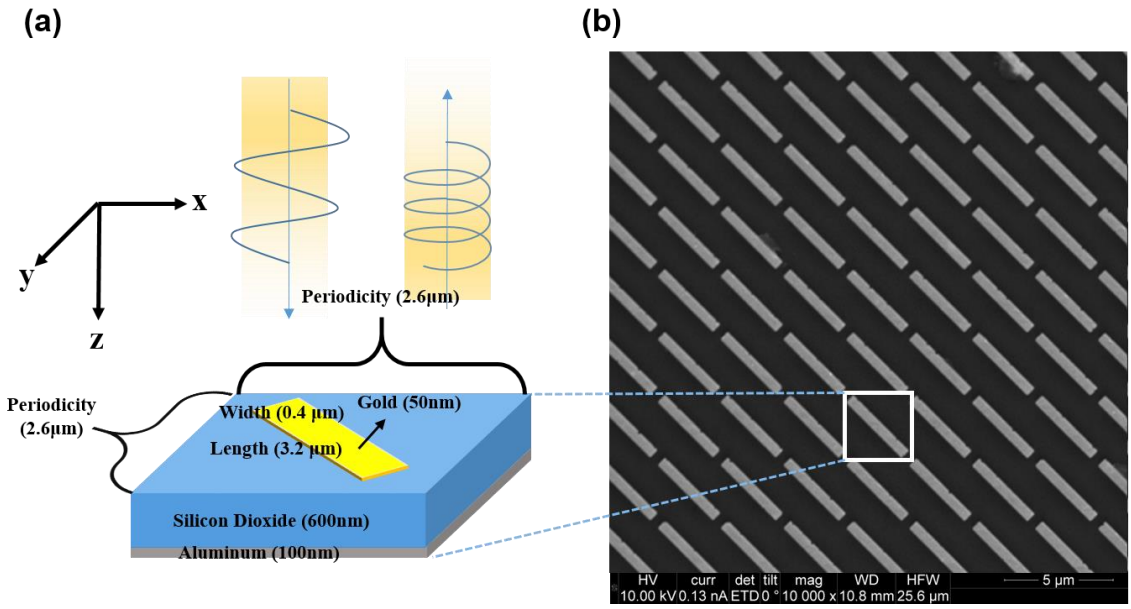

Figure 5.1 Schematic of nanorod-based metasurface. (a) The schematic of one unit cell of nanorod-based metasurface with geometric parameters. The device is placed on the x-y plane and light travels along z direction. (b) SEM photo of fabricated sample with 10000x magnification.

5.3 Simulation results

5.3.1 Reflectivity and phase spectrum

In order to investigate the polarization conversion of nanorod-based metasurface, the incident light is resolved into two orthogonal components polarized along the rod and perpendicular to rod as shown in Figure 5.2 (a). At normal incidence, we performed the reflectivity and phase spectrum of metasurface under two orthogonal polarizations respectively and the simulation results are displayed in Figure 5.2 (b) and (c). From Figure 5.2 (b), it is clear that the metasurface exhibits an anisotropic optical response for the two incident orthogonal polarizations,

whilst at the same time near unity reflectivity is obtained in the off-resonance between wavelengths of approximately 4μm to 7μm. When the incident electric field component is parallel to rod (marked with red curve), the two distinct resonances excited at 3.4μm and 7.9μm result in decreases in the simulated phase, as shown in Figure 5.2 (c). On the other hand, when the field is orthogonal to the rod (marked with blue curve), there is negligible interaction between the light with resonators. As a result, the phase spectrum for $E_{\perp}$, also shown in Figure 5.2 (c), is smoothly changing with relatively weak wavelength dispersion over a wide wavelength range. In the off-resonance wavelength band from approximately 4μm to 7.5μm (indicated in grey region in Figure 5.2 (c)), the phase difference between the two light components is relatively stable with the magnitude at a value of around $-\pi/2$. As a consequence, the combined wave will become circularly polarized light. This verifies that incident linearly polarized wave is converted into circularly polarized wave and the nanorod-based metasurface functions as a quarter wave plate within the off-resonance region. The calculated circular polarized state of reflected light is plotted as a function of wavelength in Figure 5.2 (d). R_L, R_R represent reflection for left and right circularly polarized light. The data shows that the reflected light is almost pure left-handed circularly polarized light, with conversion efficiency over 90%, in the range from 4μm to 7.5μm. Finally, the diffraction effect was investigated due to the periodic array arrangement of metasurface through FDTD simulations with provided grating analysis group which provides results including numbers of diffraction order, diffraction angles and grating efficiencies in response of broadband

wavelength range [99]. Simulation results show that, at normal incidence, the metasurface only support one diffraction order in reflection from 3-10um meaning the incident light is simply reflected with no diffraction.

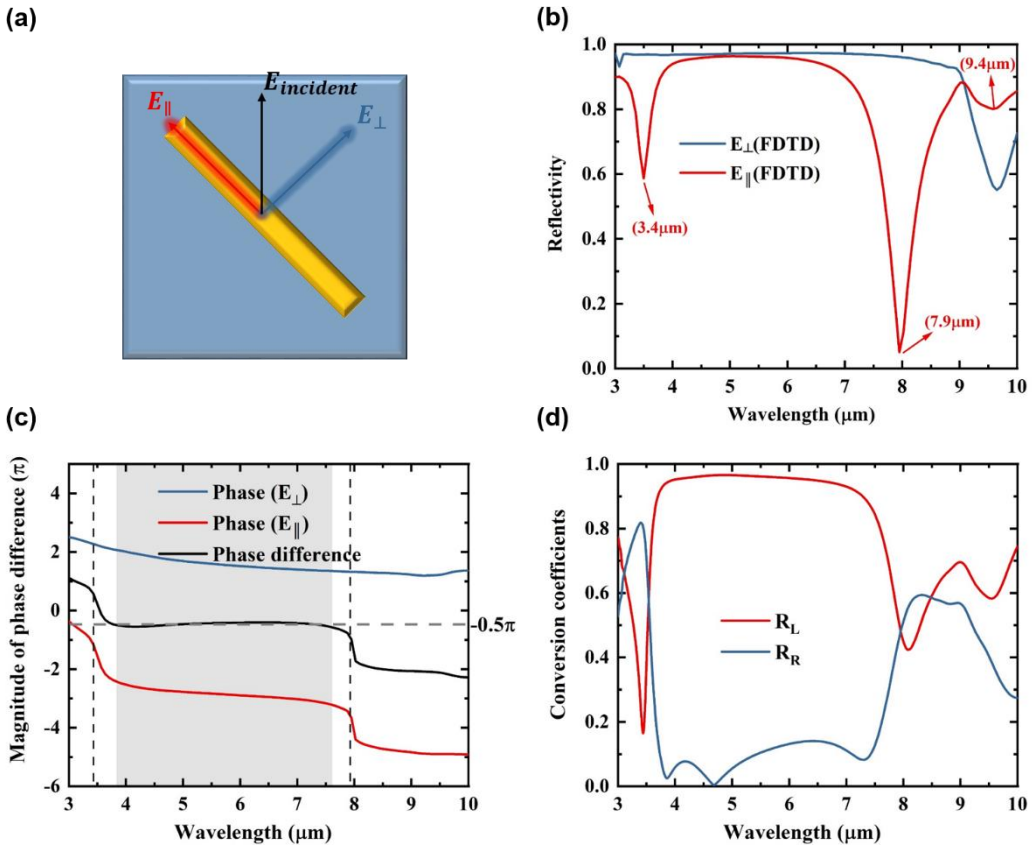

Figure 5.2 Simulation results of nanorod-based metasurface. (a) Schematic showing the polarization of the two orthogonal components in simulation. $E_{\parallel}(E_{\perp})$ stands for the incident light is polarized parallel (orthogonal) to rod. (b) Amplitude and (c) phase spectrum under excitation of two orthogonal components by FDTD full-wave simulation. (d) The retrieved normalized circularly polarized light reflected from metasurface.

5.3.2 Resonances analysis

With the incident light parallel to the rod, three distinct resonances are observed in the simulated reflection spectrum (Figure 5.2 (b)). The resonance at 9.4μm originates from the phonon absorption of silicon dioxide, and the wavelength of this resonance does not vary with the shape of the resonators. The resonances

at 3.4μm and 7.9μm, however, are based on different underlying mechanisms. The resonance at 3.4μm is consistent with the gap surface-plasmon (GSP) mode [62], [100], which can be more generally understood as a magnetic resonance with the magnetic dipoles being generated by the anti-symmetric surface current distribution in the rod resonator and aluminium ground plane. This can be verified by the simulated current density distribution and magnetic field distribution at cross plane. In order to calculate current density, FDTD assume that the effective permittivity of the metasurface is contributed by background permittivity ε_0 and permittivity correlated to current density ε_J. Then the displacement field vector for a given electric field can be calculated based on [101]:

$$\boldsymbol{D} = \varepsilon_{matesurface}\boldsymbol{E} = (\varepsilon_0 + \varepsilon_J)\boldsymbol{E} \tag{5.1}$$

Then we have:

$$\boldsymbol{D} = \boldsymbol{D}_0 + \frac{i\boldsymbol{J}}{\omega} \tag{5.2}$$

Then we yield the current density as:

$$J = \boldsymbol{D}_0 - i\omega\boldsymbol{D} \tag{5.3}$$

As shown in equation *(5.3)*, the current density can be calculated through electric field and refractive index of metasurface which can be extracted through analysis group. In FDTD simulation, mesh size is set into dx*dy*dz=50nm*50nm*5nm in a mesh override region of 2.6μm*2.6μm*1.4μm. Calculated current density vector J can be visualised at a slice on xy, yz and xz plane. In order to verify the anti-symmetric surface current distribution in the rod resonator and the aluminium

ground plane, we plot current density distribution in xy plane locating in (a) rod and (c) aluminium layer at resonance of 3.4μm in Figure 5.3. As Comparison, Figure 5.3 (b) and (d) illustrate the current density at 7.9μm. In both cases, it is clearly that the current vector generated in the rod has the opposite direction to that generated in the aluminium. Nevertheless, the current density at 3.4μm are 10 times stronger than 7.9μm. This indicates that the anti-symmetric current distribution exhibit, characteristic of the gap surface-plasmon (GSP) mode, which is the dominant effect at the 3.4μm resonance, while the resonance at 7.9μm originates from a different mechanism.

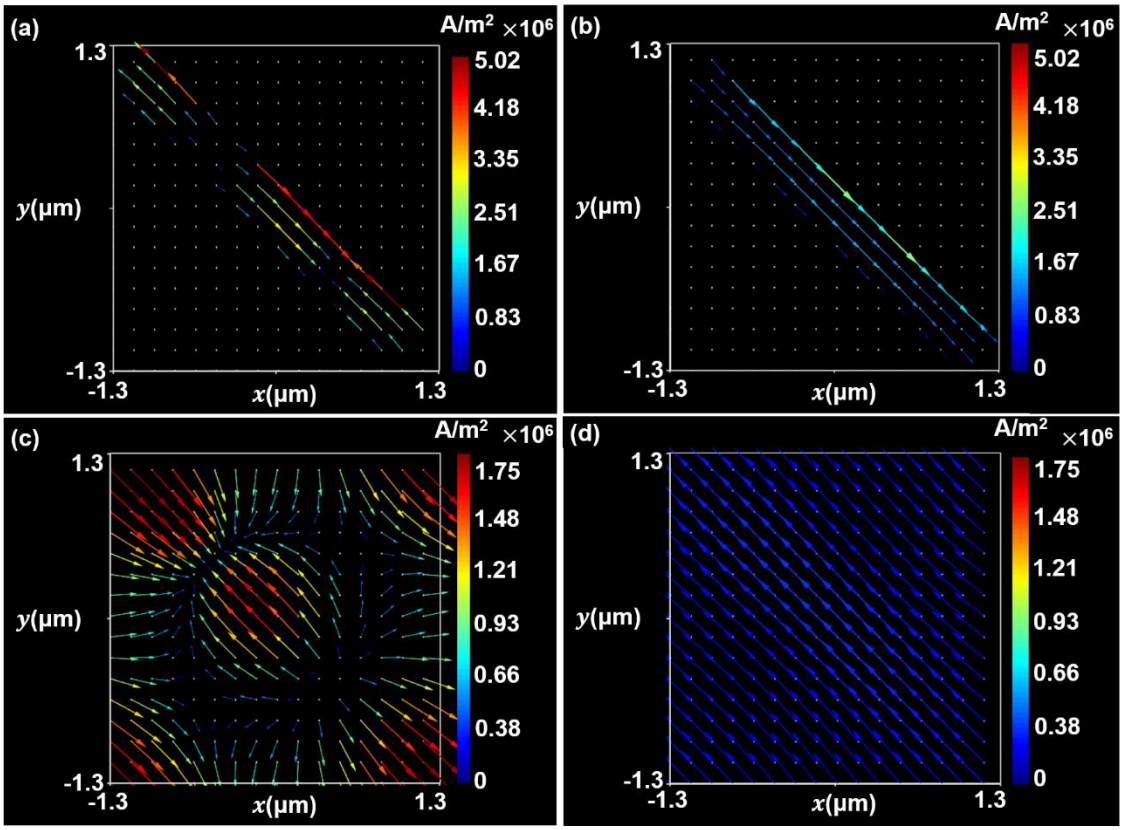

Figure 5.3 Simulated current density distribution in the plane across (a) rod at 3.4μm (b) rod at 7.9μm (c) aluminium at 3.4μm (d) aluminium at 7.9μm

The mechanism underpinning the two resonances can be verified by inspection of the magnetic field profile. Figure 5.4 shows the calculated magnetic field profiles for the resonances at 3.4μm and 7.9μm in the xz-plane at the centre of metasurface, where the outline of the structure is marked in white. In both cases, it is clear that the magnetic field is confined to the sides of rod and gradually reduces in strength as a function of depth in the silicon dioxide. However, within the same scale bar, the maximum value of magnetic field at 3.4μm is almost twice as strong than that at 7.9μm, and same for the volume of localised region for enhanced magnetic field. The strong localisation of magnetic field originates from the anti-symmetric current distribution in the metal layer which is consistent with the fundamental GSP mode mentioned in above paragraph.

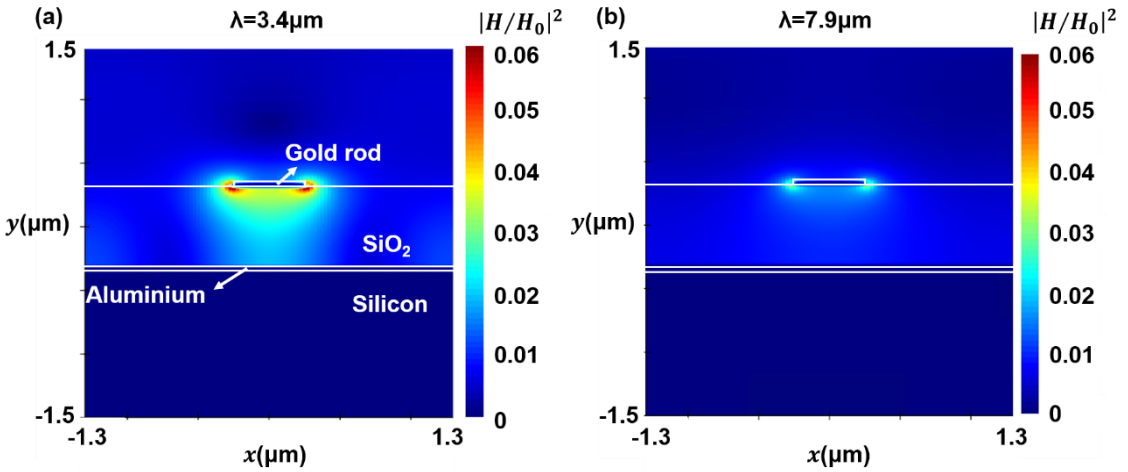

Figure 5.4 Magnetic field distribution in xz-plane at center of metasurface at resonances of (a) 3.4μm and (b) 7.9μm.

The GSP mode is a result of complex near-field coupling between the top and bottom metal layers as well as adjacent resonators, therefore, the resonance wavelength is influenced by spacer thickness and periodicity. The effects of silicon dioxide thickness and unit cell periodicity on the reflectivity are shown in

Figure 5.5 (a) and (b). In Figure 5.5 (a), we studied the periodicity varies from 2.6μm to 5μm. To begin with, here are only two resonances at 3.4μm and 7.9μm. As the periodicity increases, the coupling between adjacent resonators decreases from the GSP mode, and the resonance at lower wavelength shows significantly red-shift. As a result, the off resonance bandwidth becomes narrower, and is inversely proportional to the periodicity. In order to achieve a maximum broadband wavelength range, a periodicity of 2.6μm was chosen for the metasurfaces studied in this thesis.

The SiO_2 thickness also play an important role in the characteristics of the structure, and Figure 5.5 shows the effect of varying the SiO_2 thickness from 0 to 1000nm. With no SiO_2 spacer, the reflectance is unity across the entire spectrum. As the SiO_2 spacer layer becomes thicker, the two resonances become visible in the spectrum. The resonance strength at 3.4μm first becomes stronger, then weaker, as the SiO_2 thickness increases due to less coupling between the top and bottom metal layers. However, unlike the periodicity, the thickness of SiO_2 only has a negligible impact on the resonance wavelength. As the SiO_2 thickness also strongly determines the relative phase delay, we selected 600nm as SiO_2 thickness to ensure a 90 degree phase delay between the components of incident light.

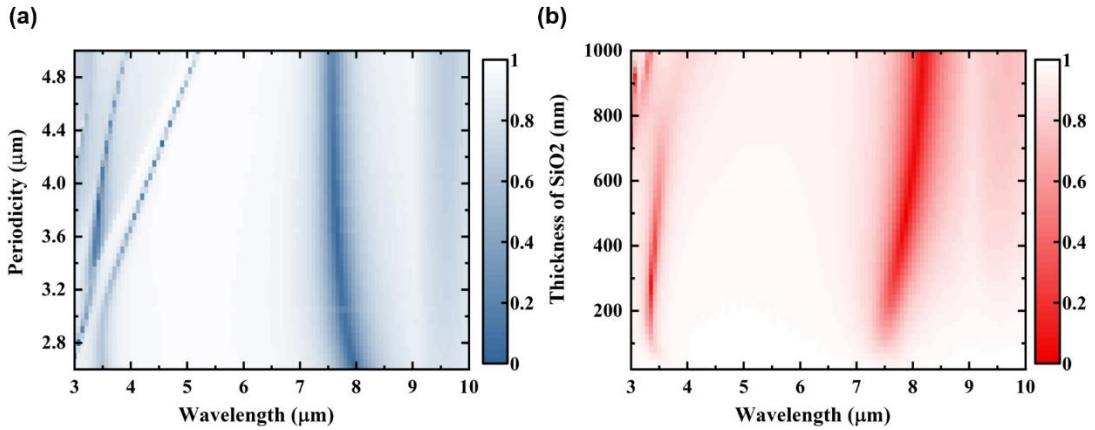

Figure 5.5 Reflectivity spectrum of $E_{\parallel}$ as a function of (a) periodicity and (b) thickness of silicon dioxide, respectively. Colorbar corresponds to reflectivity value from 0-1.

In contrast to the resonances at 3.4μm, the resonance at 7.9μm, doesn't show the same magnetic enhancement and localization, and can be understood as a Fabry-Perot cavity like mode where the two layers of metal are only linked by multi-reflection in the spacer layer, with negligible near-field coupling [102]. A minima in the reflection indicates that the incident light is trapped by the metasurface as a result of destructive interference between multi-reflection and direct reflection from metasurface. This is determined by the dispersive properties of dielectric spacer and shape of resonators. The schematic diagram of interference theory at normal incidence is shown in Figure 5.6, where the resonator rod array is considered as a homogeneous layer medium 1, and the silicon dioxide layer is treated as medium 2. There are incident light $\boldsymbol{E_{in}}$ and multi-reflected light $\boldsymbol{R_1}$, $\boldsymbol{R_2}$, $\boldsymbol{R_3}$, etc, where $\tilde{r}$ and $\tilde{t}$ represent the reflection and transmission coefficients between the two media. These are complex numbers carrying phase information where $\widetilde{t_{12}}$ is the transmitted coefficients from medium 1 to medium 2. $\widetilde{r_{12}}$ is the reflected coefficients from medium 1 to medium 2. Similarly, $\widetilde{t_{21}}$ is the transmitted coefficients from medium 2 to medium 1. $\widetilde{r_{21}}$ is the

reflected coefficients from medium 2 to medium 1. The incident light $\boldsymbol{E_{in}}$ (which is assumed to be unity) is first incident on the interface between mediums 1 and 2, with part of the light reflected back to air with the reflected coefficients of $\widetilde{r_{12}}$, part transmitted into the dielectric material with the transmitted coefficients of $\widetilde{t_{12}}$ and hitting the bottom metal plane, whilst phase index accumulates $e^{j\beta} = e^{jn_{spacer}k_0 d}$ simultaneously in propagation, where n_{spacer} is the dispersive refractive index of silicon dioxide, k_0 is the wavenumber in free space and d is the thickness of silicon dioxide. This light carrying power of $\widetilde{t_{12}}\, e^{j\beta}$ will be reflected completely by the aluminium plane, with a power of $\widetilde{-t_{12}}\, e^{j\beta}$ due to the reflection coefficient of -1. The reflected light will propagate in the dielectric medium, before being reflected by the resonator array, therefore forming a FP-cavity resonance. The overall reflection will be simply sum of all the reflection light as:

$$\boldsymbol{R = R_1 + R_2 + R_3 + \cdots} \tag{5.4}$$

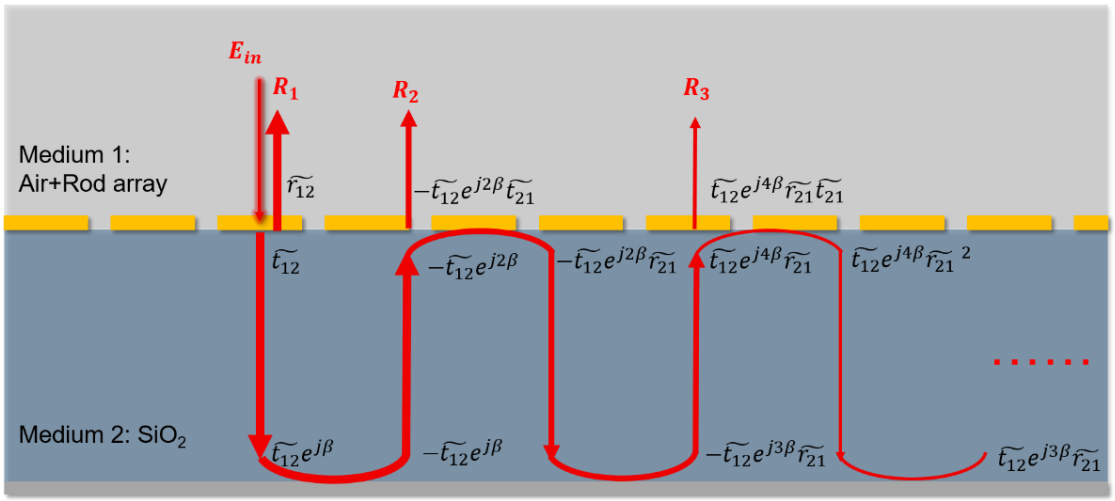

Figure 5.6 Schematic diagram of interference theory.

Replacing$\boldsymbol{R_1}$, $\boldsymbol{R_2}$, $\boldsymbol{R_3}$ …with reflected coefficients and transmitted coefficients:

$$\boldsymbol{R} = \widetilde{r_{12}} + \left(-\widetilde{t_{12}} e^{j2\beta} \widetilde{t_{21}}\right) + \widetilde{t_{12}} e^{j4\beta} \widetilde{r_{21}} \widetilde{t_{21}} + \left(-\widetilde{t_{12}} e^{j6\beta} \widetilde{r_{21}}^2 \widetilde{t_{21}}\right) + \cdots \tag{5.5}$$

The total reflection coefficient can then be calculated as:

$$\begin{aligned} \boldsymbol{R} &= \widetilde{r_{12}} - \widetilde{t_{12}} \widetilde{t_{21}} e^{j2\beta} \left[\frac{1 - \left(-e^{j2\beta} \widetilde{r_{21}}\right)^n}{1 - \left(-e^{j2\beta} \widetilde{r_{21}}\right)}\right] \\ &\approx \widetilde{r_{12}} - \frac{\widetilde{t_{12}} \widetilde{t_{21}} e^{j2\beta}}{1 + e^{j2\beta} \widetilde{r_{21}}} \end{aligned} \tag{5.6}$$

According to equation *(5.6)*, except for phase parameter β, the complex transmission and reflection coefficients: $\widetilde{t_{12}}, \widetilde{r_{12}}, \widetilde{t_{21}}, \widetilde{r_{21}}$ can be obtained by simulating a unit cell without aluminium reflector to calculate the total reflectivity as shown in Figure 5.7 (a). In simulations, the thickness of silicon dioxide was taken as half of original value for simplicity. The plane wave source is set to travel along $-z$ direction to acquire $\widetilde{t_{12}}$, $\widetilde{r_{12}}$, and $+z$ direction to calculate $\widetilde{t_{21}}, \widetilde{r_{21}}$. The reflectivity and corresponding phase value of rod resonator with silicon dioxide as a function of wavelength is shown in Figure 5.7 (b) and (c). A dipole resonance at 6.4μm is detected as a minima in transmission or a maxima in the reflectivity spectrum. As a pair of $\widetilde{t_{12}}$, $\widetilde{r_{12}}$ show similar value with $\widetilde{t_{21}}, \widetilde{r_{21}}$, it confirms that the direction of incident light have negligible impact on the intensity of coefficients. However, its influence on phase spectrum is significant as shown in Figure 5.7 (c). As a result, the calculated reflectivity based on simple interference theory has a minima reflectivity at a wavelength of 7.91μm, as shown in Figure 5.7 (d). This

is consistent with the resonance observed in the FDTD simulation at around 7.94μm. The excellent agreement validates that the resonance at 7.9μm can be understood as Fabry-Perot cavity like mode.

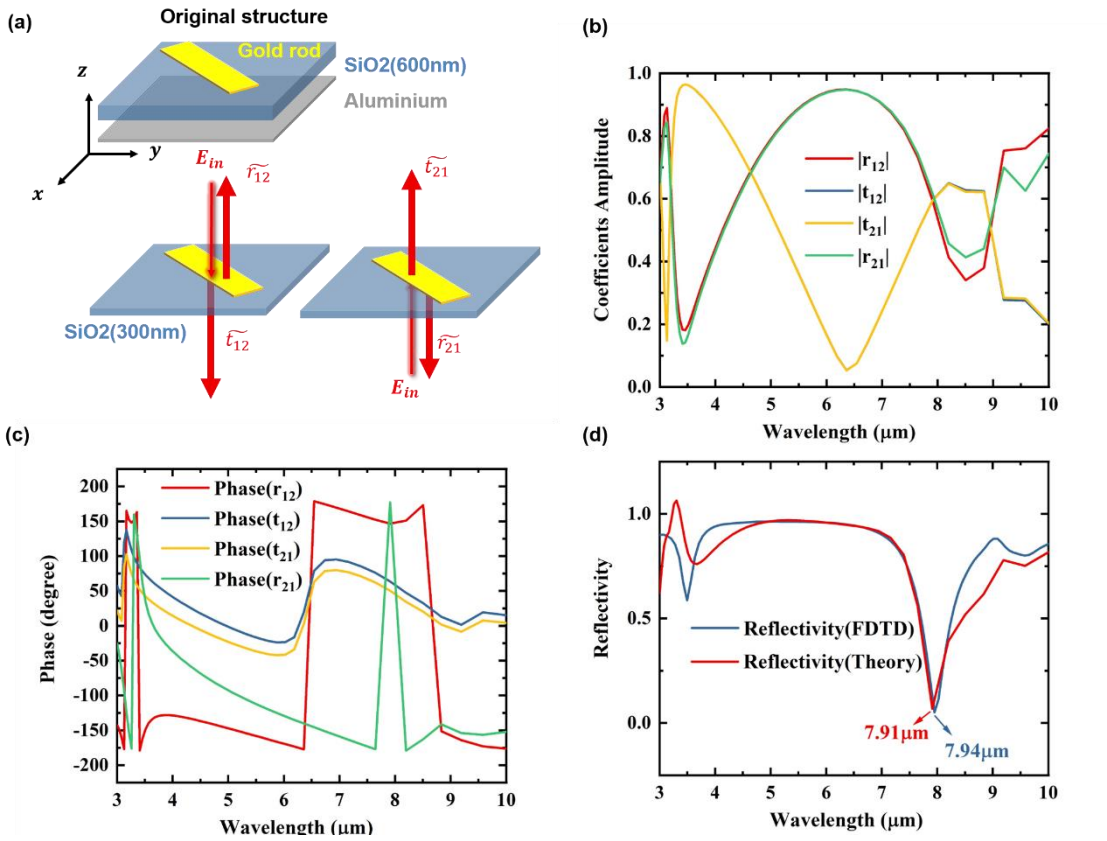

Figure 5.7 (a) Schematic diagram of original metasurface and the unit cell with beam path in simulation. (b) Simulated coefficients and (c) corresponding phase spectrum. (d) Reflectivity spectrum obtained from FDTD and interference theory.

Back to equation *(5.6)*, this light absorption dip at 7.9μm can be explained a result of destructive interference between the primary reflected light $\boldsymbol{R_1} = \widetilde{r_{12}} = r_{12}e^{j\phi 12}$ and superposition of multi-reflection $\mathbf{R_2} + \mathbf{R_3} + \cdots$. From the diagram of interference modes in Figure 5.6, the phase difference between $\boldsymbol{R_2}$, $\boldsymbol{R_3}$, etc. remains as $(2\beta + 180 + \phi_{21})$ and equal to 357 degree at 7.9μm. The phase difference is plotted as a function of wavelength in Figure 5.8 (a). Light incident on the rod resonators, and then reflected from the aluminium therefore

experiences a phase delay of 357 degrees. As a consequence, the multi-reflected light experiences constructive interference. The overall phase value of the superposition of the multi-reflected light $\mathbf{R_2} + \mathbf{R_3} + \cdots$, represented as the second term including negative sign in equation *(5.6)*, is calculated as -29.7° in Figure 5.8 (b) . As comparison, the phase spectrum of the first term, representing as $\boldsymbol{R_1}$, is shown in Figure 5.8 (b). The phase difference (yellow line) between two term reach to 175.7° at 7.9μm which satisfy the requirement of destructive interference. This indicated that the multi-reflected light destructively interferes with direct reflection from rod resonator. As a result, the total reflection is almost zero at resonance. Although there is no near-field coupling in this mode, but the multi-reflections link top and bottom metal parts in this mode.

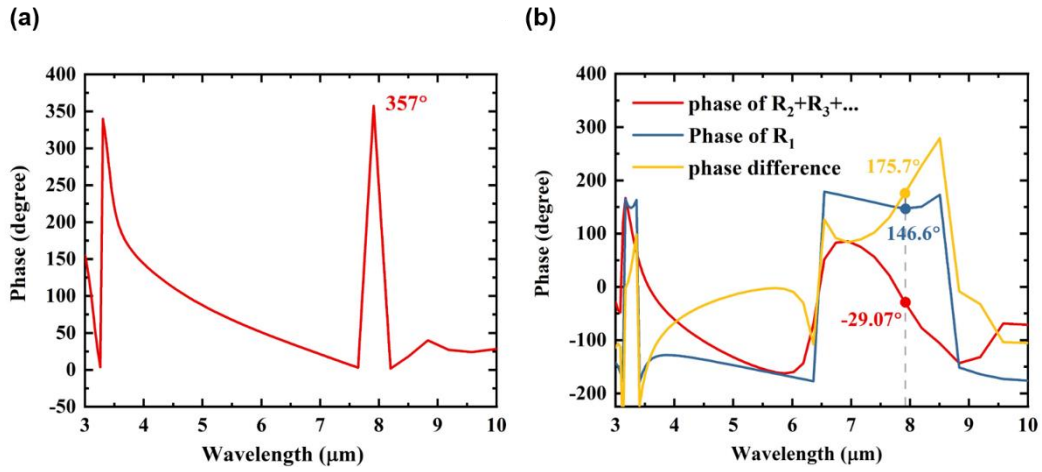

Figure 5.8 (a) Phase difference between $\boldsymbol{R_2}$, $\boldsymbol{R_3}$ etc.(b) Phase spectrum of primary reflection $\boldsymbol{R_1}$, sum of multi-reflection $\boldsymbol{R_2} + \boldsymbol{R_3} + \cdots$ and their phase difference.

5.3.3 Non-normal incidence

As discussed above, it's worth highlighting that normal incidence is of great importance to enable the nanorod-based metasurface to maintain a broadband

effective operation wavelength. As discussed in 5.3.1, the phase response of the optical resonator highly relies on excitation polarization. In order to create an ideal quarter waveplate, incident polarization must be at certain angle to excite rod resonator to produce a 90 degree phase shift between decomposed components. In this section, the characteristics of the metasurface with incident at oblique incidence, with some special cases.

An oblique incidence is defined by three angles: theta, phi and polarization angle as shown in schematically in Figure 5.9. Theta and Phi are the source angle, where theta describes the angle between the propagation vector of the incident beam and the surface normal (theta is between 0 and 90 degree), and phi defines the angle from the positive y-axis to the vector's orthogonal projection onto xy plane. There is also the polarization angle that describes the oscillation direction of the electric field vector of the incident light. All three angles contribute to the interaction between incident light and the resonators, and thus make impact the metasurface characteristics.

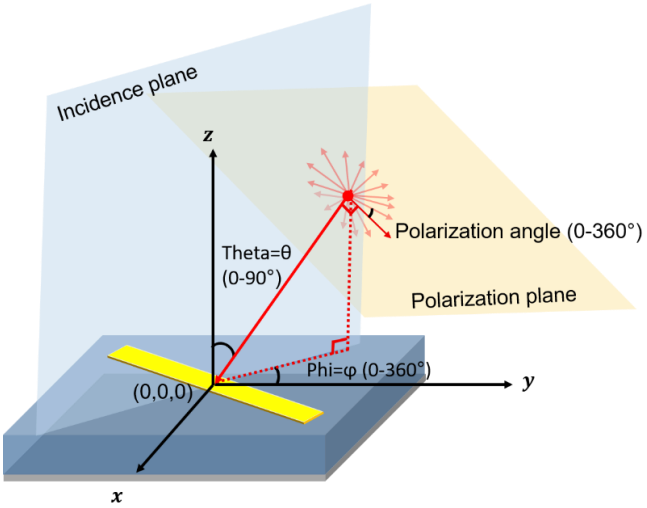

Figure 5.9 Schematic of a unit cell at oblique incidence.

For simplicity, we investigated the anisotropic property of the metasurface for two special cases at oblique incidence, when phi equals to -45° and -135°, with theta set to 10° in both cases. The decomposed two orthogonal polarizations are set as 0° and 90°, as indicated by the green and yellow arrows in Figure 5.10.

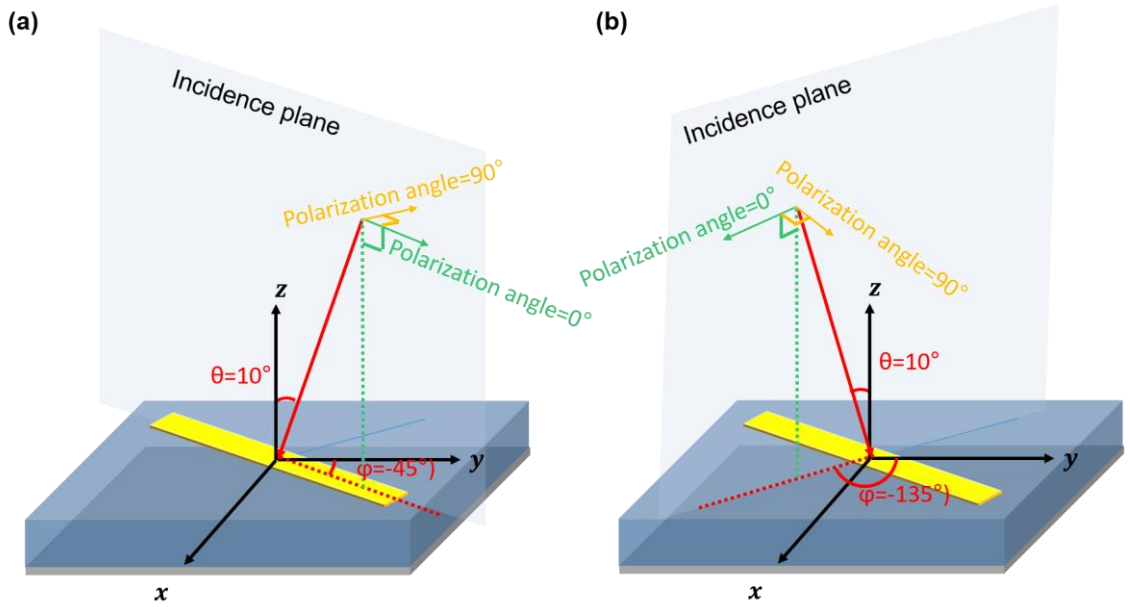

Figure 5.10 Schematic diagram for metasurface unit cell with oblique incidence. (a) $\varphi = -45°$. (b)) $\varphi = -135°$.

The simulated reflectivity and phase spectrum for the decomposed two orthogonal polarizations are plotted in Figure 5.11. In both situations when $\varphi = -45°/-135°$, there is a similar anisotropic response, where reflectivity is near unity across the entire spectrum (non-resonant mode) for one polarization, but contains multiple strong absorption minima for the other incident polarization (excitation mode). In excitation mode, the double-linked resonances around 3-3.5μm and a sharp resonance at 7.9μm seen when $\varphi = -45°/-135°$, can also be excited at normal incidence as discussed in the previous section. However, an extra resonance at 4.5μm can only excited when $\varphi = -45°$ for polarization

angle of 0°. This also results in a phase discontinuity as shown in Figure 5.11 (b), where a small phase jump can be observed in the blue curve. As a consequence, we cannot obtain an ideal quarter wave plate at 4.5μm because of the amplitude of this resonance, and the non 90 degree phase shift. By comparison, the demonstration of an anisotropic response when $\varphi = -135°$ is very similar to that at normal incidence plotted in Figure 5.2, where the reflectivity stays equal and the phase shift is -90 degree from 4μm to 6μm, confirming that the metasurface still functions as a quarter wave plate within the off-resonance wavelength range.

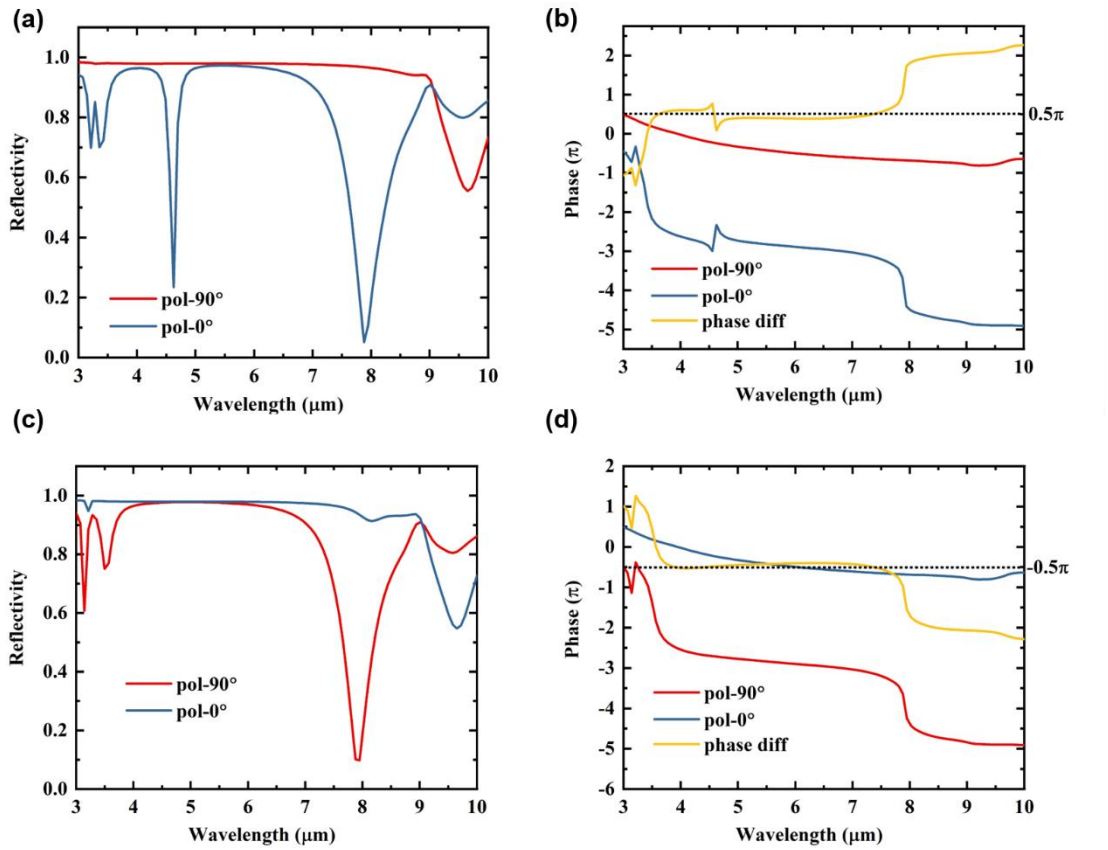

Figure 5.11 Simulated (a) amplitude and (b) phase spectrum under excitation of two orthogonal components when $\varphi = -45°$. Equivalent results in (c) and (d) when $\varphi = -135°$

5.4 Experimental results

5.4.1 Measured reflectivity

Samples were fabricated using the electron beam lithography techniques described in chapter 4. Measurements were conducted at room temperature under ambient conditions, with the reflectivity of the samples characterized using a Fourier transform infrared (FTIR) spectrometer as shown schematically in Figure 5.12. This setup is similar to that in Figure 4.12 but a x15 reflecting objective lens from Thorlabs were used to focus light onto the sample. With a pair of parabolic mirrors, the source beam size is reduced and then guided to the germanium beam splitter (ratio close to 1:1) which allows reflected light to be collected. The third off-axis parabolic mirror is used to focus the reflected light into a liquid nitrogen cooled HgCdTe detector with a 2–12 μm response, then the signal from the detector will be amplified by a low noise preamplifier before being passed to the FTIR spectrometer.

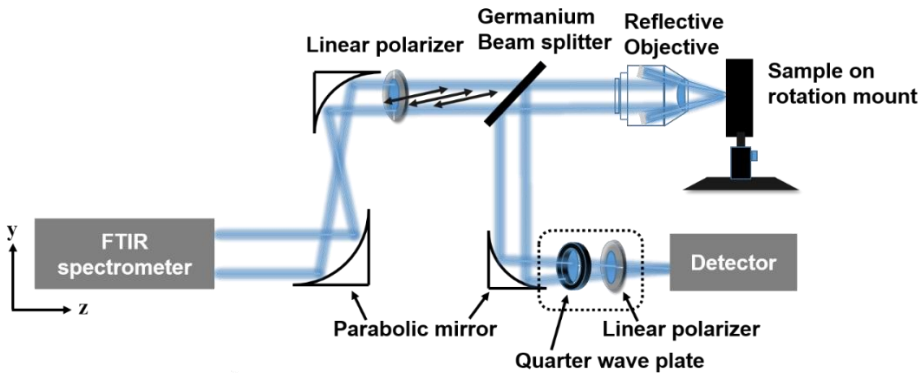

Figure 5.12 Schematic diagram of experiment set up at oblique incidence.

A wire grid linear polarizer with its optical axis orientated along y-axis, was placed before the beam splitter to generate linearly polarized incident light with electric vector along x axis. In our case, the light is oriented horizontally to the platform surface. The sample is mounted on a separate manual rotation stage with 360° continuous rotation as shown in Figure 5.14 (a) in which the incident light along x axis is marked with red arrow. The reflectivity of the two components ($E_{\parallel}$ and $E_{\perp}$) was performed by rotating the sample stage with 45° in anticlockwise or clockwise direction so that the rod resonators are either parallel or orthogonal to the polarization of incident light as shown in Figure 5.14 (b) and (c). The measured reflectivity was then normalized to that obtained from a substrate that had no resonators.

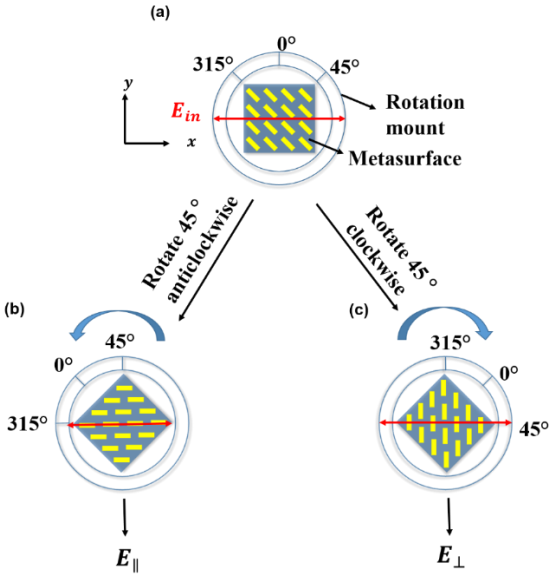

Figure 5.13 The illustration of incident light and metasurface to measure reflectivity of $E_{\parallel}$ and $E_{\perp}$. (a) The illustration of sample mounted on rotation mount. (b) The illustration of sample mounted on rotation mount to measure $E_{\parallel}$. (c) The illustration of sample mounted on rotation mount to measure $E_{\perp}$.

Reflecting objective lens provide angular incidence and the experiment results are plotted in Figure 5.14 (a) and (c) as a function of wavelength. In Figure 5.14

(a), when light polarization is parallel to resonators, minima in the measured reflectivity for $E_{\parallel}$ are observed at wavelengths of approximately 3.4μm, 3.6μm, 4.8μm and 7.9μm. The strength and wavelength of these resonances match those observed in simulations for non-normal incidence from Figure 5.11. (a), which verify that light is at non-normal incidence. This is due to the fact that reflective objective lens has intrinsic incident angle up to 35 degree. With the light orthogonal to the rods, near unity reflectivity over the operation wavelength range is be observed in the spectrum as shown in Figure 5.14 (b). As comparison, the reflectivity measured without the reflective objective lens are plotted in Figure 5.14 (c) and (d). In this case, the metasurface are excited at normal incidence. By comparing the reflectivity at non-normal incidence, it is clear that the resonances at 3.6μm and 7.9μm remain however the resonances at 3.4μm and 4.8μm disappear. As described earlier, these two remaining resonances correspond to the gap surface plasmon (GSP) mode and Fabry-Perot cavity mode, respectively. The resonances at 3.4μm and 4.8μm disappear at normal incidence which confirms that these two resonances are angular dependence. These additional resonances, arising from non-normal incidence, will narrow the working bandwidth of the metasurface as a quarter wave plate. Therefore, it is important to take incident angle into consideration in order to perform metasurface in a broadband wavelength range.

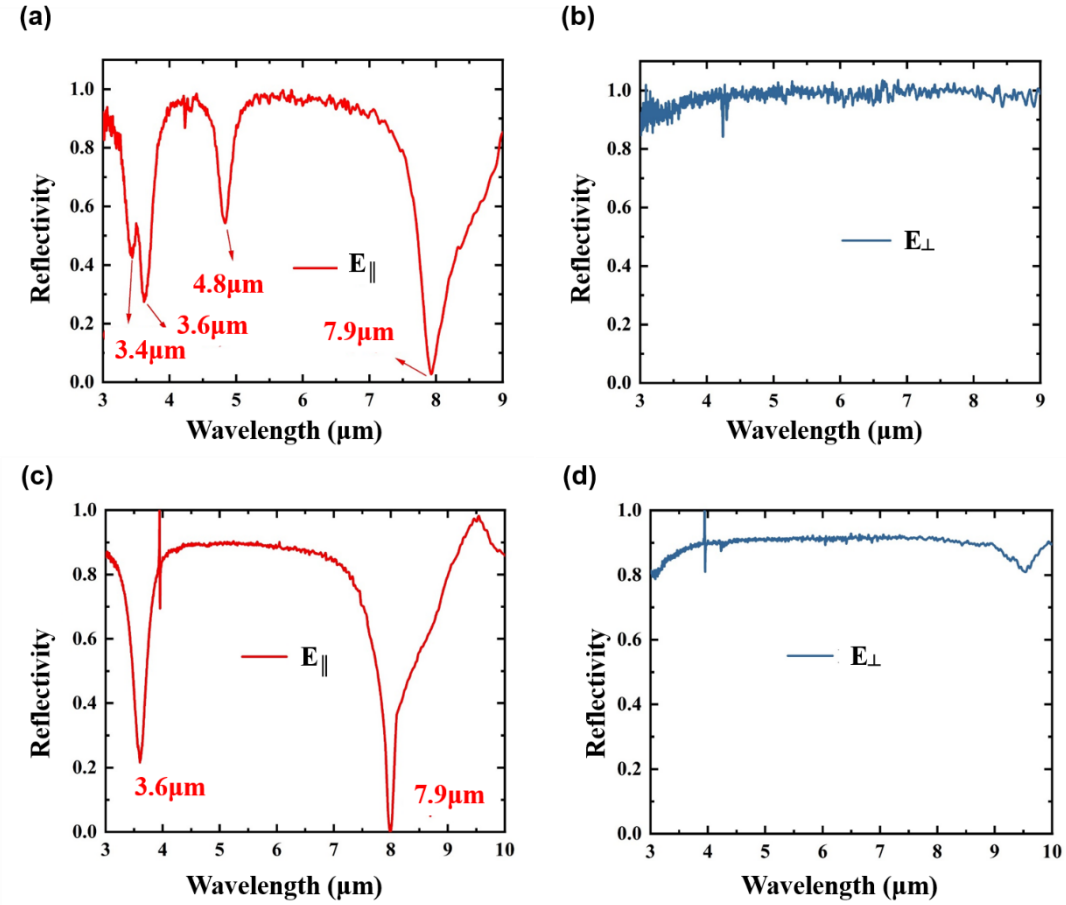

Figure 5.14 The direction between incident light and metasurface with the measured reflectivity. Reflectivity of (a) $\boldsymbol{E}_{\perp}$ and (c) $\boldsymbol{E}_{\parallel}$ at non-normal incidence. Reflectivity of (b) $\boldsymbol{E}_{\perp}$ and (d) $\boldsymbol{E}_{\parallel}$ at normal incidence.

5.4.2 Measured Stokes parameters for non-normal incidence

To further characterize the properties of the metasurface, the Stokes parameters, which give a direct physical interpretation of the state of polarization of a given electromagnetic field, were measured. In this case, sample is rotated at 0 degree so that the incident light is polarized at 45 degree to resonators. To measure the Stokes parameters an additional wire grid linear polarizer was placed between the parabolic mirror and detector, as shown in Figure 5.12 in the dashed rectangle. The classic measurement setup to obtain the Stokes parameters is depicted in

Figure 5.15 [103]. The measurement start with setting this additional linear polarizer with its optic axis along y-axis, 45 degree to y- axis and x axis to measure the intensity of the reflected beam from the metasurface. The data are marked as $P_1(0^\circ)$, $P_2(90^\circ)$, $P_3(45^\circ)$ respectively. These three measurements can calculate three Stokes parameters: S_0, S_1 and S_2 which describe the polarization ellipse of the light.

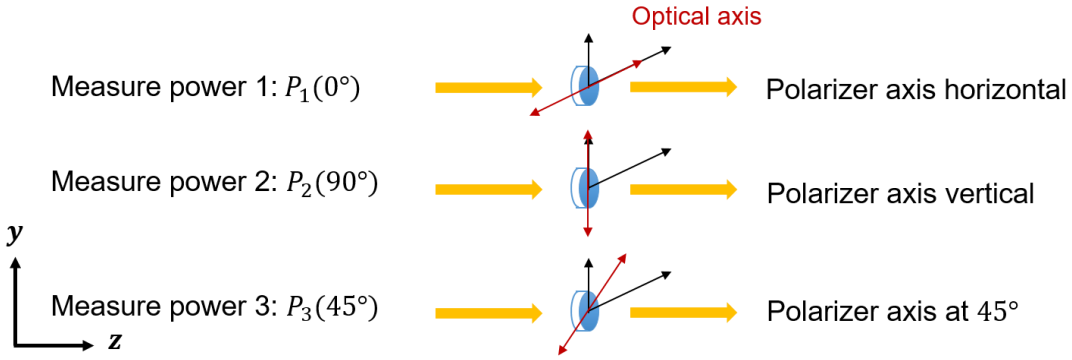

Figure 5.15 Classic measurement setup to obtain first three Stokes parameters.

The three Stokes parameters can be expressed as:

$$S_0 = P_1(0^\circ) + P_2(90^\circ) \tag{5.7}$$

$$S_1 = P_1(0^\circ) - P_2(90^\circ) \tag{5.8}$$

$$S_2 = 2P_3(45^\circ) - S_0 \tag{5.9}$$

The accurate polarization ellipse of the reflected beam can be characterized using the value of ellipse parameters E_{0x}, E_{0y} and orientation angle ψ, as indicated in Figure 5.16, with the parameters given by:

$$E_{0x} = \sqrt{\frac{1}{2}(S_0 + S_1)} \tag{5.10}$$

$$E_{0y} = \sqrt{\frac{1}{2}(S_0 - S_1)} \tag{5.11}$$

$$\psi = \frac{1}{2}\tan^{-1}\left(\frac{S_2}{S_1}\right) \tag{5.12}$$

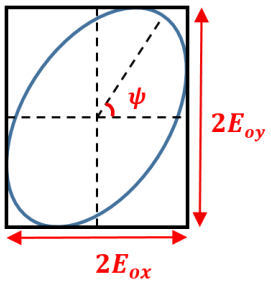

Figure 5.16 Indication of ellipse parameters E_{ox}, E_{oy} and orientation angle ψ.

Figure 5.17 (a) shows the calculated ellipse parameters E_{0x}, E_{0y} and orientation angle ψ calculated based on measured three stoke parameters (S_0, S_1 and S_2) with reflective objective lens from 3μm to 10μm. It is clear that the ellipse parameters E_{0x}, E_{0y} are almost equal from 3.8μm to 4.8μm indicating an ellipse close to circular however, they start to be different after 4.8μm which means the polarization is an tilted ellipse rather than circular. In conclusion, the linear-to-circular polarization conversion is interrupted by the resonance at 4.8μm originating from non-normal incidence. In Figure 5.17 (b), the ellipse parameter is plotted as a function of wavelength between 3.8μm and 4.8μm. Clearly, E_{0x}, E_{0y} show little wavelength dependence over the range 3.8μm to 4.8μm, as well as orientation angle ψ. Therefore, the polarization state of the beam is constant over this range. Within the wavelength range from 3.8μm to 4.8μm where linear-to-circular polarization conversion occurs, the polarization ellipse are illustrated at 4.1μm, 4.3μm, 4.5μm and 4.7μm respectively as examples to visualize the

polarization states at specific wavelength in Figure 5.17 (c). These clearly demonstrate that the reflected beam is circularly polarized in this range.

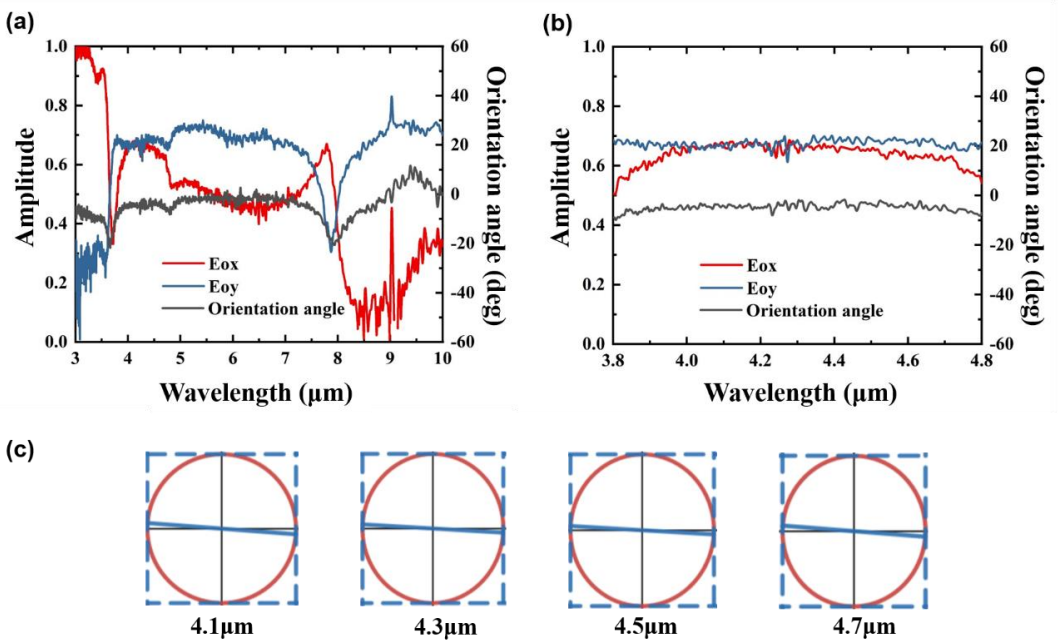

Figure 5.17 Experiment results of nanorod-based metasurface at non-normal incidence. (a) Calculated ellipse parameters E_{0x}, E_{0y} and orientation angle ψ based on Stokes parameters from 3μm to 10μm and (b) from 3.8μm to 4.8μm. (c) The schematic of polarization state of reflected beam at 4.1μm ($E_{0x} = 0.669, E_{0y} = 0.667, \psi = -4.33°$), 4.3μm ($E_{0x} = 0.648, E_{0y} = 0.685, \psi = -3.37°$), 4.5μm ($E_{0x} = 0.654, E_{0y} = 0.654, \psi = -3.35°$) and 4.7μm ($E_{0x} = 0.620, E_{0y} = 0.656, \psi = -4.38°$).

5.4.3 Measured Stokes parameters for normal incidence

As discussed above, the metasurface operation bandwidth is angular dependent, therefore, it is necessary to apply normal incidence to obtain its maximum working bandwidth. In the following discussion, the measured Stokes parameters at normal incidence without the reflective objective will be presented. Although in this case a slightly different measurement procedure was used, which allows the handedness of circularly polarized to be obtained, the obtained results are directly comparable to those obtained at non-normal incidence. In these measurements the fourth Stokes parameter S_3, was also measured, which required that a quarter

wave plate was inserted in the beam path with its fast axis fixed at 0° to the x-axis to obtain the intensity $P_4(0^\circ, 45^\circ)$, as shown in Figure 5.18.

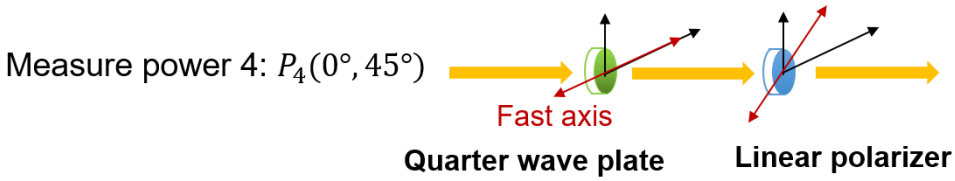

Figure 5.18 Classic measurement setup to obtain the forth Stokes parameters.

The fourth Stoke parameter can then be obtained as:

$$S_3 = S_0 - 2P_4(0^\circ, 45^\circ) \tag{5.13}$$

The Stokes parameters were measured at four different wavelengths, 3.5μm, 4.5-4.9μm, 6μm, 7μm using four different quarter waveplates. The measured Stokes parameters at normal incidence are shown in Figure 5.19, where grey bands correspond to the bandwidth of the particular quarter waveplate used for each measurement. In each figure, S_0 represents the total intensity of light, thus the value of S_0 is 1 1 across the entire band through normalisation. As discussed in section 2.2.3, S_1 and S_2 describe linear polarized light along with electric field vector oscillate along x/y axis and +45°/-45°. This means when linearly polarized light is along x/y axis, the value of S_1 will approach 1 whereas when linearly polarized light is along +45°/-45°, the value of S_2 will approach 1. This is seen in the measurement results shown in Figure 5.19 (a) where S_1 is close to 1, while S_2 is near zero, therefore, the light at 3.5μm is a linearly polarized light along the x/y axis. The fourth Stokes parameters S_3 is related to the handedness of

circularly polarized light. It can be observed ranging from -1 and 1 , the negative value implies left polarized light and positive value stands for right polarized light. In this context, when it is lineally polarized light, the value of S_3 will be 0 hence, it is perfectly circular polarization light when S_3 equal to ± 1. In the measurements shown in Figure 5.19 (a), S_3 equal to zero at 3.5μm which confirms that the light at this wavelength is linearly polarized. At 4.5-5μm the value of S_1 is approximately the same as that of S_2, whilst S_3 has value over 0.5. Similar results can be found at 6μm and 7μm. Compared with results in Figure 5.19 (a), the light detected at 4.5-5μm, 6μm and 7μm are more likely to be right-handed circularly polarized light.

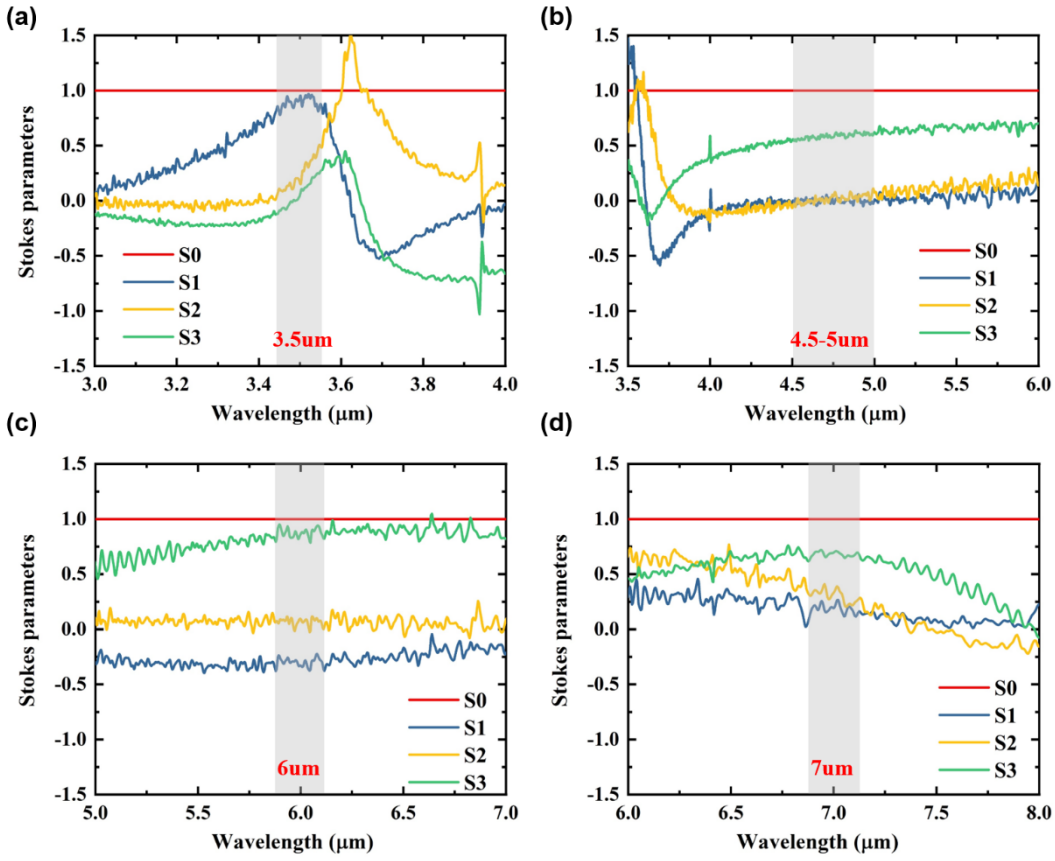

Figure 5.19 Measured Four Stokes parameters (a) at 3.5μm, (b) 4.5-5μm, (c) 6μm and (d) 7μm.

Based on equation *(5.10)-(5.12)*, the calculated ellipse parameters E_{0x}, E_{0y} and orientation angle ψ at each wavelength are plotted in Figure 5.20 Calculated ellipse parameters at (a) 3.5μm, (c) 4.5-5μm, (e) 6μm and (g) 7μm and the corresponding ellipse based on the marked value at (b) 3.5μm, (d) 4.5-5μm, (f) 6μm and (h) 7μm., where Savitzky-Golay smoothing was applied. At 3.5μm, 4.7μm, 6μm and 7μm, a set of ellipse values is picked and marked in the figure, with the corresponding ellipse shown in the right-hand figures. At 3.5μm, due to the fact that E_{0x} is close to 1 while E_{0y} is close to zero, we can predict that the detected light is more like to be a linearly polarized light, which is confirmed by the extracted ellipse. However, it is at 4.7μm, 6μm and 7μm where E_{0x} and E_{0y} have similar values, and have a weak wavelength dependence. This indicates that the polarization state is stable across a broadband wavelength range. In particular, E_{0x} and E_{0y} have identical values at 4.7μm, confirming that the detected light is a circularly polarized light at 4.7μm (the noise in the measurement of angle is due to the particular quarter waveplate used). The reflected light at 6μm and 7μm is no longer perfectly circularly polarized but is characterised as elliptically polarized light with axis ratio ($AR = \tan\chi$) ranging from 0.4 to 0.65. These experimental results show that for normal incidence the reflected light from the metasurface has been stably converted into elliptically polarized light across a broadband spectrum from 4μm to 8μm, with reflected light at 4.7μm being perfectly circularly polarized.

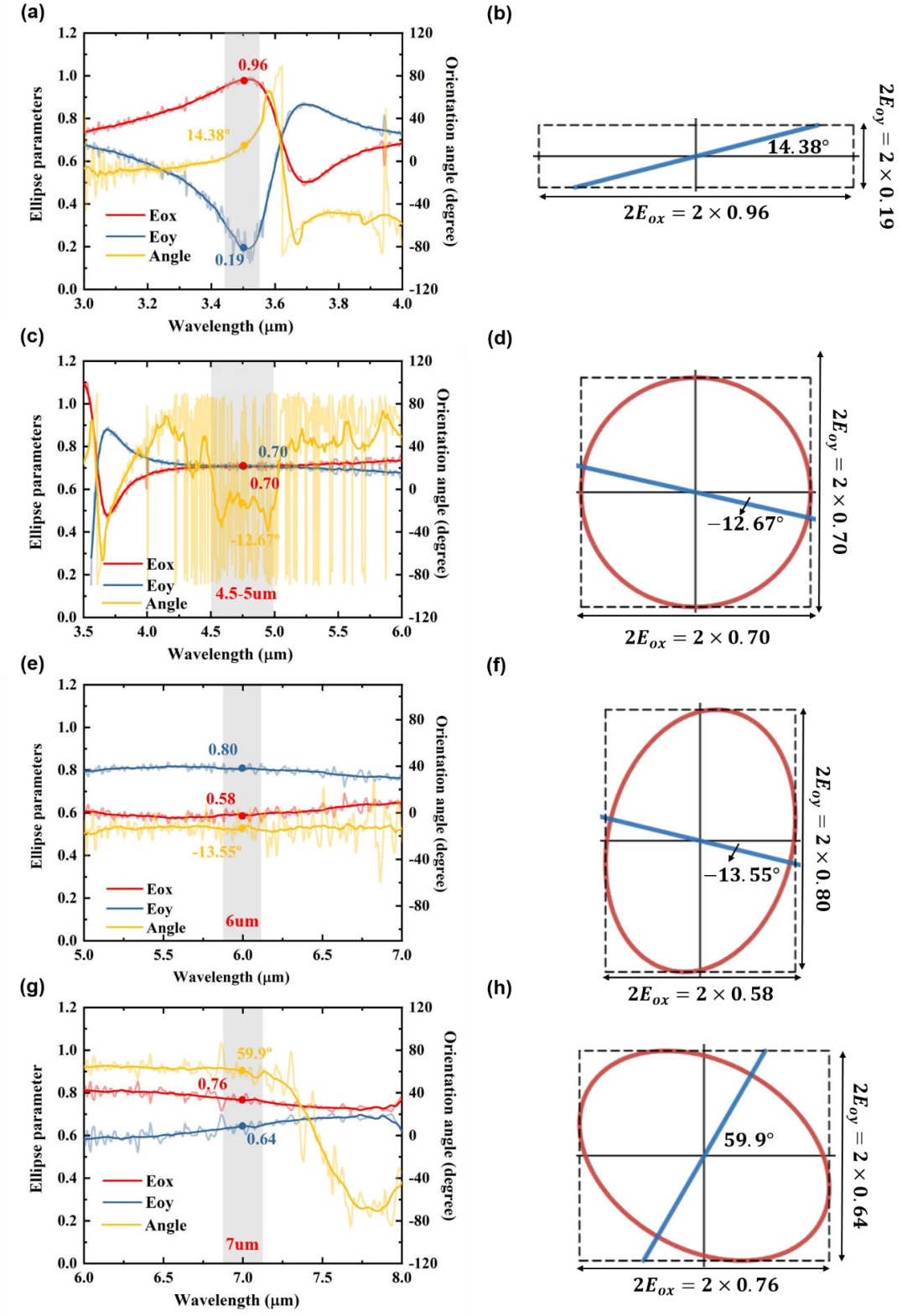

Figure 5.20 Calculated ellipse parameters at (a) 3.5μm, (c) 4.5-5μm, (e) 6μm and (g) 7μm and the corresponding ellipse based on the marked value at (b) 3.5μm, (d) 4.5-5μm, (f) 6μm and (h) 7μm.

In order to obtain the polarization conversion efficiency, the degree of the circular polarization (DOP) which represents the amount of circular polarization light in the detected beam is defined by:

$$p = \frac{I_c}{I_r} = \frac{S_3}{S_0}, 0 \leq p \leq 1 \tag{5.14}$$

where I_c stands for the amount of circular polarization light, I_r represents the power of reflected beam. From Figure 5.20, the DOP at 4.7μm is 0.6, at 6μm is 0.88, at 7μm is 0.7. The polarization conversion efficiency will be:

$$polarization\ conversion\ efficient = \frac{I_c}{I_s} = \frac{I_c}{I_r} \cdot \frac{I_r}{I_s} = p \cdot \frac{I_r}{I_s} \tag{5.15}$$

where I_s indicates the power of source corresponding to reflectivity from mirror. Figure 5.21 shows the measured $\frac{I_r}{I_s}$ as a function of wavelength in the range of 3.5μm to 10μm. Due to the existence of aluminium reflector, the reflectivity of metasurface is almost unity across the off-resonance region. Three data points at 4.7μm, 6μm and 7μm are highlighted to calculate polarization conversion efficiency of the metasurface based on equation *(5.15)* and the results are marked in green. At 4.7μm, the conversion efficient appears to be 0.58 lower than the rest. This is attributed to the low level of DOP (only 0.6). This could be due to that a tuneable quarter wave plate was used at this wavelength (supplied by ALPHALAS GmbH), which affected the alignment of the measurement system. At the other wavelengths, standard, fixed wavelength, quarter waveplates were used. In contrast, the conversion efficiencies at 6μm and 7μm were 0.83 and 0.65 respectively, closer to the expected values

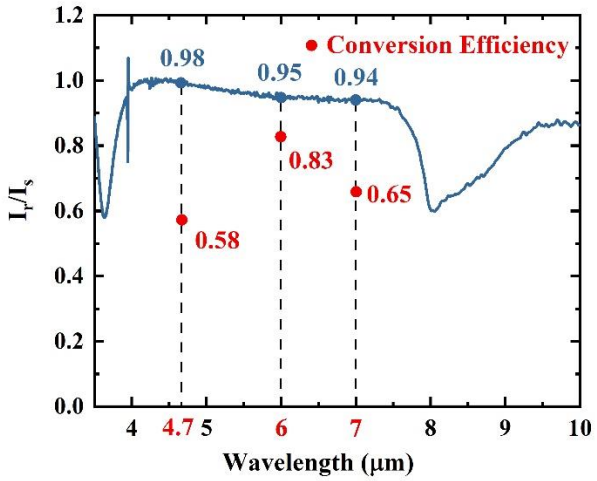

Figure 5.21 Reflectivity of metasurface and the calculated conversion efficiency.

Overall, the nanorod-based metasurface can provide linear-to-circular polarization conversion within around 4.7μm with average conversion efficiency of 58%. Broadly, this device can convert linearly to elliptically polarized light with axis ratio ranging from 0.4-0.65 across a broadband wavelength range from 4-7μm with polarization conversion efficient up to 0.83 at 6μm. This is contrast to a conventional quarter wave plate, based on birefringent material, which only provides polarization conversion at specific wavelengths. With the emerging demand of integration optical system, this metasurface with sub-wavelength thickness provide a promising design to replace conventional quarter wave plates.

5.5 Summary

In conclusion, we have designed, fabricated and characterised the optical properties of a nanorod-based metasurface in mid-infrared region. Experiments showed that fabricated metasurfaces enable to convert linearly- to circularly-polarized light within the off-resonance range from 4-7μm which are in good

agreement with the simulations. With recorded data, the polarization conversion efficiency can reach up to 0.83 at 6μm. Experimental results also show that special cases of oblique incidence will introduce an extra resonance at 5μm which narrows the effective operation wavelength range. Compared with conventional bulky quarter wave plates, which only provide polarization conversion at a specific wavelength, the metasurface provides a working bandwidth of 3μm, but with subwavelength thickness (~λ/4). Such metasurfaces could therefore become a promising candidate for replacing conventional optical quarter wave plates.

With the aim of exploring the use of these metasurfaces for the sensing of chiral molecules, in the next chapter, the near-field chirality characteristics of the achiral nanorod-based metasurface is explored.

6 Near-field chirality of a nanorod- based metasurface

6.1 Introduction

Substantial efforts have been devoted to develop chiral metamaterials with superchiral fields to allow detection and characterisation of chiral molecules. As summarised in section 2.4.3, chiral structures such as gammadion, double slit and double dimer have been experimentally demonstrated to provide measurable circular dichroism response to differentiate molecule enantiomers with high signal-to-noise ratio. However, a practical limitation of these approaches is the enhancement of circular dichroism relies on matching the structure resonance with the single molecule absorption band. Therefore a design strategy based on chiral structures can only be applicable at specific wavelengths, so can't provide molecular information at multi absorption bands. Results discussed in chapter 5 demonstrate that a metasurface based on nanorods can operate as a quarter waveplate across a broadband off-resonance. In this chapter we use simulations to determine whether a superchiral near field is excited in the metasurface across the same wavelength range, with the aim of assessing the potential use of the metasurface for broadband vibrational circular dichroism sensing in the mid-infrared region of the spectrum.

This chapter is organised as follows: first we demonstrate the findings of superchiral field generated on the surface of the nanorod-based metasurface, and plot the chirality as a function of wavelength under x-polarized excitation.

Then we compare the superchiral field distribution for x- and y-polarized light excitation and provide the far-field observation. Finally, to understand and effectively utilise the induced chirality, we analyse the behaviour as a function of incident polarization angles.

6.2 Chiral nearfields

6.2.1 Excitation with x-polarized light

We start by presenting the simulations of the nanorod-based metasurface discussed in Chapter 5 for x-polarized light excitation as depicted in Figure 6.1 (a). The simulated reflection spectrum can be seen in Figure 6.1 (b) where 3.42μm and 7.9μm are marked as the position of resonances. As shown in the previous chapter, under illumination with normal incidence light, it is proved that the reflected light will be converted into circularly polarized light across the 4μm to 7μm region.

Figure 6.1 (e) displays the strength of the optical chirality density $\hat{C}(\boldsymbol{r})$ (as defined in section 2.4.3), at a slice 5nm above the metasurface, for four different wavelength including two resonances at 3.5μm, 8μm, and two other wavelengths (5μm and 6μm) in off-resonance band. The $\pm$ sign refer to handedness of the superchiral field. A slice 5nm above metasurface was chosen because this is the point at which maximum optical chirality is observed. It is clear from these figures that superchiral fields are observed at all four different wavelengths, with the strongest chirality field localised asymmetrically at both sides of the nanorod in

each case. The maximum value of $\hat{C}(\boldsymbol{r})$ in the slice is plotted as a function of wavelength in Figure 6.1 (c). As might be expected, the superchiral enhancement is greatest at the resonances with enhancements of approximately 65 and 20 at 3.5μm and 7.9μm. The enhancement at off-resonances is lower, with values between -9 to 6, but still demonstrates the potential of this structure for the sensing of chiral molecules.

The simulations of the electric field profile on xy plane located 5nm above metasurface for the four different wavelengths are plotted in Figure 6.1 (f). It can be observed that the strongest enhancement of the electric field is at the resonances (3.5μm and 8μm), at which optical chirality density reaches maximum enhancement as shown in Figure 6.1 (e). As indicated from equation *(2.37)*, the effective enhancement of chiral fields are the consequence of the electric field enhancement. However, the spatial distributions of the electric field are different from the superchiral distributions, indicating that the generation of superchiral field arises from a complex interference between incident and scattered field rather a result of electric field alone [104].

It is also interesting to note that, from the colourmap in Figure 6.1 (e), we can observe a clear contrast between red and blue areas, which represents the sign of chirality $\hat{C}(\boldsymbol{r})$. This means that the chirality appears to be opposite handedness depending on its regions on the same slice. Therefore, we plot the sum of optical chirality as a function of wavelength in Figure 6.1 (d), which increases as a function of wavelength. Interestingly, it is observed to reach the maximum value in the off-resonance region from 4μm to 7μm. In contrast, the sum of the optical

chirality is only half or less than that for the resonance modes. It can be concluded that although the resonances lead to a strong superchiral field, they mostly cancel out due to the same amount field of opposite handedness leading to the vanishing of chirality when averaged over a unit cell. In the off-resonance region, however, the induced chiral field with one handedness is dominant, leading to significant overall chirality enhancement, holding promise to implement on chiral enantiomer sensing in a broadband wavelength range.

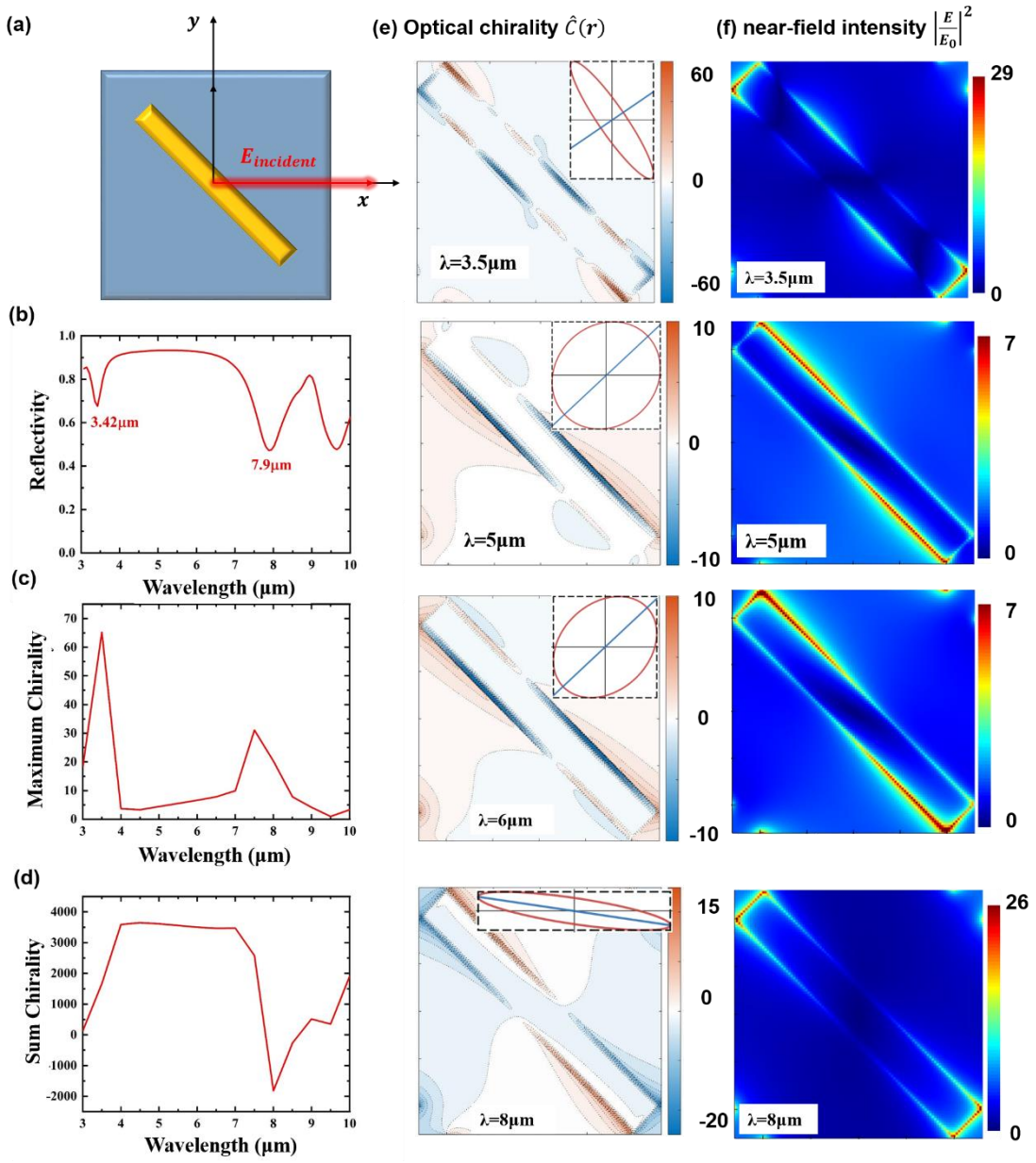

Figure 6.1 (a) Schematic diagram of a unit cell and incident light. (b) Simulated reflectivity as a function of wavelength. (c) Maximum and (d) Sum of optical chirality of the slice at 5nm above metasurface as a function of wavelength. (e) Optical chirality and (f) electric near-field intensity distribution computed at the slice 5nm above metasurface at four different wavelength.

This conclusion can be related to the metasurface far-field reflection discussed in chapter 6. From the insects in Figure 6.1 (e), we attached the polarization state of the beam at four different frequencies in far-field. It can be observed that at

same linear incident light excitation (x-polarized light), circularly polarized light can only be observed within the off-resonance region of the spectrum, while light still remains linearly polarized at the resonances. Therefore, the far-field polarization states are consistent with the sum of the computed near-field chirality.

6.2.2 Comparison between excitation of x- and y-polarized light

In far-field, the nanorod-based metasurface gives rise to circularly polarized light with its handedness sensitive to incident polarization angle. This is evidenced by the simulated results displayed in Figure 6.2. Under excitation of y-polarized light, the reflectivity for the two excitation polarizations is the same across the 4μm to 6.5μm region, whilst there is a difference of 0.5π in the phase as shown in Figure 6.2 (c) and (d). Figure 6.2 (d), indicating that reflected light becomes right-handed circularly polarized light under excitation with y-polarization. Bounded with the equivalent results for x-polarized excitation are plotted in Figure 5.2, it can be confirmed that the wavelength dependence of the reflectivity, phase and conversion efficiency are identical for the x- and y- polarized light excitation, except that the behaviour of the two orthogonal components of the electric field are reversed. This implies that the handedness of the reflected circularly polarized light can be switched most efficiently by simply rotating the metasurface by 90 degrees or rotate incident polarization by 90 degree just like a quarter wave plate.

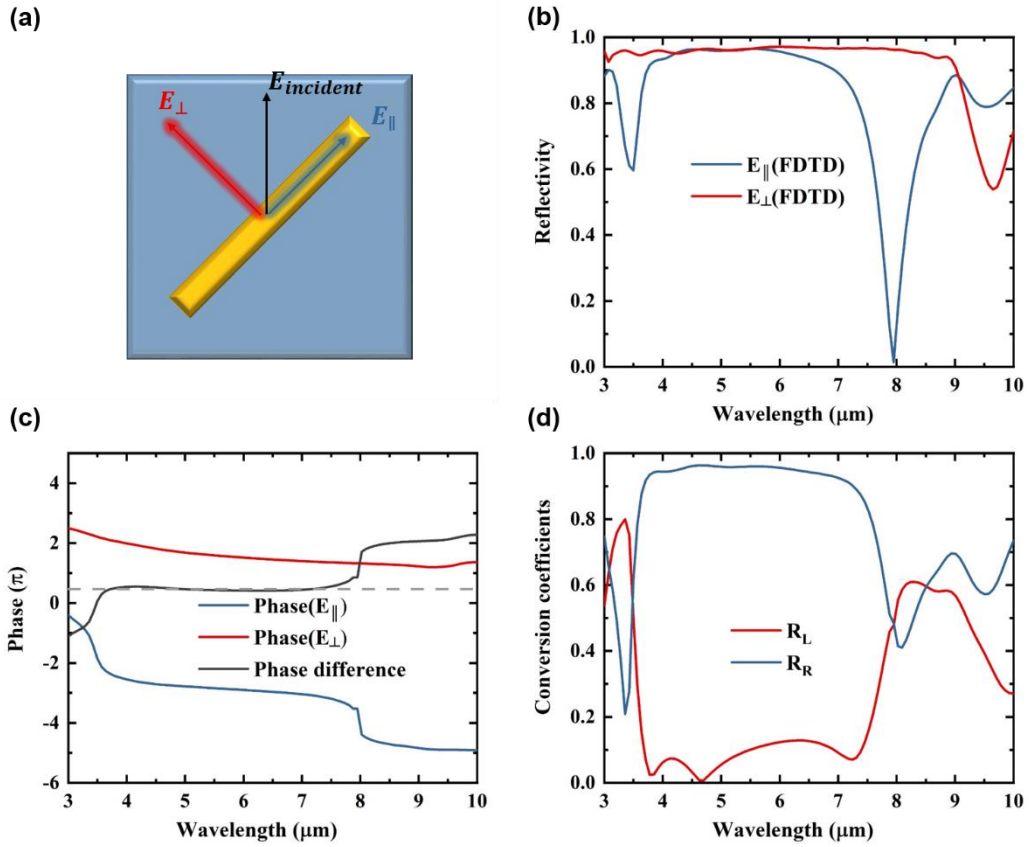

Figure 6.2 Simulation results of nanorod-based metasurface rotating 90 degree. (Equivalent data for excitation with original polarization is plotted in Figure 5.2)

To experimentally demonstrate these simulation findings, the Stokes parameters at 6μm were measured in the same way as for incident polarization along x axis, as described in chapter 5, and are shown in Figure 6.3 (a). S_1 and S_2 have similar values, close to zero, while S_3, which represents the amount of circularly polarized light, is close to -1. This shows that the reflected light is left-handed circularly polarized light and this is generated by metasurface for incident light along the x-axis. By contrast, when the metasurface is excited by linear light polarized along the y-axis (in the experiments, the metasurface was rotated by 90° as shown in insects whilst the incident polarization was kept the same), the handedness of circularly polarized light is expected to switch to right-handed. In

the measured Stokes parameters spectrum shown in Figure 6.3 (b), S_1 and S_2 still have values close to zero, whereas S_3 becomes close to 1. Therefore, the circularly polarized light is now right-handed, showing consistent with the simulation expectation. It can be concluded that the metasurface can generate circularly polarized light with customised handedness by controlling the polarization direction of incidence.

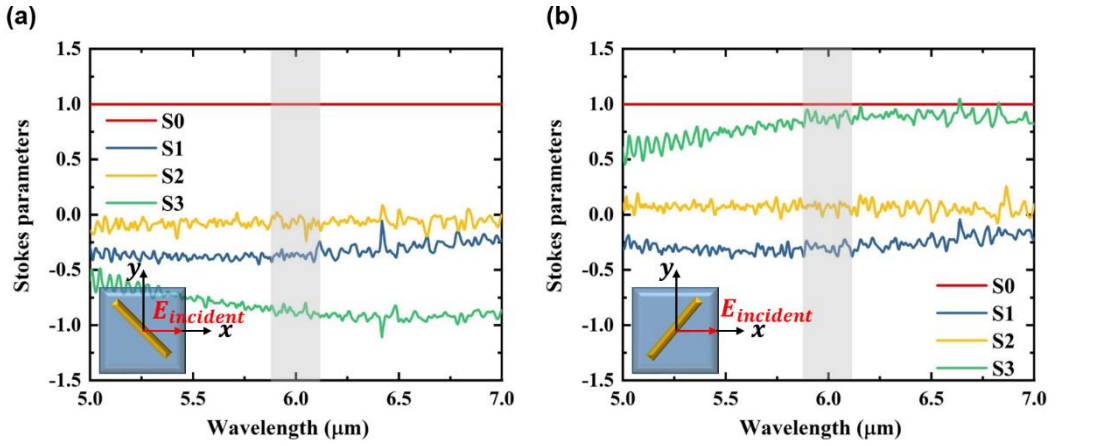

Figure 6.3 Measured Stokes parameters of metasurface for linearly polarized incident light along x- polarization. (a) Rod is at Ⅱ, Ⅳ quadrant. (b) Rod is at Ⅰ, Ⅲ quadrant.

Now we turn our attention to compare the spatial distribution of the optical chirality density $\hat{C}(\boldsymbol{r})$ in the near-field for incident polarization along x and y axis. Figure 6.4 (c) and (d) show the simulated optical chirality distribution under x and y-polarized excitation at three different wavelength namely: 3.5μm and 8μm which are resonances, and 6μm which is in the off-resonance region. From the optical chirality distribution, there are two clear findings. First, a distinct colour contrast can be seen along rod resonator, where the strongest superchiral field are confined. Second, it is obvious to see that a flip distribution map along resonator including colour switching were observed at all wavelengths for both x and y-

polarized excitation. This means that the superchiral field distribution has been flipped along the rod in terms of the size and the handedness. We plot the sum of computed optical chirality as a function of wavelength under the orthogonal excitation as shown in Figure 6.4 (b). The symmetric spectral response of $\hat{C}(\boldsymbol{r})$ over the wavelength range of interest indicates that an opposite sign of chirality are induced when the metasurface is illuminated with x- and y-polarized light. Different from the other two resonances, at 6μm, a clear contrast in the sign of $\hat{C}(\boldsymbol{r})$ can be seen in the region marked with dash triangle between rods. This can be treated as the dominant handedness of chirality in the slice as the sign of local chirality at each pixel is consistent with the sign of sum of chirality. Therefore, the handedness of superchiral field can be observed on a colourmap easily. However, at resonant wavelengths, the sum of chirality is relatively low due to the offset of opposite handedness, the sign of the entire slice is thus difficult to determine according the colourmap of the spatial distributions.

Although it is very difficult to experimentally characterise the near-field optical chirality, it is interesting to note that, in the far field, right-handed circularly polarized light was detected at this wavelength for excitation of x-polarized light which is the same handedness for the induced optical chirality in the near-field, and same principle can be applied for y-polarized excitation. To conclude, it is clear that the handedness from the near-field chirality is consistent with the far field projection. In the 4μm to 7μm region, where linearly polarized light is converted into circularly polarized light, strong super chiral near-field is excited with light twisted in the same direction as light in far-field.

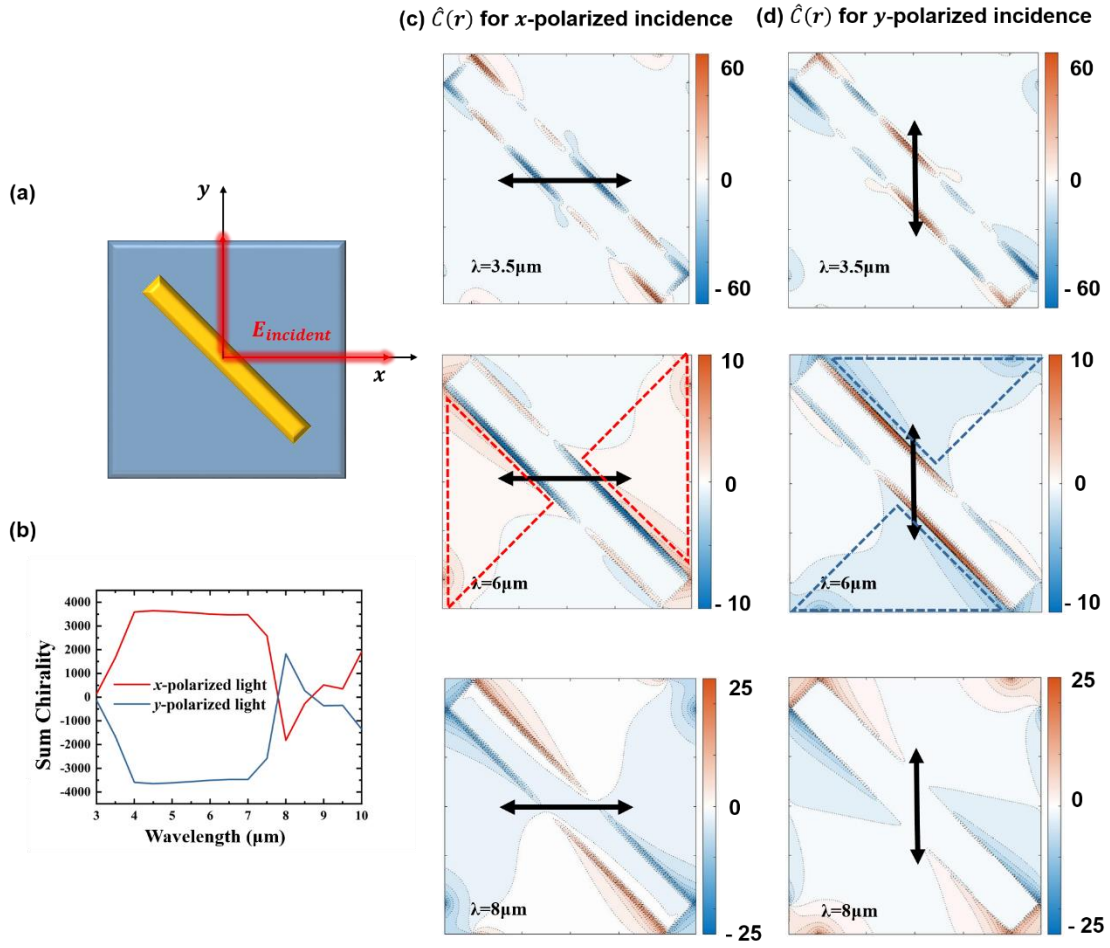

Figure 6.4 (a) Schematic diagram of a unit cell and incident light. (b) Simulated sum of optical chirality of the slice at 5nm above metasurface as a function of wavelength for x- and y-polarized incident light. Optical chirality distribution computed at the slice 5nm above metasurface at three different wavelengths for (c) x- and (d) y-polarized incident light.

6.2.3 Chirality with various incident polarization angle

As discussed, the handedness indicated from sum of optical chirality in the near-field shows strong dependence on incident polarization which also control the handedness of circularly polarized light in the far-field. To further explore the link between the near and far field optical chirality, we investigated the metasurface far-field polarization conversion performance and near-field superchiral distribution as a function of polarization angle.

First, in order to characterise the polarization states for far-field projection, the Stokes parameters of metasurface rotated at four different angles were measured for x-polarized incidence at 6μm and the results are presented in Figure 6.5, where the inset in each figure shows the diagram of a unit cell and x-polarized incidence. In Figure 6.5 (a) and (c), we have previously discussed these two case when the resonator is oriented at -45° or 45° with respect to the polarization direction of the linearly polarized excitation (x-polarized light in this case), where the detected beam can be identify as circularly polarized light with opposite handedness. As expected, we observed similar value of S_1 and S_2 but opposite sign of S_3 from results in Figure 6.5 (a) and (c). For measurements with the resonator oriented along, or orthogonal to incident x-poalrized light shown in Figure 6.5 (b) and (d), similar values of Stokes parameter are observed in both case, with S_1 close to 1 and S_2 and S_3 close to zero. This means that the detected light is linearly polarized along the x-axis, and the metasurface does not give polarization conversion in this case. In summary, the chirality in far-field shows strong dependence on excitation polarization.

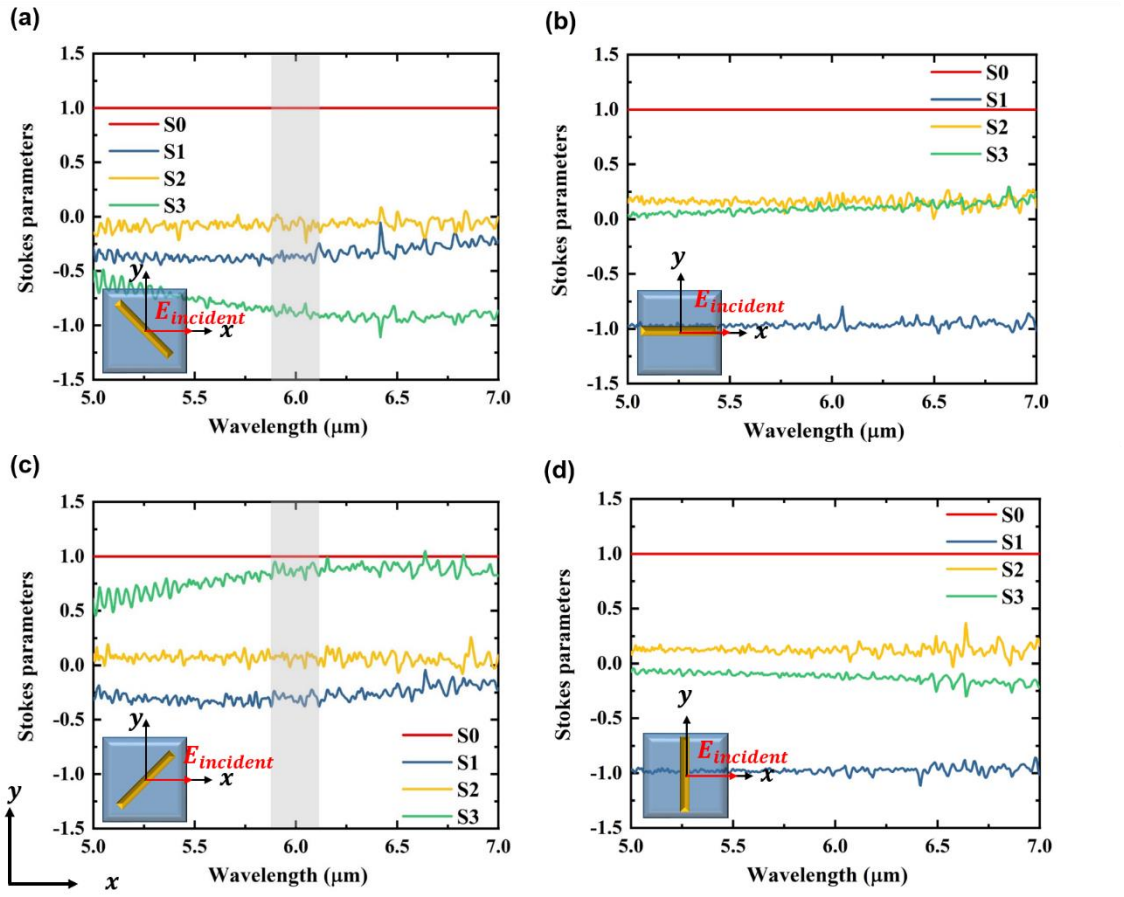

Figure 6.5 Measured Stokes parameters of metasurface at four different angle for x-polarized incident light

To go further, we investigate the superchiral near-field as a function of polarization angle. The simulation results for five different incident polarization angle ϕ (45°, 67.5°, 90°, 112.5° and 135°) are shown in Figure 6.6. These angles are selected from 45° to 135°, with an increment of 22.5°, to cover the cases when the rod resonator is excited by orthogonal light, parallel light, and in-between. Figure 6.6 (a) displays the schematic diagram of the unit cell versus five different polarization angle ϕ. First, since the superchiral field is non-uniformly distributed with opposite handedness, we plot the value of strongest chirality field as a function of wavelength in Figure 6.6 (b). When the metasurface is

illuminated with linearly polarized light where the electric field vector is orthogonal to the rod (polarization angle is 45°), there is negligible chirality field generated across the entire wavelength range. As the polarization angle increases to 135°, the maximum value of induced optical chirality also increases until the incident light become parallel to rod, where the strongest induced chirality field is observed.

In order to understand the insight physical principle behind the generated superchiral field, Figure 6.6 (c) displays the superchiral field distribution at 6μm under increasing polarization angle. Starting from the smallest angle (45°), it is obvious that there is almost no superchiral field being generated. In this case, the incident light is polarized along the direction that is orthogonal to the resonator, resulting in weak interaction with rod resonator. There is thus no electric field enhancement in the vicinity of the metasurface. As a consequence there is no strong near-field contribution to generate chirality. When the polarization angle increases, the induced superchiral field become more and more intense and reaches tomaximum at 135°. This phenomena can be understood by the Hertzian dipole mode discussed in [104], where the rod resonator is treated as an electric diploe and the induced chirality arises from the interaction between the magnetic field of the incident light and the scattered electric field. When incident light polarization exhibit an arbitrary angle to dipole axis, the induced superchiral field is then directly linked to the components of those two that is parallel to dipole. When incident light polarization is parallel to the dipole, the induced superchiral field is determined by components of those that is orthogonal to dipole. As the

magnetic field of the incident light is always orthogonal to the dipole, the maximum chirality is induced when the incident light is polarized parallel to the resonator.

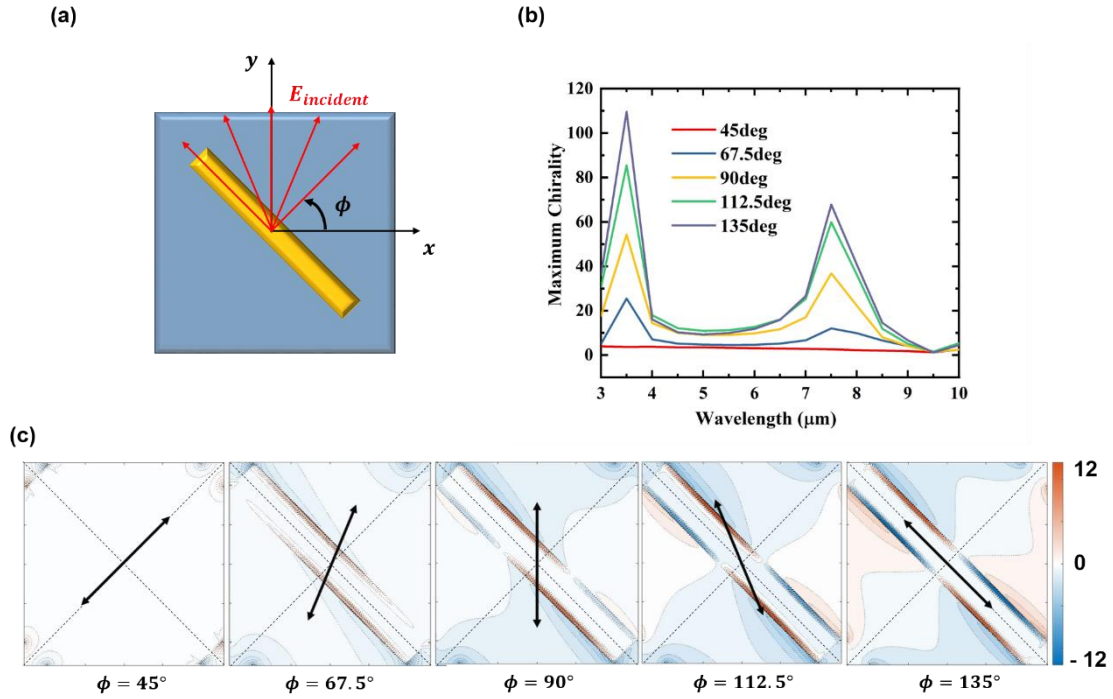

Figure 6.6 (a) Schematic diagram of unit cell and five different polarization angle (b) Maximum of optical chirality of the slice at 5nm above metasurface for five different polarization angle as a function of wavelength. (c) Optical chirality distribution computed at the slice 5nm above metasurface at 6μm for five different polarization angles.

Although the strongest superchiral field is induced when incident light is polarized along the resonator, due to the geometric symmetry, equal amounts of chirality with opposite handedness are also induced, as shown in the chirality distribution in Figure 6.6 (c). As a consequence, the sum of chirality approaches zero, potentially making the metasurface not suitable molecular sensing. In Figure 6.7 (a), we plot the spectrum of the sum of chirality for five different polarization angles. As expected, the sum of chirality become zero when light is either parallel

or orthogonal to the rod. On the contrary, the absolute chirality exhibits maximum value when incident light is at 90 degrees. Figure 6.7 (b) gives the sum of chirality at 6μm as a function of incident polarization angle, which clearly shows that the sum of chirality is polarization-dependent. Therefore, the generation of optical chirality is linked to the absence of symmetry between the excitation polarization and metasurface resonators.

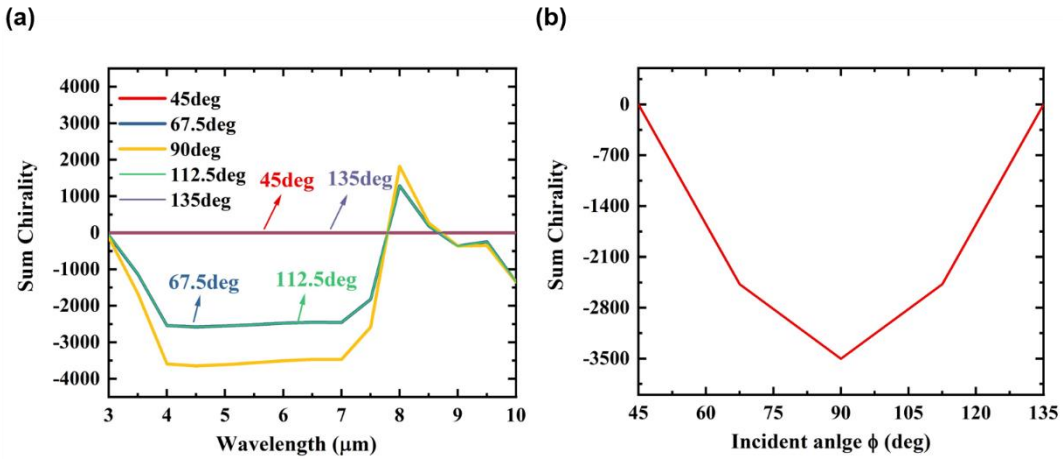

Figure 6.7 (a) Computed absolute chirality as a function of wavelength for five different polarization excitation. (b) The absolute chirality at 6μm as a function of excitation polarization angle.

6.3 Summary

In summary, we numerically modelled the near-field chirality of a nanorod-based metasurface. The simulation results show that a superchiral near-field can be generated under linear polarization excitation, when the polarization angle is 45 degrees to the rod resonator. The same superchiral field can be generated, but with opposite handedness, when the polarization angle is rotated by 90 degrees. Thus, the nanorod-based metasurface can be exploited to enhance chiroptical

effect for enantiomer sensing based on circular dichroism spectroscopy. We also investigate the induced chirality in the near-field as a function of polarization angle. Bounded with the chirality measured in far-field, we conclude that the absolute chirality in near-field exhibit consistence with that in far-field.

Based on the theoretical analysis above, in the next chapter, we will provide an enantiomeric selection measurement to conduct circular dichroism spectroscopy using the nanorod-based metasurface.

7 Molecular enantiomer differentiation using a nanorod-based metasurface

7.1 Introduction

Molecular enantiomers, which include many important biomolecules, are made up of identical atomic elements, but have a chiral arrangement of the molecular components which may lead to distinct chemical and physical properties. Because enantiomers vary in the stereogenic context to their structure, they interact with circularly polarized light differently. Circular dichroism spectroscopy, measures the different absorption for left- and right-handed circularly polarized light, is a core technique to identify different molecular enantiomers. However, the weak interaction between molecules and light means that it is challenging to resolve molecular information due to a relatively low signal-to-noise ratio.

The advent of nanophotonics, which enable the concentration of the electromagnetic field, has paved the wave for significant research on fast and high-sensitivity biosensing on nanoscale for small molecules. By optimising the shape and size of the resonating structure to match corresponding operation wavelength, signal enhancement with few orders of magnitude has been demonstrate in fluorescence, surface enhanced Raman scattering in the visible spectrum, and surface enhance infrared absorption in the mid-infrared region. Due to the existence of molecular vibrational fingerprints in the mid-infrared

spectrum, surface enhance infrared absorption is particularly powerful for resolving molecular functional groups without labelling requirement.

An enhanced circular dichroism response has been demonstrated with various chiral nanostructure due to the capability of inducing a high degree of superchiral fields which is suggest to enhance enantiomeric selective absorption. Based on the near-field chirality analysis in chapter 6, we numerically showed that the nanorod-based metasurface possess unique ability of creating strong superchiral field under linear polarization excitation in a broadband mid-infrared spectrum. In comparison to conventional circular dichroism spectroscopy based on chiral nanostructures, which enhances the potential response by matching the plasmonic resonance with the vibrational absorption of the molecules, the nanorod-based structure explored in this work as two main potential advantage: 1), the metasurface can create superchiral field across a broadband mid-infrared range from 4-7μm and can thus provide molecular information at multiple bands. 2), conventional circular dichroism spectroscopy requires fabrication of both left- and right-handed metasurfaces to selectively interact with enantiomers. For our structure, the opposite handedness of chiral field can be generated by simply rotating either the metasurface or incident polarization, by 90 degree.

Motivated by these numerical results, we proposed the measurement scheme as follow to measure enhancement of circular dichroism response of the amino acid alanine enantiomers on nanorod-based metasurface.

7.2 Sample preparation

Our enantiomers of choice is L-alanine and D-alanine, suspended in paraffin oil. Chiral enantiomers and paraffin oil were purchased from Sigma-Aldrich. As both L-alanine and D-alanine are supplied in crystalline form, the sample preparation is designed to mix the molecules and paraffin oil well so that the alanine is evenly distributed on the metasurface. Figure 7.1 display the sample preparation process. It starts from thoroughly grinding alanine powder in a mortar with a pestle. The powder (0.05 gram in this experiment) is then added into 1.5ml reaction tube, where the desired volume of paraffin oil is added. In order to evenly disperse alanine powder in paraffin oil, the reaction tube are placed into a sonicator for about 5 minute until the liquid become completely cloudy, with no large big particles seen. After mixing, the liquid sample is drop cast onto a substrate with a pipette. Finally, an IR polished calcium fluoride optical window (10mmx0.35mm) was added on top of the mixture layer, to both reduce the sample thickness and to make sure that this thickness is the same across the device. Measurements on the metasurface were conducted separately with the enantiomers in the order as: L-alanine, clean, R-alanine, clean. After each measurement, the metasurface was soaked and rinsed with acetone then Isopropyl alcohol to remove any residues and contamination from previous measurement on surface. Once the measurement were finished, the metasurface were cleaned and reused for the next measurement.

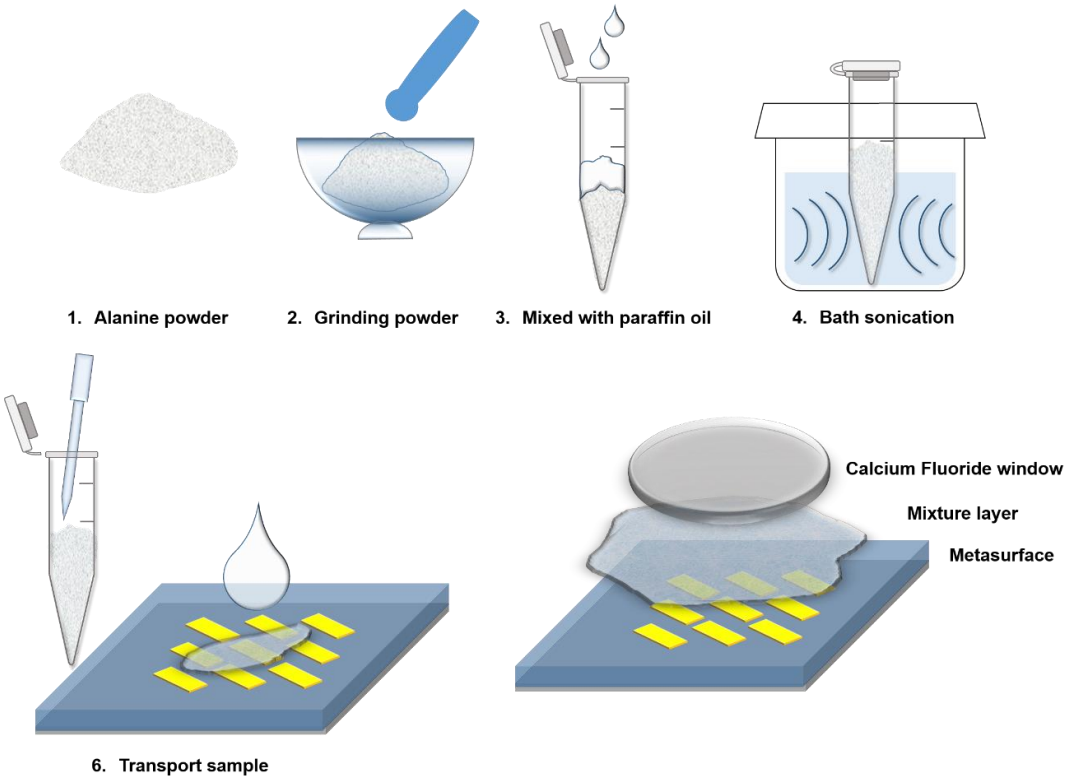

Figure 7.1 Schematic diagram of sample preparation process.

7.2 Transmission Measurements

Before characterization of the circular dichroism response using the metasurface, the transmission spectrum of the D-alanine and paraffin oil suspension was measured with a FTIR spectrometer from 4000 to 1000 cm^{-1} to identify the functional groups (the same spectrum was observed for L-alanine). In this case, the molecular sample was drop cast onto a transparent calcium fluoride window, and the transmission was measured in the FTIR chamber in vacuum to reduce the effects of atmospheric transmission. Same measurement was conduct for pure paraffin oil. In order to better visualise the molecular absorption, the obtained raw data for paraffin oil was normalised by the transmission of calcium fluoride

window only and the data for molecular sample is normalised by the transmission of pure paraffin oil. The normalised transmission spectrum for paraffin oil and D-alanine are plotted in Figure 7.2 (a) where the inset shows the chemical structure of D-alanine. The marked red area at 2958cm^{-1}, 1459cm^{-1} and 1376cm^{-1} respectively are the overlapping bands where both paraffin oil and alanine contribute to the vibrational absorption. For alanine, there is a strong and sharp vibrational absorption that can be detected for C-H asymmetric stretching at 2958 cm^{-1}. The minima at 2112 cm^{-1} marked with blue area represents the asymmetrical bending vibration of NH_3^+. The absorption band at 1621 cm^{-1} is due to the contribution from C=O stretching, and is used in conventional circular dichroism spectroscopy. The minima at 1453 cm^{-1} is related to CH_3 bending modes [105], [106]. Considering that metasurface excites strong and consistent superchiral field in the spectrum from 4-7μm, we selected the region of 2500-1400cm^{-1}, which includes the 2111cm^{-1} and 1621cm^{-1}, absorption fingerprints only from alanine to characterising circular dichroism spectroscopy for alanine without interference from the paraffin oil.

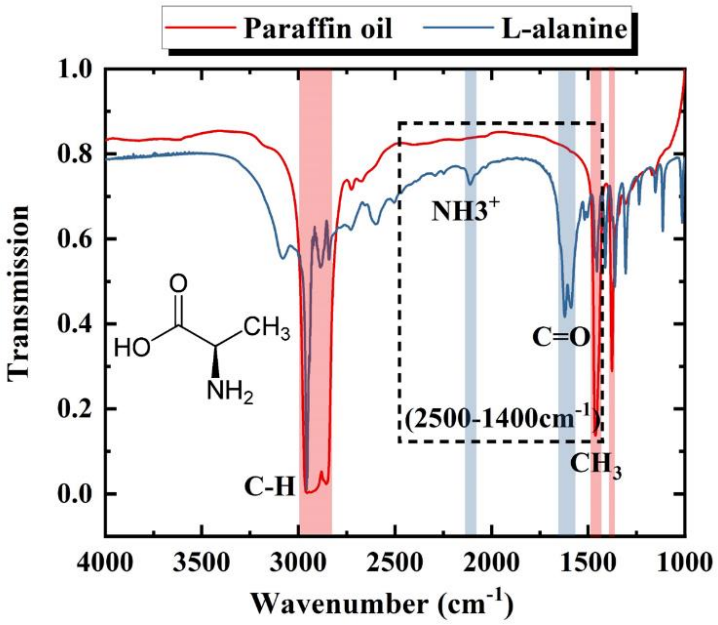

Figure 7.2 Transmission spectrum of paraffin oil and L-alanine at 4000-1000cm^{-1}.

7.3 Vibrational circular dichroism spectroscopy

Infrared reflection spectra were measured with FTIR spectrometer from Bruker Vertex 80v with a self-built reflection measurement system as shown in Figure 7.3 (a) (details of the measurement system can be found in section 4.3.5). The size of the source aperture was set to 8mm to match the size of the resonator array (8mmx8mm in the centre of a 10x10mm chip) in order to collect as much signal as possible. A holographic wire grid polarizer from Thorlabs (transparent from 2 to 30μm) was used to generate horizontally polarized light guided to the metasurface. To excite circularly polarized light, the metasurface sample (mounted on a rotation stage) was initially positioned with the rod resonators oriented at 45 degrees to the incident polarization at Ⅱ, Ⅳ quadrant. In this case, we marked this position as 0 degree as shown in Figure 7.3 (b). In order to switch

the handedness of induced superchiral field, the metasurface sample was rotated by 90 degrees, therefore, the position was marked as 90 degree. Measurements were conducted in the off-resonance region which corresponds to spectrum of 1400-2500 cm^{-1}, where the superchiral field were generated. For a final measurement spectrum, a total of 1120 scans (taking an hour) were averaged with 1cm^{-1} spectral resolution.

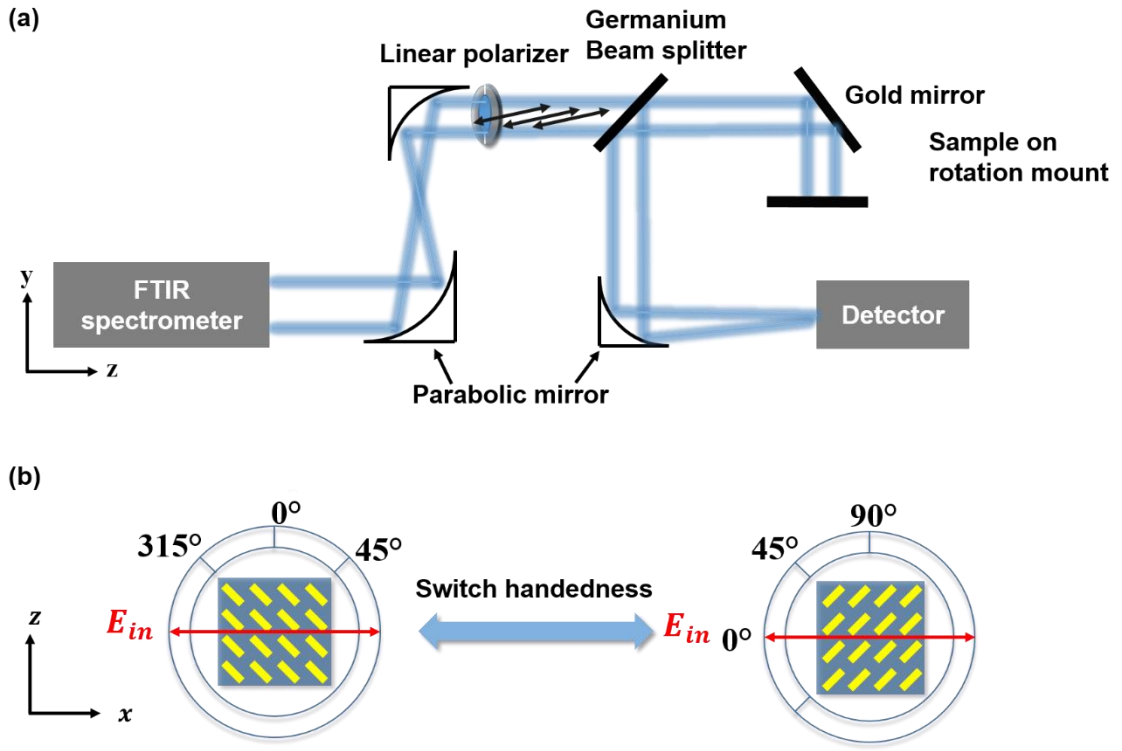

Figure 7.3 (a) Schematic diagram of FTIR-based reflection measurement setup. (b) Schematic diagram to show the orientation of rod resonator with incident polarization. Sample is mounted on a rotation mount labelled with dials to show the degree of rotation. Simply rotate 90 degree to switch the handedness of metasurface.

7.4 Results and Discussion

7.4.1 Effect of molecular concentration

The concentration of molecules in the paraffin oil suspension can affect the quality of the vibrational circular dichroism. A higher concentration lead to stronger absorption features. However, there is an upper limit beyond which increasing concentration may result in situation where there is not enough signal at the minima of the molecular resonance to be able to accurately measure the circular dichroism. To identify the optimum concentration, we performed reflection measurements using the metasurface with three different concentration of D-alanine in paraffin oil: 0mol/L, 0.05mol/L and 0.2mol/L. In this experiment, the liquid mixture with different concentration were prepared independently in advance. After drop casting the suspension on top of the metausrface, the reflectance spectra were measured with metasurface being rotated at 0° (to excite a left-handed superchiral field) recorded as R(0°), and 90° degree (excite right-handed superchiral field) recorded as R(90°). Note that the experiments were conducted in ambient conditions in air, and raw spectra contain rapidly varying atmospheric absorption bands. A Savitzky-Golay filter method was applied to the raw data to remove the effects of atmospheric absorption, whilst allowing the absorption bands from molecules of interest to be more clearly seen. In order to keep variables on similar scale between measurements, the measured raw data R(0°) or R(90°) are then normalised by the data obtained without molecules (pure paraffin oil on metasurface)and recorded as $R_n(0°)$ or $R_n(90°)$.

The circular dichroism response is characterised by the ratio between two reflectance: $R_n(0°)/R_n(90°)$ for each concentration to better visualise the differential absorption.

The reflectance spectra (smoothed raw data) for three different concentration of D-alanine are shown in Figure 7.4 (a). In Figure 7.4 (a), for the metasurface coated with pure paraffin oil, two very strong absorption bands: 2350cm^{-1} (CO_2) and 1460cm^{-1} (Paraffin oil) are observed, with the features in the range from 2000cm^{-1} to 1400cm^{-1} due to atmospheric water. For the case of paraffin oil only, the spectra measured at 0° and 90° should be identical, and the small deviations between the two measured spectra are likely to be due to alignment issues. When the concentration was increased to 0.05mol/L, the existence of alanine results in a decrease in reflectance. Two strong absorption bands at 2110cm^{-1} and 1600cm^{-1} associated with alanine appears. As the concentration increased further to 0.2mol/L, the absorption will become stronger, with the reflectance amplitude being reduced further across the entire spectrum as shown in Figure 7.4 (a). The absorption fingerprint caused by the alanine becomes more significant than that for less concentration, especially at 1600cm^{-1} where the reflectance amplitude was reduced to zero. Because the entire signal was absorbed by alanine, the differential interaction between alanine with opposite superchial field become negligible which is challenging to measure. As a result, a concentration of 0.05mol/L is better to undertake circular dichroism spectroscopy as it provides clear and distinguishable absorption fingerprints with measureable signal.

To confirm that 0.05mol/L is the sufficient level of concentration to carry out circular dichroism spectroscopy, in Figure 7.4 (b) circular dichroism response $R_n(0°)/R_n(90°)$ for three different concentration is plotted. With just paraffin oil, the ratio is largely independent of wavelength, with an average value of 1.05. This confirms that that the paraffin oil interacts with the two different hands of the circularly polarised light equally, as expected. In contrast to paraffin oil, it is interesting to observe that features emerge in the plotted ratio as the alanine concentrations increase. However, for 0.2mol/L, it can be observed that significant light absorption occurs, resulting in zero reflectance at 1600cm^{-1}. This doesn't allow the difference in absorption for left- and right-handed superchiral fields to be distinguished. For a concentration of 0.05mol/L, the ratio appears is relatively independent of wavelength, with clear features at 2110cm^{-1} and 1600cm^{-1} associated with the alanine. This demonstrates the feasibility of using the metasurface for enhanced vibrational circular dichroism.

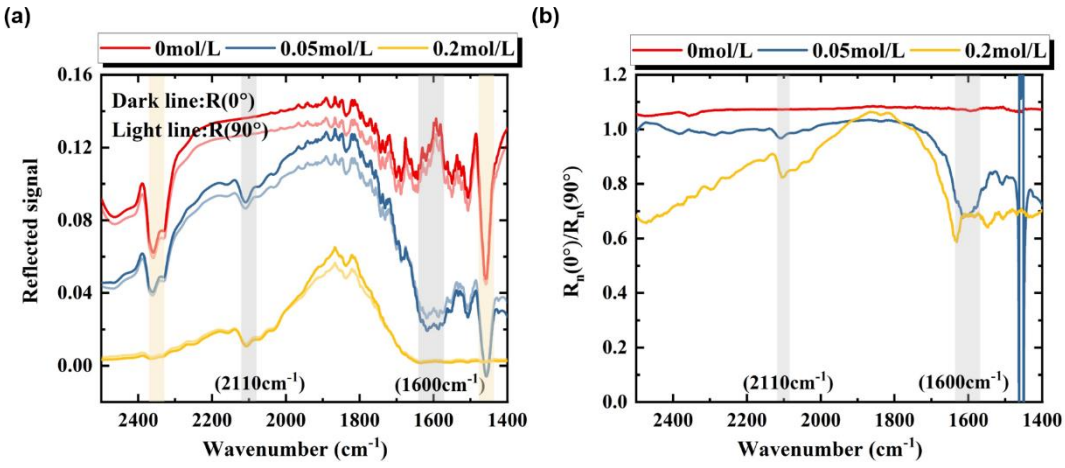

Figure 7.4 (a) Smoothed reflectance spectrum for sample with three different concentration: 0mol/L, 0.05mol/L and 0.2mol/L. the dark (light) line represent the spectrum measured when metasurface is at 0 (90) degree. (b) The calculated $R_n(0°)/R_n(90°)$ as a function of wavenumber for three different concentrations.

7.4.2 Enhancement infrared absorption based on metasurface

In order to investigate the metasurface's ability to enhance the infrared absorption by molecules, reflectance spectra for a metasurface and substrate (SiO_2/Al/Si without resonators), rotated at 0 and 90 degrees, were conducted. In this experiment, the concentration of 0.05mol/L for D-alanine was selected. Figure 7.5 show the $R_n(0°)/R_n(90°)$ for substrate and metasurface as a function of wavenumber. For substrate, the value of the ratio across most of the spectrum is 1, indicating that the molecule interacts with light equality as there is no chirality being generated without resonator in near-field. However, there are three absorption bands (2359cm^{-1}, 2112cm^{-1} and 1600cm^{-1}), marked in the grey area, where the shifts slightly away from 1. This means that there are signal changes after the substrate being rotated by 90 degrees. The main reason behind this unexpected difference can be attributed to alignment issues in the measurement system: 1), as the substrate was rotated by 90 degree, the incident light may interact with a different amount of paraffin oil and molecules, which could then lead to a difference in reflectance. 2), the rotation of substrate could cause changes in light scattering, reflection and absorption.

A similar result was observed for the measured $R_n(0°)/R_n(90°)$ produced by metasurface, where the value of the ratio is approximately 1 over most of the spectrum. However, for the metasurface only alanine vibrational absorption bands, namely: 2112cm^{-1} and 1600cm^{-1} are visible as minima, with their size being much greater than equivalent result from substrate. Despite the potential

optical alignment issue, this distinct behaviour is sufficient to prove that the chiral near-field of the metasurface has enhanced the interaction with the molecules.

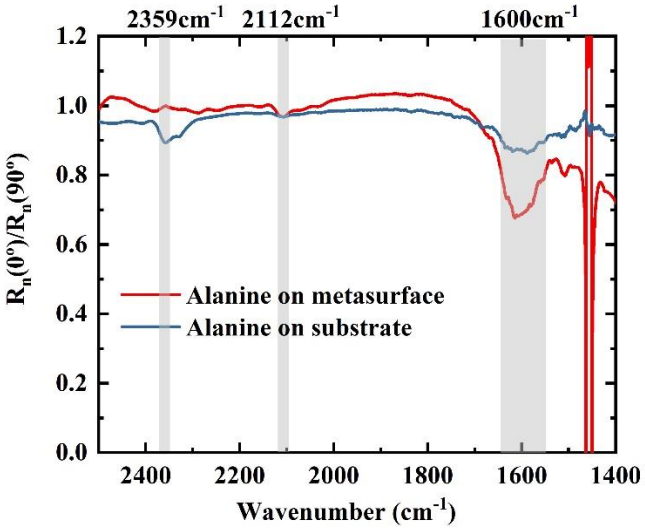

Figure 7.5 The calculated $R_n(0°)/R_n(90°)$ as a function of wavenumber for metasurface and substrate.

7.4.3 Vibrational circular dichroism

The near-field analysis in chapter 6 showed that superchiral field with opposite handedness is expected to generate when the metasurface is orientated at 0° or 90. Therefore the ratio of $R_n(0°)/R_n(90°)$ for D- and L-alanine should be the complement of each other (i.e.in one case lying above 1, in the other lying below 1). However the calculated $R_n(0°)/R_n(90°)$ for D-, L-alanine and paraffin oil on the metasurface, in Figure 7.6, shows that the results are very similar for both molecules, in contrast to the expectations from the near-field analysis. The absence of a circular dichroism response raises questions regarding the alignment of the reflection measurement system. The vibrational circular

dichroism signal for enantiomers are typically weak compared to electric transitions, and their characterization requires highly sensitivity instruments to detect weak signal from molecules, and a robust measurement system to reduce any influence from other variables and making it easier to compare and analyse signals from different enantiomers. In this experiment, several challenges are presented regarding keeping variables constant between measurements: 1), the experiment is conducted in air, thus the absorption from atmospheric gases, particularly water vapour and carbon dioxide, could cause unpredictable absorptions and scattering affecting the chiroptical response. 2), Precise alignment of optical components is a challenge in the mid-IR region due to the higher likelihood of beam divergence and diffraction effects. 3) By manually rotating the metasurface, extra variables could have introduced more variables 4), paraffin oil cannot dissolve alanine particles, so a suspension I formed, and it is therefore hard to ensure even distribution of molecules across the metasurface. Further work is needed to optimise the measurement system to enable the demonstration of enhanced circular dichroism.

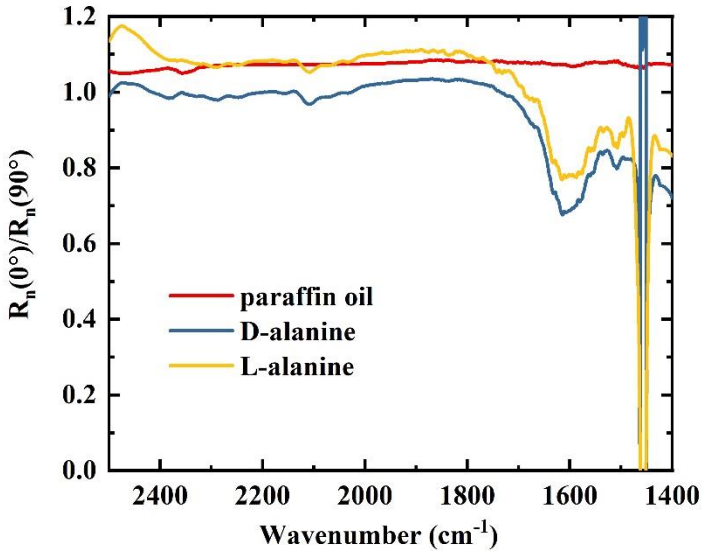

Figure 7.6 The calculated $R_n(0°)/R_n(90°)$ as a function of wavenumber for metasurface

7.5 Summary

With the aim of validating the near-field analysis of the nanorod-based metasurface, and the potential use of the metasurface for chiral enantiomer sensing, a comprehensive experiment was conducted to assess the capability of this achiral metasurface to enhance chiroptical effect with chiral molecules. The nanorod-based metasurface generates superchiral field under linear excitation, and the handedness of the chiral field can be switched by simply rotating metasurface by 90 degrees. In contrast to conventional circular dichroism spectroscopy which measures the differential absorption for left- and right-handed circularly polarized light, this experiment aim to observe significant reflectance difference with the metasurface orientated at 0° and 90° to characterise the circular dichroism response. First, we identified two distinct

absorption bands at 2112cm^{-1} and 1621cm^{-1} originating from the chiral molecule from alanine in the measured transmission spectrum. Next, we investigated molecule concentration effects on circular dichroism, with the measurement results showing that 0.05mol/L is the ideal level of concentration which provide distinguishable absorption feature associate with alanine. With reference to measurements using the substrate only, measurements also showed that the metasurface produces strong near field that significantly enhance molecular interaction. Although it wasn't possible to observe an enhance circular dichroism response, we believe that this is dues to the limitations of the measurement system, and the results presented represent an important step towards using an achiral metasurface structure for the sensing of chiral molecules.

8 Conclusions and outlook

8.1 Conclusions

8.1.1 Broadband efficient mid-infrared linear-to-circular polarization conversion using a nanorod-based metasurface

A nanorod-based metasurface was designed, fabricated and characterised to conduct efficient broadband linear-to-circular polarization conversion in the mid-infrared region of spectrum. The anisotropic property of metasurface is investigated by decomposing linear incidence into two orthogonal polarizations with one along the rod, the other one perpendicular to the rod. Simulations showed two well separated resonances at 3.4μm and 7.9μm are excited in the reflection spectrum, and in the wavelength between these resonances orthogonal components have almost equal amplitude and 90 degree phase shift, allows reflected light be converted into circular polarization light. The properties of two resonances that introduce phase shift are investigated with metasurface geometries and the underlying mechanism are analysed by inspection of the near-field distributions and the properties of Fabry-Perot cavity-like modes. Simulation results validate that 3.4μm is originated from a gap-plasmon mode, whilst the resonance at 7.9μm is due to Fabry-Perot cavity-like mode. An investigation of the performance of metasurface at oblique incidence showed that

a further Fabry-Perot mode can be induced, so that normal incidence illumination for the metasurface is important in maintaining broadband operation wavelength. Stokes parameters within the off-resonance wavelength range were measured to extract the actual polarization properties of the reflected beam. Results showed that light had been converted into circular polarization from 4-7μm, with efficiency up to 0.83, showing consistency with simulations. This metasurface with subwavelength thickness demonstrates potential as alternative optical element for conventional quarter wave plates.

8.1.2 Near-field chirality of a nanorod- based metasurface

With aim of practical application of chiral sensing, the near-field chirality of the nanorod-based metasurface was investigated, and we showed that under illumination, the strong superchiral field is induced, which holds promise for chiral enantiomer sensing. The simulation results showed that the superchiral field is distributed non-uniformly on the metasurface, with opposite handedness. The maximum enhancement (29 and 26 times increase) was founded at the resonances of 3.4μm and 7.9μm due to enhancement of electric field, but a lower enhancement was seen in the wavelength region between resonances. However, the absolute chirality, which is the sum of the fields across the unit cell of the metasurface, and which characterise the strength of interaction with an analyte, showed opposite behaviour. The absolute chirality diminished at the resonances, but exhibit maximum value within broadband off-resonance range, offering potential for chiral enantiomers sensing. In addition, by simply switching the

excitation polarization, we demonstrate that the absolute chirality can switch its handedness which indicates that the absolute chirality is polarization dependent. In experiment, we measured the handedness of chirality in far-field, showing that switching the excitation polarization switches the handedness, as with the near-field chirality. Solid evidence of the polarization dependence of the near field chirality, and similar behaviour for far-field chirality was found by investigating the absolute chirality as a function of incident polarization. Results shows that maximum absolute chirality can be obtained when light is polarized along axis at 45 degrees with respect to the rod, and it is zero when light is polarized along/orthogonal to rod. Measurements results also prove similar behaviour in far-field.

8.1.3 Molecular enantiomer differentiation using a nanorod-based metasurface

An enantiomeric selective experiment scheme based on vibrational circular dichroism spectroscopy was conducted with nanorod-based metasurface. For this experiment, the tested substance was a suspension of the amino acid alanine (L- or D-alanine) in paraffin oil.

First, we recognised two distinct absorption bands at 2112cm^{-1} and 1621cm^{-1} originating from the chiral molecule alanine in the measured transmission spectrum. Next, we investigated molecule concentration effects on circular dichroism, with the measurement results showing that 0.05mol/L is the ideal level of concentration which provide distinguishable absorption feature associate with

alanine meanwhile higher concentration lead to stronger absorption result in diminishing reflectance. With reference to measurements using the substrate, measurements also showed it is validated that the metasurface is capable of producing strong near fields that significantly enhance molecular interaction. Although it wasn't possible to observe an enhanced circular dichroism response, we believe that this is due to the limitations of the measurement system, and the results presented represent an important step towards using here open possibility of chiral sensing on an achiral metasurface structure for the sensing of chiral molecules.

8.2 Outlook

8.2.1 Polarization conversion

Due to the invisibility of mid-infrared light, the most challenging thing in the experiments is to align measurement system, making sure that the beam properly illuminates the sample. The alignment also needs to be maintained between measurements to ensure the reproducibility of results. This adds up more challenges as introducing the sample could potentially change the alignment of the reflection system, thus introducing instability in the final results. For example, the measured Stokes parameters at 4.5-5μm in Figure 5.20 (c) are very noisy, even though the feature can stand up after smoothing data, the measured third Stokes parameters is at value of 0.59 which is a deviation from the theoretical expectation. As the third Stokes parameter was measured with a tunable quarter-wave plate, and its tunability is accomplished through tilted the bulky window at

certain angle, this also affecting the alignment and introduced more errors into results. The use of identical quarter wave plates at each measurement wavelength would provide improved reproducibility of the measurements.

8.2.2 Relationship between near-field and far-field chirality

In most published research, the superchiral field are induced and enhanced by chiral plasmonic nanostructures such as, double slits [29], [80], hierarchical structure [73], gammadion arrays [71], [107] and nanorod dimer[72], [108] because of the geometric chirality. Excitation of circular polarization of light introduces intrinsic chirality in the system, with the confinement of local electromagnetic field, the induced superchiral field can increase by a few orders of magnitude compared to a substrate. In 2012, Martin [104] from University of Stuttgart numerically calculated optical chiral density in near-field of achiral structure under achiral light and showed that superchiral field can be produced even in a symmetric environment. Following this pioneering work, the subsequent development of achiral structures shows enhanced superchiral field under excitation of achiral light, including examples from dielectric slab [109], gold nanodisks [110], nanorod [111], elliptical nanohole [112] and the nanorod-based metasurface studied in the thesis. It should be emphasized that in this case, the absolute chirality could be offset to zero thus making no contribution to chiroptical effect. The use of an achiral structure can causes a more complicated chiroptical effect. Further work is needed to understand the mechanism of the circular

dichroism response, and the relationship between the near-field and far-field chirality.

8.2.3 Optimised design to generate stronger super-chiral field

As demonstrated in Chapter 6 and other examples of achiral metasurface [28], [110], [111], [113], it is confirmed that geometric chirality is not a necessary prerequisite to produce superchiral fields to enhance the chiroptical response. However, there has been much less focus on achiral metasurfaces compared to chiral structure, which have been widely investigated for enantiomeric selective sensing due to their intrinsic chiroptical response. Although there is a profound capability for tailoring the superchiral fields obtained from a chiral structure, in the scenario of practical application such as: enantiomeric sensing, a chiral structure geometric-based approach has four drawback: 1), due to the offset from opposite handedness, the non-uniform distribution of superchiral field diminishing the overall impact on chiral molecule. 2), the superchiral field excitation relies on the resonances of the nanostructures used, therefore limiting the effective working bandwidth. 3), circular polarization excitation is required.4), a pair of structures for opposite handedness has to be fabricated. As demonstrated in Chapter 6, an optimised achiral structure hold promise for overcoming these drawbacks, with the possible exception of creating spatially uniform superchiral fields. In 2023, L. Cui and co-workers [114] investigated a design of a simple nanoslit which impressively generates chiral light with pure handedness inside the slit, which provides an ideal volume for molecular detection. Overall, the use of achiral

structures holds promising possibilities to facilitating chiroptical effects, and they provide ab excellent platform to study a range of interesting physical phenomena.

Bibliography

[1] P. Biagioni, J. S. Huang, L. Duò, M. Finazzi, and B. Hecht, “Cross resonant optical antenna,” *Phys. Rev. Lett.*, vol. 102, no. 25, pp. 1–4, 2009.

[2] H. Yuan *et al.*, “Generation and electric control of spin-valley-coupled circular photogalvanic current in WSe2,” *Nat. Nanotechnol.*, vol. 9, no. 10, pp. 851–857, 2014.

[3] T. Ellenbogen, K. Seo, and K. B. Crozier, “Chromatic plasmonic polarizers for active visible color filtering and polarimetry,” *Nano Lett.*, vol. 12, no. 2, pp. 1026–1031, 2012.

[4] S. Beychok, “Circular dichroism of biological macromolecules,” *Science (80-.).*, vol. 154, no. 3754, pp. 1288–1299, 1966.

[5] Y. Tang and A. E. Cohen, “Enhanced enantioselectivity in excitation of chiral molecules by superchiral light,” *Science (80-.).*, vol. 332, no. 6027, pp. 333–336, 2011.

[6] E. Hecht, *Optics*, 2nd ed. Reading: Addison-Wesley, 1987.

[7] A. Saha, K. Bhattacharya, and A. K. Chakraborty, “Achromatic quarter-wave plate using crystalline quartz,” *Appl. Opt.*, vol. 51, no. 12, pp. 1976–1980, 2012.

[8] M. S. El-Bahrawi, N. N. Nagib, S. A. Khodier, and H. M. Sidki,

"Birefringence of muscovite mica," *Opt. Laser Technol.*, vol. 30, no. 6, pp. 411–415, 1998.

[9] A. J. J. Kragt, I. P. M. van Gessel, A. P. H. J. Schenning, and D. J. Broer, "Temperature-Responsive Polymer Wave Plates as Tunable Polarization Converters," *Adv. Opt. Mater.*, vol. 7, no. 21, 2019.

[10] M. D. Lavrentovich, T. A. Sergan, and J. R. Kelly, "Switchable broadband achromatic half-wave plate with nematic liquid crystals," *Opt. Lett.*, vol. 29, no. 12, p. 1411, 2004.

[11] R. K. Komanduri, K. F. Lawler, and M. J. Escuti, "Multi-twist retarders: broadband retardation control using self-aligning reactive liquid crystal layers," *Opt. Express*, vol. 21, no. 1, p. 404, 2013.

[12] G. Zheng, H. Mühlenbernd, M. Kenney, G. Li, T. Zentgraf, and S. Zhang, "Metasurface holograms reaching 80% efficiency," *Nat. Nanotechnol.*, vol. 10, no. 4, pp. 308–312, 2015.

[13] N. Yu *et al.*, "Light Propagation with Phase Reflection and Refraction," *Science (80-.).*, vol. 334, no. October, pp. 333–337, 2011.

[14] X. Ni, N. K. Emani, A. V. Kildishev, A. Boltasseva, and V. M. Shalaev, "Broadband light bending with plasmonic nanoantennas," *Science (80-.).*, vol. 335, no. 6067, p. 427, 2012.

[15] Y. Zhao and A. Alù, "Manipulating light polarization with ultrathin plasmonic metasurfaces," *Phys. Rev. B - Condens. Matter Mater. Phys.*, vol. 84, no.

20, pp. 1–6, 2011.

[16] J. Hao *et al.*, “Manipulating electromagnetic wave polarizations by anisotropic metamaterials,” *Phys. Rev. Lett.*, vol. 99, no. 6, pp. 1–4, 2007.

[17] T. Li *et al.*, “Manipulating optical rotation in extraordinary transmission by hybrid plasmonic excitations,” *Appl. Phys. Lett.*, vol. 93, no. 2, 2008.

[18] N. Yu, F. Aieta, P. Genevet, M. A. Kats, Z. Gaburro, and F. Capasso, “A broadband, background-free quarter-wave plate based on plasmonic metasurfaces,” *Nano Lett.*, vol. 12, no. 12, pp. 6328–6333, 2012.

[19] Anthony Krier, *Mid-infrared Semiconductor Optoelectronics*. Springer London, 2007.

[20] Brian C. Smith, *Fundamentals of Fourier Transform Infrared Spectroscopy*. Boca Raton, 2011.

[21] A. Barth, “The infrared absorption of amino acid side chains,” *Prog. Biophys. Mol. Biol.*, vol. 74, no. 3–5, pp. 141–173, 2000.

[22] S. J. Parker, A.W., Quinn, *Infrared Spectroscopy of DNA*. Berlin, 2013.

[23] N. E. S. K. Peter C. Vollhardt, *Organic chemistry : structure and function*. New York: W.H. Freeman and Company, 2014.

[24] G. Roos and C. Roos, “Isomers and Stereochemistry,” in *Organic Chemistry Concepts*, Elsevier, 2015, pp. 43–54.

[25] J. H. Kim and A. R. Scialli, “Thalidomide: The tragedy of birth defects and

the effective treatment of disease," *Toxicol. Sci.*, vol. 122, no. 1, pp. 1–6, 2011.

[26] L. D. Barron, *Molecular Light Scattering and Optical Activity*. Cambridge University Press, 2004.

[27] H. E. Lee *et al.*, "Amino-acid- A nd peptide-directed synthesis of chiral plasmonic gold nanoparticles," *Nature*, vol. 556, no. 7701, pp. 360–364, 2018.

[28] M. L. Nesterov, X. Yin, M. Schäferling, H. Giessen, and T. Weiss, "The Role of Plasmon-Generated Near Fields for Enhanced Circular Dichroism Spectroscopy," *ACS Photonics*, vol. 3, no. 4, pp. 578–583, 2016.

[29] R. Knipper, V. Kopecký, U. Huebner, J. Popp, and T. G. Mayerhöfer, "Slit-Enhanced Chiral- and Broadband Infrared Ultra-Sensing," *ACS Photonics*, vol. 5, no. 8, pp. 3238–3245, 2018.

[30] Y. Zhao, A. N. Askarpour, L. Sun, J. Shi, X. Li, and A. Alù, "Chirality detection of enantiomers using twisted optical metamaterials," *Nat. Commun.*, vol. 8, pp. 6–13, 2017.

[31] T. Zhang, J. Liu, W. Shi, F. Fan, and S. Chang, "Enhancing terahertz circular dichroism spectrum of amino acid chiral enantiomers by all-dielectric metasurface," *Sensors Actuators A Phys.*, vol. 348, no. PA, p. 114001, 2022.

[32] S. Jeon and S. J. Kim, "Enhancement of optical chirality using

metasurfaces for enantiomer-selective molecular sensing," *Appl. Sci.*, vol. 11, no. 7, 2021.

[33] J. Hu, M. Lawrence, and J. A. Dionne, "High Quality Factor Dielectric Metasurfaces for Ultraviolet Circular Dichroism Spectroscopy," *ACS Photonics*, vol. 7, no. 1, pp. 36–42, 2020.

[34] Tim Wallace, "Stereochemistry," 2021. [Online]. Available: https://www.stereoelectronics.org/webSC/SC_04.html.

[35] M. Meyring *et al.*, "In vitro biotransformation of (R)- and (S)-thalidomide: Application of circular dichroism spectroscopy to the stereochemical characterization of the hydroxylated metabolites," *Anal. Chem.*, vol. 74, no. 15, pp. 3726–3735, 2002.

[36] H. Zou and G. R. Nash, "Efficient mid-infrared linear-to-circular polarization conversion using a nanorod-based metasurface," *Opt. Mater. Express*, vol. 12, no. 12, p. 4565, 2022.

[37] N. Shashar, R. Hagan, J. G. Boal, and R. T. Hanlon, "Cuttlefish use polarization sensitivity in predation on silvery fish," *Vision Res.*, vol. 40, no. 1, pp. 71–75, 2000.

[38] R. Wehner, "Polarized-light navigation by insects," *Sci. Am.*, vol. 235, no. 1, pp. 106–115, 1976.

[39] A. Sweeney, C. Jiggins, and S. Johnsen, "Polarized light as a butterfly mating signal," *Nature*, vol. 423, no. 6935, pp. 31–32, 2003.

[40] D. H. Goldstein, *Polarized Light*. Boca Raton: CRC Press, 2017.

[41] F. L. Kooi and A. Toet, “Visual comfort of binocular and 3D displays,” *Displays*, vol. 25, no. 2–3, pp. 99–108, 2004.

[42] A. Mosley, “Liquid crystal displays-an overview,” *Displays*, vol. 14, no. 2, pp. 67–73, 1993.

[43] H. Mott, “Definitions of Polarization in Radar,” in *Direct and Inverse Methods in Radar Polarimetry*, Dordrecht: Springer Netherlands, 1992.

[44] T. Kuppens, P. Bultinck, and W. Langenaeker, “Determination of absolute configuration via vibrational circular dichroism,” *Drug Discov. Today Technol.*, vol. 1, no. 3, pp. 269–275, 2004.

[45] G. G. Stokes, “On the Composition and Resolution of Streams of Polarized Light from different Sources,” in *Mathematical and Physical Papers*, Cambridge University Press, 2009, pp. 233–258.

[46] M. J. Walker, “Matrix Calculus and the Stokes Parameters of Polarized Radiation,” *Am. J. Phys.*, vol. 22, no. 4, pp. 170–174, 1954.

[47] E. Collett, *Field Guide to Polarization*. SPIE, 2005.

[48] E. Collett, “The Description of Polarization in Classical Physics,” *Am. J. Phys.*, vol. 36, no. 8, pp. 713–725, 1968.

[49] H. T. Chen, A. J. Taylor, and N. Yu, “A review of metasurfaces: Physics and applications,” *Reports Prog. Phys.*, vol. 79, no. 7, 2016.

[50] Y. Deng, Z. Cai, Y. Ding, S. I. Bozhevolnyi, and F. Ding, “Recent progress in metasurface-enabled optical waveplates,” *Nanophotonics*, vol. 11, no. 10, pp. 2219–2244, 2022.

[51] F. I. Baida, M. Boutria, R. Oussaid, and D. Van Labeke, “Enhanced-transmission metamaterials as anisotropic plates,” *Phys. Rev. B - Condens. Matter Mater. Phys.*, vol. 84, no. 3, pp. 1–8, 2011.

[52] J. Sung, E. M. Hicks, R. P. Van Duyne, and K. Spears, “Nanoparticle spectroscopy: Plasmon coupling in finite-sized two-dimensional arrays of cylindrical silver nanoparticles,” *J. Phys. Chem. C*, vol. 112, no. 11, pp. 4091–4096, 2008.

[53] P. Biagioni, M. Savoini, J. S. Huang, L. Duò, M. Finazzi, and B. Hecht, “Near-field polarization shaping by a near-resonant plasmonic cross antenna,” *Phys. Rev. B - Condens. Matter Mater. Phys.*, vol. 80, no. 15, pp. 2–5, 2009.

[54] M. A. Kats *et al.*, “Giant birefringence in optical antenna arrays with widely tailorable optical anisotropy,” *Proc. Natl. Acad. Sci. U. S. A.*, vol. 109, no. 31, pp. 12364–12368, 2012.

[55] M. Veysi, C. Guclu, O. Boyraz, and F. Capolino, “Thin anisotropic metasurfaces for simultaneous light focusing and polarization manipulation,” *J. Opt. Soc. Am. B*, vol. 32, no. 2, p. 318, 2015.

[56] A. C. Strikwerda, K. Fan, H. Tao, D. V. Pilon, X. Zhang, and R. D. Averitt, “Comparison of birefringent metamaterials and meanderline structure as

quarter-wave plates at terahertz frequencies," *Opt. InfoBase Conf. Pap.*, vol. 17, no. 1, pp. 4184–4187, 2009.

[57] C. Enkrich *et al.*, "Magnetic metamaterials at telecommunication and visible frequencies," *Phys. Rev. Lett.*, vol. 95, no. 20, pp. 5–8, 2005.

[58] D. Wang, Y. Gu, Y. Gong, C.-W. Qiu, and M. Hong, "An ultrathin terahertz quarter-wave plate using planar babinet-inverted metasurface," *Opt. Express*, vol. 23, no. 9, p. 11114, 2015.

[59] Y. Zhao and A. Aluì, "Tailoring the dispersion of plasmonic nanorods to realize broadband optical meta-waveplates," *Nano Lett.*, vol. 13, no. 3, pp. 1086–1091, 2013.

[60] W. Chen *et al.*, "Large-Area Nanoimprinted Colloidal Au Nanocrystal-Based Nanoantennas for Ultrathin Polarizing Plasmonic Metasurfaces," *Nano Lett.*, vol. 15, no. 8, pp. 5254–5260, 2015.

[61] F. Wang, A. Chakrabarty, F. Minkowski, K. Sun, and Q. H. Wei, "Polarization conversion with elliptical patch nanoantennas," *Appl. Phys. Lett.*, vol. 101, no. 2, 2012.

[62] A. Pors and S. I. Bozhevolnyi, "Efficient and broadband quarter-wave plates by gap-plasmon resonators," *Opt. Express*, vol. 21, no. 3, p. 2942, 2013.

[63] N. K. Grady *et al.*, "Terahertz metamaterials for linear polarization conversion and anomalous refraction," *Science (80-.).*, vol. 340, no. 6138,

pp. 1304–1307, 2013.

[64] Z. H. Jiang *et al.*, “Broadband and wide field-of-view plasmonic metasurface-enabled waveplates,” *Sci. Rep.*, vol. 4, pp. 1–8, 2014.

[65] H. F. Ma, G. Z. Wang, G. S. Kong, and T. J. Cui, “Broadband circular and linear polarization conversions realized by thin birefringent reflective metasurfaces,” *Opt. Mater. Express*, vol. 4, no. 8, p. 1717, 2014.

[66] F. Ding, Y. Yang, R. A. Deshpande, and S. I. Bozhevolnyi, “A review of gap-surface plasmon metasurfaces: Fundamentals and applications,” *Nanophotonics*, vol. 7, no. 6, pp. 1129–1156, 2018.

[67] C. C. Chang, Z. Zhao, D. Li, A. J. Taylor, S. Fan, and H. T. Chen, “Broadband Linear-to-Circular Polarization Conversion Enabled by Birefringent Off-Resonance Reflective Metasurfaces,” *Phys. Rev. Lett.*, vol. 123, no. 23, p. 237401, Dec. 2019.

[68] S. Fan and W. Suh, “Temporal coupled-mode theory for the Fano resonance in optical resonators,” vol. 20, no. 3, pp. 569–572, 2003.

[69] B. 2023, “Guide to Infrared Spectroscopy.” [Online]. Available: https://www.bruker.com/en/products-and-solutions/infrared-and-raman/ft-ir-routine-spectrometer/what-is-ft-ir-spectroscopy.html.

[70] L. M. Ng and R. Simmons, “Infrared Spectroscopy,” *Anal. Chem.*, vol. 71, no. 12, pp. 343–350, Jun. 1999.

[71] E. Hendry *et al.*, “Ultrasensitive detection and characterization of

biomolecules using superchiral fields," *Nat. Nanotechnol.*, vol. 5, no. 11, pp. 783–787, 2010.

[72] N. Meinzer, E. Hendry, and W. L. Barnes, "Probing the chiral nature of electromagnetic fields surrounding plasmonic nanostructures," *Phys. Rev. B - Condens. Matter Mater. Phys.*, vol. 88, no. 4, pp. 1–5, 2013.

[73] R. Tullius *et al.*, "'superchiral' Spectroscopy: Detection of Protein Higher Order Hierarchical Structure with Chiral Plasmonic Nanostructures," *J. Am. Chem. Soc.*, vol. 137, no. 26, pp. 8380–8383, 2015.

[74] T. B. Freedman, X. Cao, R. Dukor, and L. A. Nafie, "Absolute Configuration Determination of Chiral Molecules in the Solution State Using Vibrational Circular Dichroism," *Chirality*, vol. 15, no. 9, pp. 743–758, 2003.

[75] J. Mun *et al.*, "Electromagnetic chirality: from fundamentals to nontraditional chiroptical phenomena," *Light Sci. Appl.*, vol. 9, no. 1, 2020.

[76] Y. Tang and A. E. Cohen, "Optical chirality and its interaction with matter," *Phys. Rev. Lett.*, vol. 104, no. 16, pp. 1–4, 2010.

[77] D. M. Lipkin, "Existence of a new conservation law in electromagnetic theory," *J. Math. Phys.*, vol. 5, no. 5, pp. 696–700, 1964.

[78] M. Schäferling, D. Dregely, M. Hentschel, and H. Giessen, "Tailoring enhanced optical chirality: Design principles for chiral plasmonic nanostructures," *Phys. Rev. X*, vol. 2, no. 3, pp. 1–9, 2012.

[79] M. Schäferling, N. Engheta, H. Giessen, and T. Weiss, "Reducing the

Complexity: Enantioselective Chiral Near-Fields by Diagonal Slit and Mirror Configuration," *ACS Photonics*, vol. 3, no. 6, pp. 1076–1084, 2016.

[80] E. Hendry, R. V. Mikhaylovskiy, L. D. Barron, M. Kadodwala, and T. J. Davis, "Chiral electromagnetic fields generated by arrays of nanoslits," *Nano Lett.*, vol. 12, no. 7, pp. 3640–3644, 2012.

[81] T. Iida *et al.*, "Super-chiral vibrational spectroscopy with metasurfaces for high-sensitive identification of alanine enantiomers," *Appl. Phys. Lett.*, vol. 117, no. 10, 2020.

[82] K. S. Yee, "Numerical solution of initial boundary value problems involving maxwell's equations in isotropic media," *IEEE Trans. Antennas Propag.*, vol. 14, no. 3, pp. 302–307, 1966.

[83] M. E. B. Allen Taflove, "Numerical Solution of Steady-State Electromagnetic Scattering Problems Using the Time-Dependent Maxwell's Equations," *IEEE Trans. Microw. Theory Tech.*, vol. 23, no. 8, pp. 623–630, 1975.

[84] M. E. B. Allen Taflove, "Computation of the Electromagnetic Fields and Induced Temperatures Within a Model of the Microwave-Irradiated Human Eye," *IEEE Trans. Microw. Theory Tech.*, vol. 23, no. 11, pp. 888–896, 1975.

[85] S. D. Gedney, *Introduction to the Finite-DifferenceTime-Domain (FDTD) Method for Electromagnetics*. Cham: Springer International Publishing, 2011.

[86] A. Christ and H. L. Hartnagel, “Three-Dimensional Finite-Difference Method for the Analysis of Microwave-Device Embedding,” *IEEE Trans. Microw. Theory Tech.*, vol. 35, no. 8, pp. 688–696, Aug. 1987.

[87] E. D. Palik, “Handbook of Optical Constants of Solids, Five-Volume Set,” p. 3224, 1997.

[88] H. R. Barnard and G. R. Nash, “Tailoring the spectral properties of layered chiral mid-infrared metamaterials,” *Appl. Phys. Lett.*, vol. 119, no. 24, 2021.

[89] C. Shi, I. J. Luxmoore, and G. R. Nash, “Gate tunable graphene-integrated metasurface modulator for mid-infrared beam steering,” *Opt. Express*, vol. 27, no. 10, p. 14577, 2019.

[90] Ansys Canada Ltd, “FDTD solver - Simulation Object.” [Online]. Available: https://optics.ansys.com/hc/en-us/articles/360034382534-Simulation-FDTD.

[91] A. C. Ltd., “Understanding frequency domain CW normalization.” [Online]. Available: https://optics.ansys.com/hc/en-us/articles/360034394234-Understanding-frequency-domain-CW-normalization.

[92] A. C. Ltd., “Convergence testing process for FDTD simulations.” [Online]. Available: https://optics.ansys.com/hc/en-us/articles/360034915833-Convergence-testing-process-for-FDTD-simulations.

[93] “Periodic Table of Elements (EnvironmentalChemistry.com).” [Online]. Available: https://environmentalchemistry.com/yogi/periodic/. [Accessed:

03-Oct-2022].

[94] T. H. P. Chang, “Proximity effect in electron beam lithography,” *J. Vac. Sci. Technol.*, vol. 12, no. 6, pp. 1271–1275, 1975.

[95] Brucker Optics, “Bruker Vertex Series Brochure,” 2021. [Online]. Available: https://www.bruker.com/en/products-and-solutions/infrared-and-raman/ft-ir-research-spectrometers/vertex-research-ft-ir-spectrometer/vertex-80-80v-ft-ir-spectrometer.html.

[96] U. S. S. of C. on behalf of the U.S.A., “NIST Chemistry WebBook, SRD 69, Carbon dioxide infrared spectroscopy.” [Online]. Available: https://webbook.nist.gov/cgi/cbook.cgi?ID=C124389&Type=IR-SPEC&Index=1.

[97] U. S. S. of C. on behalf of the U.S.A., “NIST Chemistry WebBook, SRD 69, Water gas infrared spectroscopy.” [Online]. Available: https://webbook.nist.gov/cgi/cbook.cgi?ID=C7732185&Units=SI&Type=IR-SPEC&Index=0#IR-SPEC.

[98] Thorlabs, “Unprotected gold parabolic mirror.” [Online]. Available: https://www.thorlabs.com/newgrouppage9.cfm?objectgroup_id=12395.

[99] L. S. Inc, “Diffraction grating,” 2015. [Online]. Available: https://optics.ansys.com/hc/en-us/articles/360042088813-Diffraction-grating.

[100] A. Pors and S. I. Bozhevolnyi, “Plasmonic metasurfaces for efficient phase

control in reflection," *Opt. Express*, vol. 21, no. 22, p. 27438, 2013.

[101] A. C. Ltd., "https://optics.ansys.com/hc/en-us/articles/360034395074-Calculating-charge-distributions-and-currents-in-metals-induced-by-an-optical-field." .

[102] H.-T. Chen, "Interference theory of metamaterial perfect absorbers," *Opt. Express*, vol. 20, no. 7, p. 7165, 2012.

[103] B. Schaefer, E. Collett, R. Smyth, D. Barrett, and B. Fraher, "Measuring the Stokes polarization parameters," *Am. J. Phys.*, vol. 75, no. 2, pp. 163–168, 2007.

[104] M. Schäferling, X. Yin, and H. Giessen, "Formation of chiral fields in a symmetric environment," *Opt. Express*, vol. 20, no. 24, p. 26326, 2012.

[105] J. P. erdousi Akhtar, "A Study on Growth, Structural, Optical and Electrical Characterization of L-alanine Single Crystal for Optoelectronic Devices," *Res. J. Phys.*, vol. 6, pp. 31–40, 2012.

[106] S. A. Avila, S. S. M. Francis, and A. L. Rajesh, "Synthesis , growth and characterization of L -Alanine Potassium Chloride single crystal : a phase-matchable semi-organic material for second and third order NLO applications," *J. Mater. Sci. Mater. Electron.*, vol. 28, no. 1, pp. 1051–1059, 2017.

[107] J. Garciá-Guirado, M. Svedendahl, J. Puigdollers, and R. Quidant, "Enantiomer-Selective Molecular Sensing Using Racemic Nanoplasmonic

Arrays," *Nano Lett.*, vol. 18, no. 10, pp. 6279–6285, 2018.

[108] L. V. Poulikakos, P. Thureja, A. Stollmann, E. De Leo, and D. J. Norris, "Chiral Light Design and Detection Inspired by Optical Antenna Theory," *Nano Lett.*, vol. 18, no. 8, pp. 4633–4640, 2018.

[109] S. Droulias and L. Bougas, "Chiral sensing with achiral anisotropic metasurfaces," *Phys. Rev. B*, vol. 104, no. 7, pp. 1–11, 2021.

[110] A. Horrer *et al.*, "Local Optical Chirality Induced by Near-Field Mode Interference in Achiral Plasmonic Metamolecules," *Nano Lett.*, vol. 20, no. 1, pp. 509–516, 2020.

[111] T. J. Davis and E. Hendry, "Superchiral electromagnetic fields created by surface plasmons in nonchiral metallic nanostructures," *Phys. Rev. B - Condens. Matter Mater. Phys.*, vol. 87, no. 8, pp. 1–5, 2013.

[112] T. Cao and M. J. Cryan, "Circular dichroism in planar nonchiral metamaterial made of elliptical nanoholes array," *J. Electromagn. Waves Appl.*, vol. 26, no. 10, pp. 1275–1282, 2012.

[113] S. Hashiyada, T. Narushima, and H. Okamoto, "Active Control of Chiral Optical near Fields on a Single Metal Nanorod," *ACS Photonics*, vol. 6, no. 3, pp. 677–683, 2019.

[114] L. Cui, X. Yang, B. Reynier, C. Schwob, and S. Bidault, "An achiral magnetic photonic antenna as a tunable nanosource of superchiral light," *arXiv Prepr. arXiv2301.11044*, 2023.